LEVEL II

THERMOELECTRICALLY COOLED FOCAL PLANE FOR NON-SCANNING SYSTEMS

Honeywell

SYSTEMS & RESEARCH CENTER

2600 RIDGWAY PARKWAY
MINNEAPOLIS, MINNESOTA 55413

February 1979

Final Technical Report for Period July 6, 1977 – May 6, 1978

Prepared for

Army Night Vision and Electro-Optics Laboratory (NV&EOL)
U.S. Army Electronics Command
Fort Belvoir, Virginia 22060

NOTICE

When Government drawings, specifications, or other data are used for any purpose other than in connection with a definitely related Government procurement operation, the United States Government thereby incurs no responsibility nor any obligation whatsoever; and the fact that the government may have formulated, furnished, or in any way supplied the said drawings, specifications, or other data is not to be regarded by implication or otherwise as in any manner licensing the holder or any other person or corporation, or conveying any rights or permission to manufacture, use, or sell any patented invention that may in any way be related thereto.

This final technical report for the period 6 June 1977 through 6 May 1978 was prepared by Honeywell Inc., Systems and Research Center, 2600 Ridgway Parkway, Minneapolis, Minnesota 55413, under Contract No. DAAK70-77-C-0160 for the Army Night Vision and Electro-Optics Laboratory, Fort Belvoir, Virginia 22060.

The technical monitor for this contract at NVL was Ray Balcerak. At Honeywell, this work was carried out at the Systems and Research Center, Minneapolis, Minnesota, and at the Honeywell Electro-Optics Center, Lexington, Massachusetts. N.A. Foss was the Honeywell Program Manager and Principal Investigator. Contributors included M. Gurnee, D. Marshall, D. Wick, D. Gregorich, T. Hendrickson, and J. Schwanabeck. Distribution of this report is limited to U.S. Government agencies only. Other requests for this document must be referred to Director, Night Vision Laboratory, Attn: DELNV-FIRD, Fort Belvoir, Virginia 22060.

This technical report has been reviewed and is approved for publication. The views, opinions and/or findings contained in this report are those of the authors and should not be construed as an official Department of the Army position, policy, or decision, unless so designated by other documentation.

Copies of this report should not be returned unless return is required by security considerations, contractual obligations, or notice on a specific document.

Final rept. 6 Jun 77-6 May 78,

UNCLASSIFIED
SECURITY CLASSIFICATION OF THIS PAGE (WHEN DATA ENTERED)

REPORT DOCUMENTATION PAGE		READ INSTRUCTIONS BEFORE COMPLETING FORM
1. REPORT NUMBER	2. GOVT ACCESSION NUMBER	3. RECIPIENT'S CATALOG NUMBER
4. TITLE (AND SUBTITLE) (6) Thermoelectrically Cooled Focal Plane for Non-Scanning Systems		5. TYPE OF REPORT/PERIOD COVERED Final Technical 6/6/77 - 5/6/78
		6. PERFORMING ORG. REPORT NUMBER (14) 78SRC71
7. AUTHOR(S) (10) N. A. Foss, M. N. Gurnee, T. Hendrickson		8. CONTRACT OR GRANT NUMBER(S) (15) DAAK70-77-C-0160
9. PERFORMING ORGANIZATIONS NAME/ADDRESS Honeywell Incorporated Systems and Research Center 2600 Ridgway Parkway, Minneapolis, MN 55413		10. PROGRAM ELEMENT, PROJECT, TASK AREA & WORK UNIT NUMBERS (12) 227p.
11. CONTROLLING OFFICE NAME/ADDRESS Night Vision and Electro-Optics Laboratory U.S. Army Electronics Command Fort Belvoir, Virginia 22060		(11) 12. REPORT DATE Febr[illegible]979 13. NUMBER OF PAGES 236
14. MONITORING AGENCY NAME/ADDRESS (IF DIFFERENT FROM CONT. OFF.)		15. SECURITY CLASSIFICATION (OF THIS REPORT) Unclassified
		15a. DECLASSIFICATION DOWNGRADING SCHEDULE

16. DISTRIBUTION STATEMENT (OF THIS REPORT)
Distribution limited to U.S. Government agencies only. Other requests for this document must be referred to Director, Army Night Vision and Electro-Optics Laboratory DELNV-FIRD, Fort Belvoir, Virginia 22060

17. DISTRIBUTION STATEMENT (OF THE ABSTRACT ENTERED IN BLOCK 20, IF DIFFERENT FROM REPORT)

18. SUPPLEMENTARY NOTES

19. KEY WORDS (CONTINUE ON REVERSE SIDE IF NECESSARY AND IDENTIFY BY BLOCK NUMBER)
micrometers

20. ABSTRACT (CONTINUE ON REVERSE SIDE IF NECESSARY AND IDENTIFY BY BLOCK NUMBER)
The objectives of this contract were to (a) analyze potential system applications for 3 to 5 (μm) TE-cooled staring focal planes and to determine both universal and unique focal plane requirements for each of the applications; (b) determine critical detector and focal plane signal processing parameters and develop preliminary designs for these focal planes; (c) evaluate the overall focal plane designs to determine system performance; and (d) make performance measurements on sample detector elements, focal plane electronics, and equalization processing electronics to substantiate predictions of →

DD FORM 1 JAN 73 1473 EDITION OF 1 NOV 55 IS OBSOLETE

HD-168 REV 11/74

79 06 12 050

402 349 Gun

23 30 057

20. Abstract (concluded)

device performance.

A tradeoff of staring and scanned array systems showed that tremendous systems performance improvements can be made by using high density staring focal plane arrays. In particular, improved MRT and NEΔT performance, reduced power consumption, lightweight and all electronic operation (no moving parts) are advantages which staring arrays have over scanned arrays.

The application areas investigated were broken down into three categories: small anti-armor weapons, surveillance systems, and remote piloted vehicles (RPV). The focal plane requirements for these systems were established and number of detectors, IFOV, frame rate, and dynamic range requirements were also established.

Focal plane design considerations showed that staring arrays can achieve optimum performance by means of backside illuminated detector arrays which are flip-chip bump mounted to CCD readout electronics. Detector performance modeling was done to trade off the detector crosstalk and quantum efficiency as a function of detector thickness. Results showed that quantum efficiency greater than 50 percent with crosstalk to adjacent detectors of about 7 percent can be achieved with 12 μm thick HgCdTe backside illuminated detectors.

Analysis of the readout electronics requirements showed that it is possible to do the difficult dc suppression function at each detector input by means of Honeywell's multiple sample injection (MSI) input technique. Other detector/CCD coupling techniques analyzed either resulted in complex, high packing density structures or large reset noise levels when going to the very small pixel sizes.

Responsivity and offset nonuniformity correction requirements were established which showed that offset correction levels on the order of 10 to 11 bits are required while responsivity compensation can be kept to 8 correction bits. Techniques were investigated for implementation of the compensation function in a lowest power configuration. Digital and analog implementations were considered and the conclusion was that analog compensation techniques such as Honeywell's Double Buffer Memory Module (proprietary design) represent a real power and size savings for the compensation electronics.

Staring array performance modeling was done through a modification to the NVL "Static Performance Model for Thermal Viewing Systems." The output from these calculations was characterizations of the MRT and NEΔT parameters for the staring arrays.

A supplementary section has been published in a separate, proprietary volume. It contains details of the DBM uniformity compensation approach and the application of electro-optical shutters for non-uniformity compensation.

FOREWORD

This final technical report was prepared by Honeywell Inc., Systems and Research Center, 2600 Ridgway Parkway, Minneapolis, Minnesota 55413, under Contract No. DAAK70-77-C-0160 for the Army Night Vision and Electro-Optics Laboratory, Fort Belvoir, Virgina 22060. The technical monitor for this contract at NVL was Ray Balcerak.

At Honeywell, this work was carried out at the Systems and Research Center, Minneapolis, Minnesota, and the Honeywell Electro-Optics Center, Lexington, Massachusetts. N.A. Foss was the Honeywell Program Manager and Principal Investigator. Contributors included M. Gurnee, D. Marshall, D. Wick, D. Gregorich, T. Hendrickson, and J. Schwanabeck.

This final report covers the period from 6/6/77 to 5/6/78.

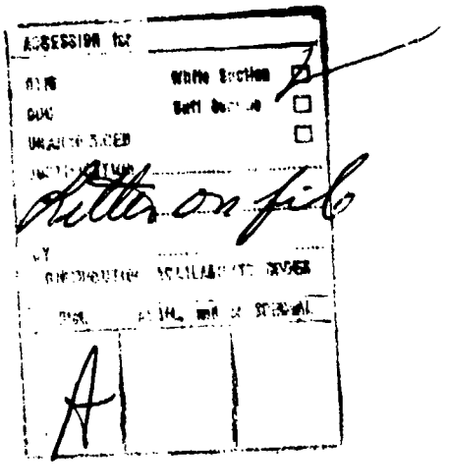

CONTENTS

CONTENTS (continued)

CONTENTS (concluded)

LIST OF ILLUSTRATIONS

LIST OF ILLUSTRATIONS (continued)

LIST OF ILLUSTRATIONS (continued)

LIST OF ILLUSTRATIONS (continued)

LIST OF ILLUSTRATIONS (continued)

LIST OF ILLUSTRATIONS (concluded)

LIST OF TABLES

LIST OF TABLES (concluded)

SECTION I

INTRODUCTION AND SUMMARY

This Final Technical Report presents the work performed on contract no. DAAK70-77-C-0160, Thermoelectrically Cooled Focal Plane for Non-Scanning Systems.

The objectives of this contract were to:

- Analyze potential system applications for 3 to 5 μm TE-cooled staring focal planes and to determine both universal and unique focal plane requirements for each of the applications
- Determine critical detector and focal plane signal processing parameters and develop preliminary designs for these focal planes
- Evaluate the overall focal plane designs to determine system performance
- Make performance measurements on sample detector elements, focal plane electronics, and equalization processing electronics to substantiate predictions of device performance

The analysis and results of the experimental work are presented in this report. A summary of the results of these studies is as follows:

STARING AND SCANNED ARRAY TRADEOFFS

Tremendous systems performance improvements can be made by use of high density staring focal plane arrays. In particular, improved MRT and NEΔT performance, reduced power consumption, lightweight and all electronic (no moving parts) are advantages which staring arrays have over scanned arrays.

APPLICATIONS AND REQUIREMENTS

The application areas investigated were broken down into three categories:

- Small anti-armor weapons
- Surveillance systems
- Remote piloted vehicles (RPV)

The focal plane requirements for these systems were established and number of detectors, IFOV, frame rate, and dynamic range requirements were also established.

FOCAL PLANE DESIGN

Focal plane design considerations showed that staring arrays can acheive optimum performance by means of backside illuminated detector arrays which are flip-chip bump mounted to the CCD readout electronics.

Detector performance modeling was done to trade off the detector crosstalk and quantum efficiency as a function of detector thickness. Results showed

that quantum efficiency greater than 60 percent with crosstalk to adjacent detectors of about 7 percent can be achieved with 12 μm thick HgCdTe back-side illuminated detectors.

Analysis of the readout electronics requirements showed that it is possible to do the difficult dc suppression function at each detector input by means of Honeywell's multiple sample injection (MSI) input technique. Other detector/CCD coupling techniques analyzed either resulted in complex, high packing density structures or large reset noise levels when going to the very small pixel sizes.

NONUNIFORMITY COMPENSATION

Responsivity and offset nonuniformity correction requirements were established which showed that offset correction levels on the order of 10 to 11 bits are required while responsivity compensation can be kept to eight correction bits. Techniques were investigated for implementation of the compensation function in a lowest power configuration. Digital and analog implementations were considered with the conclusion being that analog compensation techniques such as Honeywell's Double Buffer Memory Module (Proprietary Design discussed in Supplement A) represents a real power and size savings for the compensation electronics.

STARING SYSTEM MODELING

A computer program was developed to model the staring array performance characteristics. A modification to the NVL static performance model for thermal viewing systems was derived and performance modeling of the MRT and NEΔT parameters were calculated.

The final report is organized according to the outline above. In addition, there are five appendixes which present detailed analysis of the MSI input circuit operation and details of the system performance modeling calculations.

A supplementary section has been published in a separate, proprietary volume. It contains details of the DBM uniformity compensation approach and the application of electro-optical shutters for nonuniformity compensation.

SECTION II

STARING AND SCANNED ARRAY TRADEOFFS

The development of non-scanning (i.e., staring) focal planes brings thermal imaging systems out of the realm of an electromechanical configuration and into the area of an all electronic structure. Serial, serial/parallel, and parallel scan imaging systems all require the use of at least one rotating scan mirror in order to scan the scene radiation over the detector array as shown in Figure 2-1. Problems with the use of these scan mirrors results in lifetime limitations, increased power and weight requirements, and in some cases the use of sophisticated scan converters to convert the output signal to a TV-compatible format. The use of a staring focal plane eliminates the mechanical scanning components. Also, performance characteristics are improved due to the increased number of detector elements and the longer integration times possible with a staring configuration.

When these staring focal planes are operated at thermoelectrically cooled temperatures, additional advantages in reduced system size and power dissipation are also gained.

The inherent advantages of a non-scanned TE-cooled focal plane are summarized below:

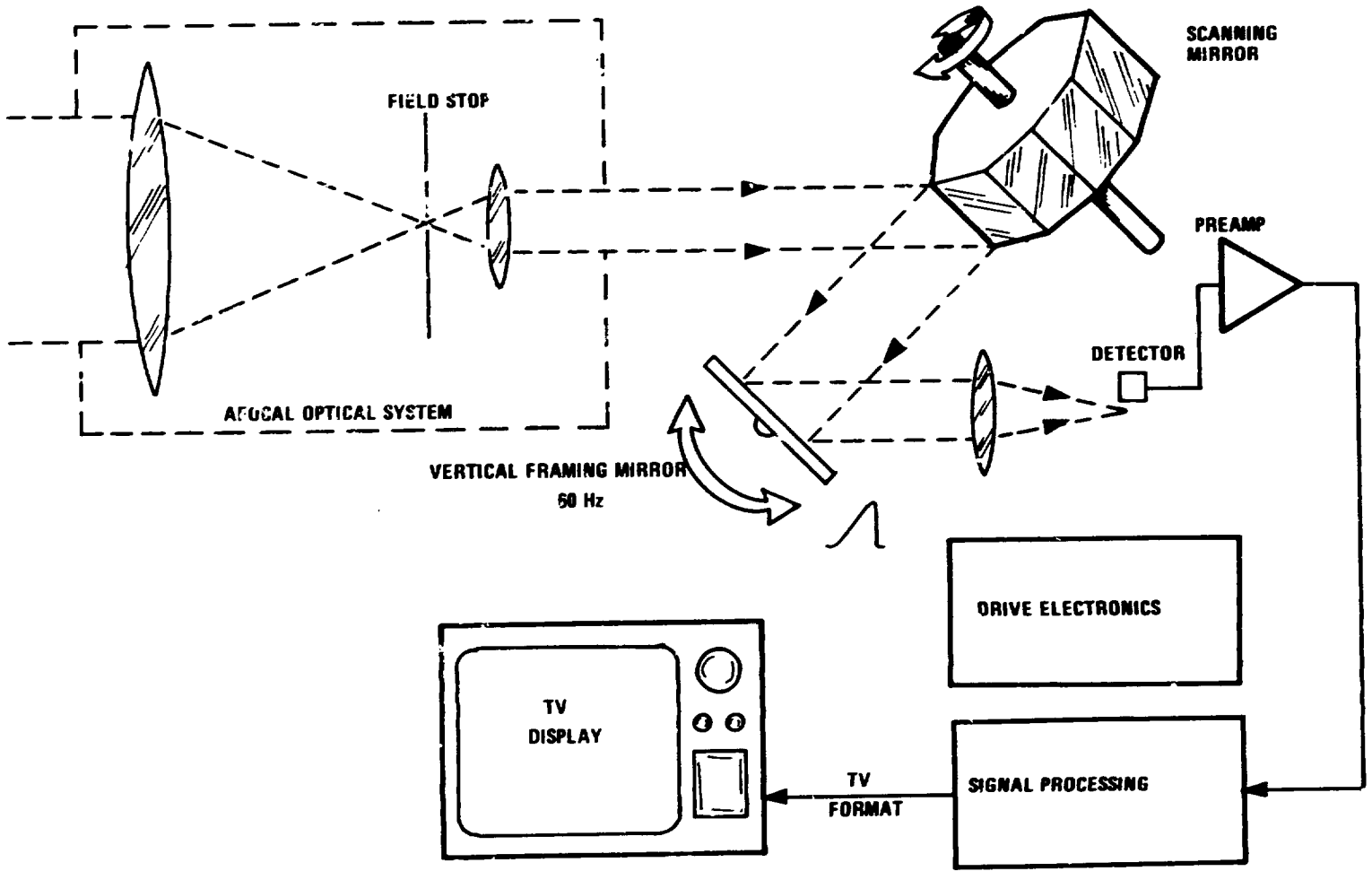

Figure 2-1. Basic Principles of Serial/Parallel Scanning Systems

- High performance--The minimum resolvable temperature (MRT) and noise equivalent temperature difference (NEΔT) are inversely proportional to the integration time.
- Low power consumption--No scan motor power is required, and only a low power TE cooler or zero power-consumption Freon cooler is necessary.
- Lightweight--Portable, rugged missile seekers and hand-held thermal imagers are possible.
- No moving parts--This means added reliability and reduced cost.

Staring focal planes, therefore, emphasize purely electronic ways of achieving high performance. This emphasis makes it easy and attractive to incorporate them into near-term missile seeker systems and lightweight thermal viewers.

Focal planes operating at TE-cooled temperatures offer an additional advantage over systems requiring liquid N_2 cooling in that the system can be operated with either a thermoelectric cooler or a low pressure Freon bottle if desired. These low pressure bottles are particularly attractive in missile applications where they have the advantages of long storage life, safety, and low cost over conventional high pressure, low temperature bottles. Low pressure (400 to 700 psi) Freon bottles (i.e., Freon 23, 13, or 16) have boiling points in the range of 191 to 195 K which makes them ideal candidates for such a cooling system. When thermoelectric

coolers are used in missile seeker applications, the seeker can operate indefinitely in an "armed" status and the missile does not have to be committed to firing (or disposal) as is the case with gas bottle systems.

While elimination of the scan mirror reduces the mechanical complexity of the imaging system, it brings with it the problem of having to perform a more complex nonuniformity compensation function. Serial/parallel scan imaging systems having from 10 to 20 detector channels can be normalized for readout electronics offset and detector responsivity variations by manually adjusting the channel offset and gain adjust controls. As the number of output channels increases (e.g., with parallel scan or staring focal planes), the adjustment of the hundreds or thousands of detector channels must be implemented via automatic electronic compensation techniques. The compensation technique used must be a lightweight, low power approach consistent with these relative advantages of the staring system.

Table 2-1 summarizes the relative advantages and disadvantages of five different focal plane configurations which include:

1. TE-cooled staring arrays
2. Serial scan (i.e., Mini-FLIR)
3. Parallel scan/parallel output (i.e., Common Modular FLIR)
4. Serial/parallel scan (i.e., MATRIX FLIR)
5. Parallel scan/serial output (i.e., Honeywell TWS approach)

TABLE 2-1. RELATIVE ADVANTAGES AND DISADVANTAGES OF DIFFERENT IR THERMAL IMAGING SYSTEMS

	TE-Cooled Staring Arrays	Serial Scan	Parallel Scan/ Parallel Output	Serial/Parallel Scan	Parallel Scan/ Serial Output
Example System	• Missile Seeker • Hand-Held Thermal Viewer	• Mini-FLIR --Two-Axis scan system	• Common Modular FLIR --Linear array = 180 detectors --Parallel output = 180 amplifiers --Parallel scan mirror	• MATRIX FLIR --Two-axis mirror	• Honeywell TWS --Parallel scan mirror
Advantages	• Low Power • Portable, rugged • All electronic--moving parts • Compatible with many display formats	• Few detectors • Electronically simple • No uniformity compensation • Direct LED view • TV-compatible output	• Parallel processing, low data rates • Direct LED viewing	• Parallel processing moderate data rates • TDI--defect tolerance	• TDI--defect tolerance • TV-compatible • Moderate power, size
Disadvantages	• More complex nonuniformity compensation	• Mechanically complex --High speed rotating parts --Life, angular rate limits • Power	• Mechanical scan • Scan converter display • Parallel configuration --Redundant electronics --Preamplifiers • Weight, power, size	• Mechanically complex • Power, weight • Scan converter	• Mechanical scanner

An example of a staring focal plane design suitable for either missile seeker applications or thermal imaging systems is shown in Figure 2-2. In this figure the detector/CCD focal plane is mounted onto a TE cooler which is housed within a hard-vacuum dewar.

The optical system shown is designed to accommodate an electro-optical shutter which periodically images a "blackbody" reference onto the focal plane to update the nonuniformity equalization coefficients and to correct for dc drift. As can be seen in this figure, the overall optics/focal plane design is extremely simple compared with more conventional scanned systems.

This can also be seen in Figure 2-3 which shows the overall thermal imager system block diagram. As shown in this figure, the electronics package consists of the focal plane waveform generators, temperature controller, video processing, and nonuniformity compensation functions. The non-uniformity compensation function can be achieved through one of many different approaches, as will be described later.

The performance advantages realized with a dense staring focal plane are due principally to the much larger number of detectors that may be used. An example is shown in Figure 2-4 which presents the MRT vs. temperature calculations for a scanned array of 350 x 4 (TDI) detectors and a non-scanned array which consists of 350 x 260 detectors. (The system modeling was done using the Honeywell Staring Focal Plane Performance Model, described in Section VI, which is a modification to the NVL Thermal Imager Performance Model.) The MRT values for the

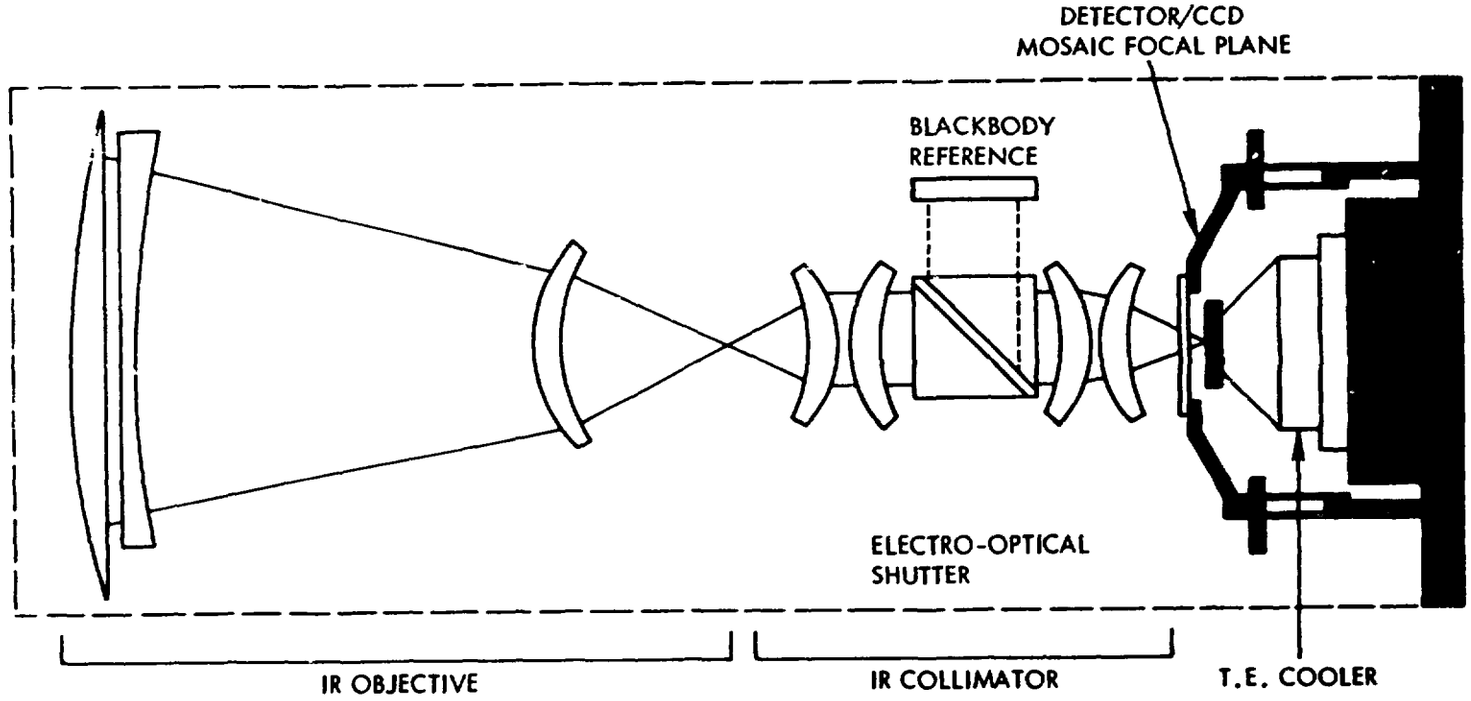

Figure 2-2. Staring Focal Plane Optical Design

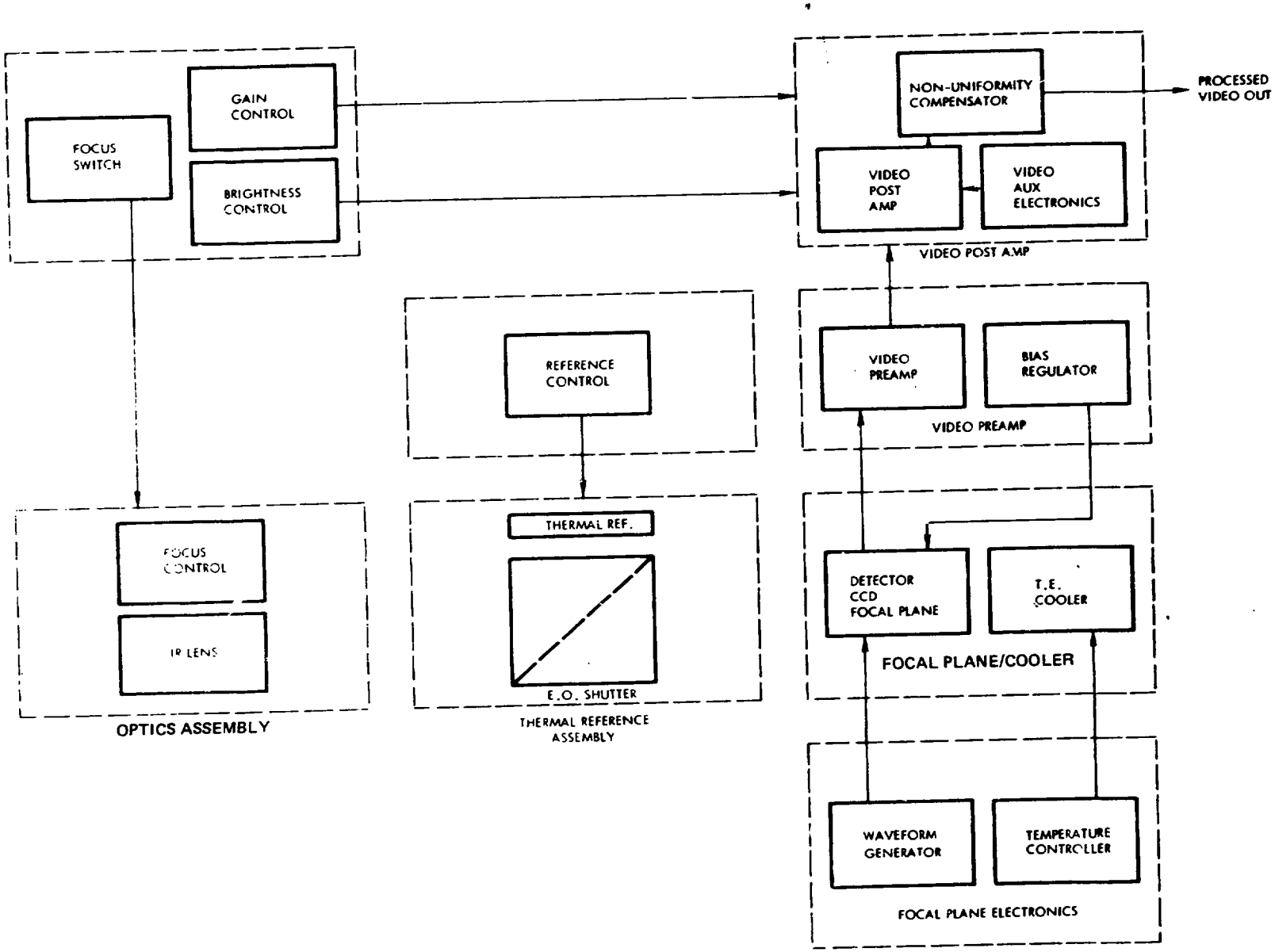

Figure 2-3. Thermal Imager Assembly Using Staring Focal Plane

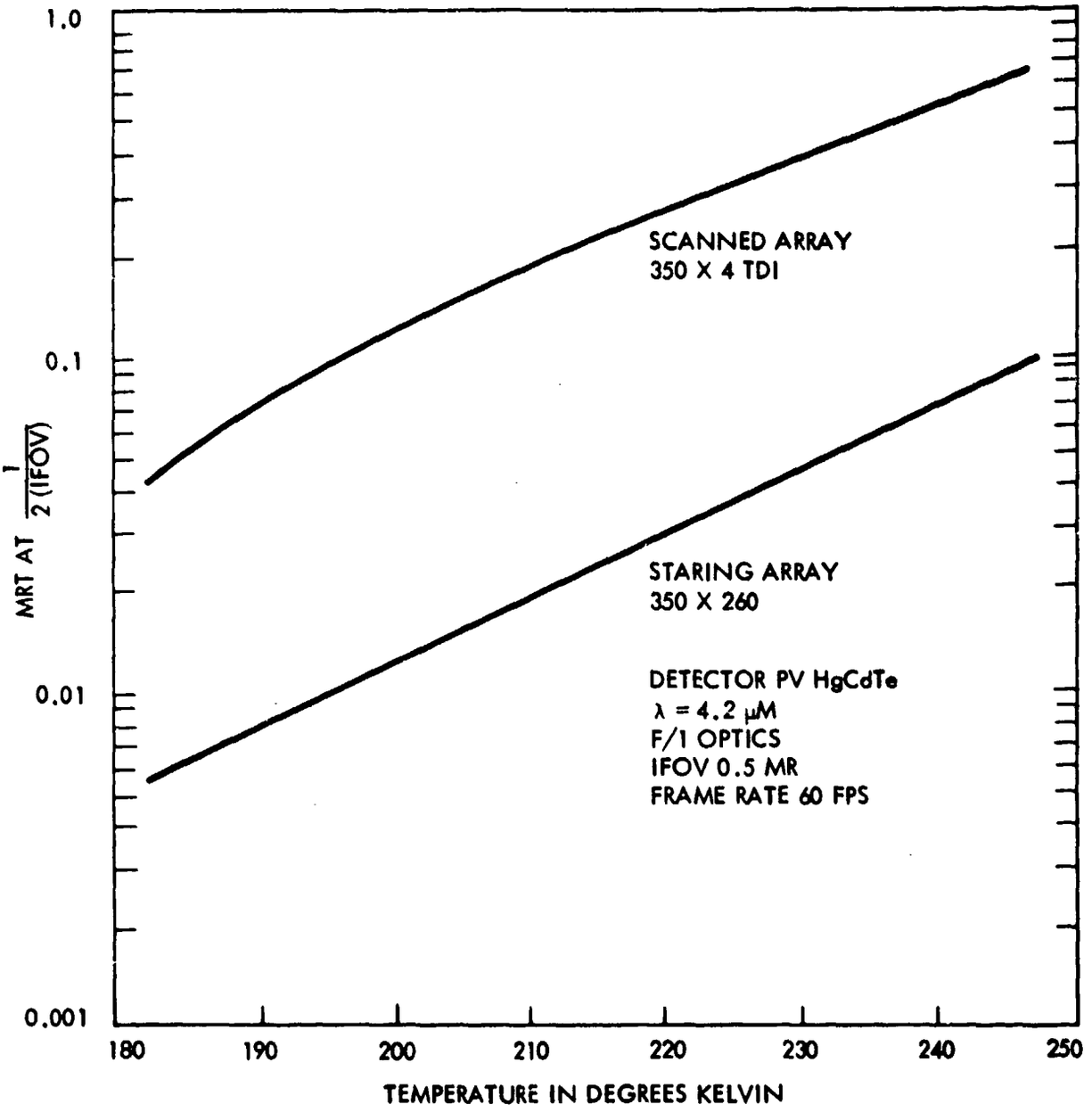

Figure 2-4. MRT vs. Temperature for Staring and Scanner Detector Arrays

particular system modeled is on the order of MRT = 0.01 K for the staring array at 195 K, an excellent MRT level. Of particular advantage here is that the staring array can operate at ≃ 240 K with the same performance level as the scanned system at T = 190 K. This results in a significant reduction in the TE cooler power requirement.

SUMMARY OF ADVANTAGES

The staring focal plane system has great advantages in the area of reduced weight, size, and power over scanned imaging systems. Table 2-2 shows the power and weight comparison of the staring system compared with three different scanned imagers. The staring array under consideration is a 525 x 390 element array which operates at T = 240 K; this results in MRT performance comparable to the three other imaging systems operating at 77 K. The weight and power reduction available through the staring system is considerable as can be seen in this table.

A total system power dissipation of only 7.5 watts and a weight of less than 4 pounds makes this system extremely attractive for hand-held night-sights and missile seeker applications. The main power dissipation is related to the nonuniformity compensation electronics and is such that the system power dissipation would decrease to about 6.2 watts for a smaller 256 x 192 element focal plane (assuming that analog compensation techniques are used to correct for the offset and responsivity nonuniformities). The Honeywell Thermal Weapons Sight (TWS) approach is shown to be the next best system in terms of weight and power dissipation. Even compared to the outstanding characteristics of the parallel scanned TWS approach, the staring focal plane results in an additional 25 percent weight and power advantage.

TABLE 2-2. POWER/WEIGHT COMPARISON FOR THE STARING ARRAY AS COMPARED WITH SEVERAL DIFFERENT SCANNED IMAGING SYSTEMS

	525 x 390 Staring Array	Parallel Scan Imager (Honeywell TWS)	Mini-Flir (RPV FLIR)	Common Modular FLIR
Power				
Scanner	0	2.0	18	
Cooler	1.5*	3.5**	BOTTLE	
F.P. Electronics	1.4	1.4	≈ 0	
Electronics	3.1	1.4	13	
Display	1.5	1.5		
Total Power	7.5 W	9.8 W	31 W	96 W
Weight	3.9 lbs	5.2 lbs	14 lbs	46 lbs

Nonuniformity compensation using analog techniques

* T (Focal Plane) = 240 K

** T (Focal Plane) = 195 K

SECTION III

APPLICATIONS AND REQUIREMENTS

Staring focal plane system applications can be categorized into three general areas:

- Small Anti-Armor Weapons
  - SADARM (Sense and Destroy Armor)
  - FFAST (Fire and Forget Anti-tank System Technology)
  - TGSM (Terminally Guided Submunition)
  - Fire and Forget
- Surveillance Systems
  - Night Sight Imagers
  - Individual Serve Weapon Sights
  - Threat Warning
- Remotely Piloted Vehicles
  - Over-The-Horizon (OTH)
  - POISE RPV (Pointing and Stabilization Element)

To generate the focal plane requirements for these types of systems, we can categorize the applications into general requirement areas.

Infrared systems with potential applications for TE-cooled staring focal planes, including hand-held viewers, missile seekers, artillery guidance, RPV sensors, and others, are best identified by considering the tactical scenario in which the system is intended to operate. Figure 3-1 shows a

CATEGORY #1: OVERHEAD TO 45° FROM VERTICAL

CATEGORY #2: 30° TO 60° FROM VERTICAL

CATEGORY #3: GREATER THAN 60° FROM VERTICAL

CATEGORY #4: GROUND BASED IMAGING

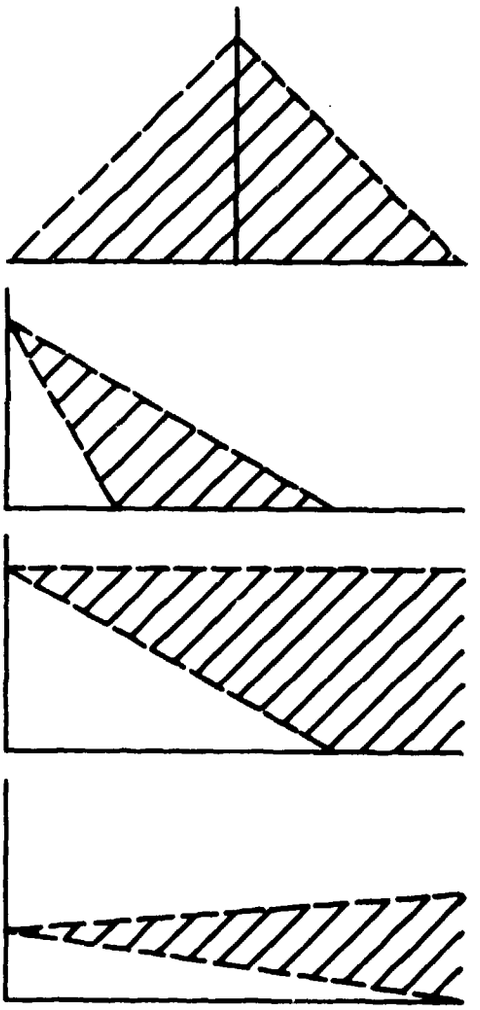

Figure 3-1. Tactical Scenarios According to Imager-To-Target Viewing Angle

method of categorizing the operational scenario according to the angle of incidence between the imager and the target. We can identify the following four categories:

1. Overhead to 45 degrees from vertical
2. 30 degrees to 60 degrees from vertical
3. Greater than 60 degrees from vertical
4. Ground based imaging (near-horizontal viewing)

The first two categories would definitely be autonomous operations and would require large search fields-of-view. Category 3 would include both autonomous operation and acquisition before launch.

Category 1 is typical of systems such as the cannon-launched missile and aircraft dispenser missiles; category 2 includes RPV and aircraft-launched missiles. Category 3 includes aircraft or helicopter launched missiles, while category 4 includes the hand-held thermal viewer.

Table 3-1 describes the general FOV, IFOV, acquisition range, and required array size (for strapdown operation) for some typical scenarios where we have assumed a three-foot IFOV at the target (typical for armored vehicle recognition). The number of detector elements increases in general in going from categories 1 to 4.

From this table we can see that the requirements for the array size are quite large and range from 180 x 90 elements to 525 x 260 elements. Recall, however, that these numbers are the requirements for a strapdown

TABLE 3-1. OPERATIONAL REQUIREMENTS FOR STARING FOCAL PLANE IMAGES

	Category 1	Category 2	Category 3	Category 4
Engagement	Overhead to 45° from vertical	30 - 50° from vertical	>60° from vertical	Ground based imaging
Delivery Technique	- Cannon missile - Up and over - Aircraft/ Dispenser	- RPV - Aircraft launched missiles - Small cruise missiles	- Aircraft or helicopter launch - Cannon launch - Fly-out	- Hand-held/ Portable imagers - Individual serve Weapon sight
Acquisition Range	500-1000 ft	1500-5000 ft	3000-5000 ft	1000-5000 ft
Search FOV	45° at min. altitude 10° at max. altitude	20° x 10°	20° x 10°	8° x 4°
Sensor IFOV	5 mr at min. altitude 0.5 mr. at max. altitude	0.5 - 1 mr	0.5 - 1 mr	0.25 - 1 mr
Array Size (Strapdown)	160 x 160 350 x 350	700 x 350 350 x 175	700 x 350 350 x 175	560 x 280 140 x 70

system. The array size requirements vary considerably in the case of automatic acquisition of armored targets since the guidance can be addressed in terms of two general approaches:

- Unresolved target acquisition
- Resolved target acquisition

Unresolved target acquisition depends on a single target feature to uniquely distinguish it from false targets and background clutter. If this criterion is satisfied, unresolved target acquisition approaches offer a simple, state-of-the-art solution to target acquisition.

Resolved target acquisition depends on the criterion that the target is an anomaly in the background, i.e., that the target is different. The anomalous characteristics of the target are defined in terms of several target features. The analysis of these features requires several sensor resolution elements on the target and/or more than one sensing medium to examine the target (detect features which are spectrally dependent). When compared to unresolved target acquisition, resolved target acquisition approaches should have much higher performance. However, the high performance of resolved target acquisition approaches may be offset by cost and technological immaturity. A fair comparison of unresolved and resolved target acquisition approaches can only be made if one measures the total effectiveness of the weapon system to which the two approaches are applied.

RESOLUTION REQUIREMENTS

Unresolved Acquisition Approach

Unresolved target acquisition depends on the existence of one target feature which is uniquely different from background clutter and false targets. Infrared sensors almost always use the hot target exhaust and its spectral distribution as the target feature. The target feature can be discriminated from background clutter and false targets by using two-color and spatial discrimination techniques. The resolution requirement for an unresolved target acquisition sensor is based on the target feature (hot spot), plus background vs. background, plus clutter contrasts vs. the signal-to-noise capability of the sensor. In a 200 K ft^2 search area, a 40°C target feature can provide a probability of detection, $P_D > 0.8$, and a probability of false alarm, $P_{FA} < 0.1$, if the target feature is three to five percent of the instantaneous field of view of the detector. Using typical dimensions quoted for Soviet target features, the ground resolution of the unresolved target acquisition is then approximately 80 to 100 ft^2.

Resolved Acquisition Approach

Many researchers in the field of automatic target acquisition have attempted, with varying degrees of success, to detect and recognize a target in the background. Features used by researchers include target shape and size, frequency distribution, brightness (including spectral distribution), structural details, etc. The use of these or other detail target features requires

that the target be resolved into several resolution elements. For this report, the criteria for visual target detection and recognition is used with the assumption that machines may someday equal this eye-brain performance. Johnson[1] has reported that three to four "cycles" on a display are sufficient to enable target recognition. This means that at least 16 resolution elements must be imaged on a 10 x 20 ft target for a ground resolution of at least 12.5 ft^2.

IMPLEMENTATION APPROACHES

Table 3-2 illustrates resolution requirements for strapdown and gimballed seeker configurations applied to the three weapon categories. In each case it is assumed that target acquisition must take place at the specified acquisition range of that weapon. This means that category 1 weapons must acquire 450 to 500 ft from the target, category 2 weapons must acquire 1500 ft from the target, and category 3 weapons must acquire 7000 ft from the target. For category 3 weapons, this places an untenable requirement on focal plane dimensions, optics (0.4 mr IFOV), and information data rates. An alternate approach to category 3 weapons would be to guide (by some other means) to the suspected target area and then operate as category 1 weapons.

From Tables 3-1 and 3-2 we can see that the focal plane requirements for staring arrays range from less than 32 x 32 elements to greater than 500 x 500 elements depending upon the particular application and the mode of operation. The smaller arrays are applicable primarily to missile seeker systems and, therefore, represent more near-term applications for the first generation of staring focal plane systems.

---

[1] Johnson, J., Proceedings of Image Intensifier Symposium, Fort Belvoir, Virginia, October 1958.

TABLE 3-2. FOCAL PLANE REQUIREMENTS (NUMBER OF PIXELS) FOR RESOLVED AND UNRESOLVED TARGET ACQUISITION OF ARMORED VEHICLES

UNRESOLVED TARGET ACQUISITION

Weapon Category	Strapdown	Gimballed
1	50 x 50	5 x 5
2	82 x 82	14 x 14
3	700 x 700	62 x 62

Assumptions:
- IFOV = 10 x 10 feet on ground
- Gimballed assumes 6-degree search window

RESOLVED TARGET ACQUISITION

Weapon Category	Strapdown	Gimballed
1	175 x 175	14 x 14
2	280 x 280	46 x 46
3	1225 x 1225	216 x 216

Assumptions:
- IFOV = 3 feet on ground
- Category 1 acquisition range = 500 ft; category 2 = 1500 feet; category 3 = 7000 feet

Since the smaller array sizes represent a near-term application, Table 3-3 lists various anti-armor weapons systems which are applicable to automatic target acquisition using TE-cooled staring focal plane technology.

Table 3-4 lists the general focal plane requirements for a typical missile seeker and hand-held thermal viewer system. Of particular importance is the requirement for a cell size of 1 x 1 mil to 2 x 2 mil which is necessary to keep the system weight to a minimum.

TABLE 3-3. LIST OF ANTI-ARMOR WEAPON SYSTEMS APPLICABLE TO AUTOMATIC ACQUISITION TECHNOLOGY

Name	Service	Type
GSRS/TGMW	ARMY	Rocket launched, terminally guided system; may be unitary, cluster warhead, or submissile.
SADARM	ARMY	Cannon launched; long standoff warhead.
ERAM	AF	Aircraft dispenser delivery; mine, pop-up and kill.
CYCLOPS	AF	Aircraft dispenser delivery; long standoff warhead or several submunitions.
WASP	AF	Aircraft delivered; either dispenser or unitary missile; impacts target; ground-to-ground or air-to-ground.
TOW/AHAM	ARMY	A missile with unitary warhead. Wire guided (TOW) or beam rider (AHAM).
Dragon	ARMY	Ground-to-ground, lightweight, wire guided missile with unitary warhead.
Hellfire	ARMY	Air-to-ground missile with unitary warhead.
Maverick	AF	Aircraft launched missile with unitary warhead. Either TV or IR guided.
Fire and Forget	DARPA	Individual served ground-to-ground missile with uniting warhead. IR guidance.

TABLE 3-3. LIST OF ANTI-ARMOR WEAPON SYSTEMS APPLICABLE TO AUTOMATIC ACQUISITION TECHNOLOGY (concluded)

Name	Service	Type
FFAST	ARMY	Same as Fire and Forget except target reacquisition required for overhead attack.
Copperhead	ARMY	Cannon launched; unitary warhead; laser guidance.
TGP	ARMY	Cannon launched; unitary warhead with IR guidance.
Motherbird	DARPA	Long standoff aircraft or ground launched "smart missile" carrying submissiles. Smart missile guides to and acquires target(s); submissiles guide to target(s) impact.

TABLE 3-4. TYPICAL REQUIREMENTS FOR MISSILE SEEKER AND HAND-HELD THERMAL VIEWER SYSTEMS

	Missile Seeker	Hand-Held Thermal Viewer
Number of Detectors	128 x 128	256 x 256
Detector Size	1 x 1 to 2 x 2 mil	1.5 x 1.5 mil
Wavelength	4.2 or 5.0 μm	4.2 or 5.0 μm
Fill Factor	90%	90%
Optics	f/1.5	f/1.5
Optics Diameter	2 in.	3 in.
IFOV	0.5 x 0.5 mrad	0.3 x 0.3 mrad
FOV	3.7 x 3.7 deg	4.4 x 4.4 deg
Frame Rate	30-60 fps	60 fps
Temperature (Focal Plane)	195 K	195 K
Dynamic Range	60 dB	60 dB

SECTION IV

FOCAL PLANE DESIGN

GENERAL CONSIDERATIONS

There is a broad class of requirements for the two-dimensional sampling of object space in the infrared portion of the spectrum. Typical examples include night viewing requirements, day/night guidance of missiles, and threat detection. Currently, the majority of the systems developed to meet these requirements employ a detector array with a scan mechanism to scan the image across the detectors such that the total field of view is systematically viewed. The development of the charge-coupled device (CCD) concept and its application to the multiplexing of IR detectors provides a basis for the development of two-dimensional non-scanned detector arrays. However, there are certain operational differences between scanning and non-scanning systems that must be taken into account. In particular, the change in the signal integration time and the need to view reference signal sources must be considered.

With a direct injected CCD multiplexed focal plane, the photon-generated electrons are integrated at a CCD well to form the signal charge packet that is periodically shifted to the output amplifier. With a scanning system,

the integration time is less than or equal to the detector dwell time and is several orders of magnitude less than the frame time. With a five-micron cutoff detector, the total charge accumulated during the integration time is only a small fraction of the capacity of even the smallest well. However, for a staring system the detector dwell time is determined by scene motion and the integration time is the frame time. Under these conditions the overfilling of the integration well can be a problem.

Figure 4-1 shows the relationship between the maximum integration time and the incident flux density for BLIP detectors with and without a background suppression function. As an example, for a detector with a 4.2-micron cutoff cold shielded to an f/1 optics, the effective photon flux is 8.4×10^{14} photons/cm^2· second. Referring to Figure 4-1, the maximum integration time is limited to about one millisecond, whereas the desired frame time is typically 16-33 milliseconds. In fact, for TE cooled detectors where the detector is non-BLIP, the detector saturation current is comparable to the background current, thereby making the charge handling problem even more severe. The net result of this relationship is that a staring focal plane must have a relatively complex coupling circuit into the CCD, rather than the simple direct injection suitable for scanning arrays. The more complex input circuitry, in turn, has implications about the amount of CCD area required for each detector and hence, the ultimate size of the focal plane. The size of the focal plane, in turn, affects the heat load on the TE cooler. These factors must be considered in assessing staring arrays for applications with high pixel counts.

FOCAL PLANE ORGANIZATION

High density IR staring focal planes can be realized through the development of charge coupled device (CCD) technology. This technology

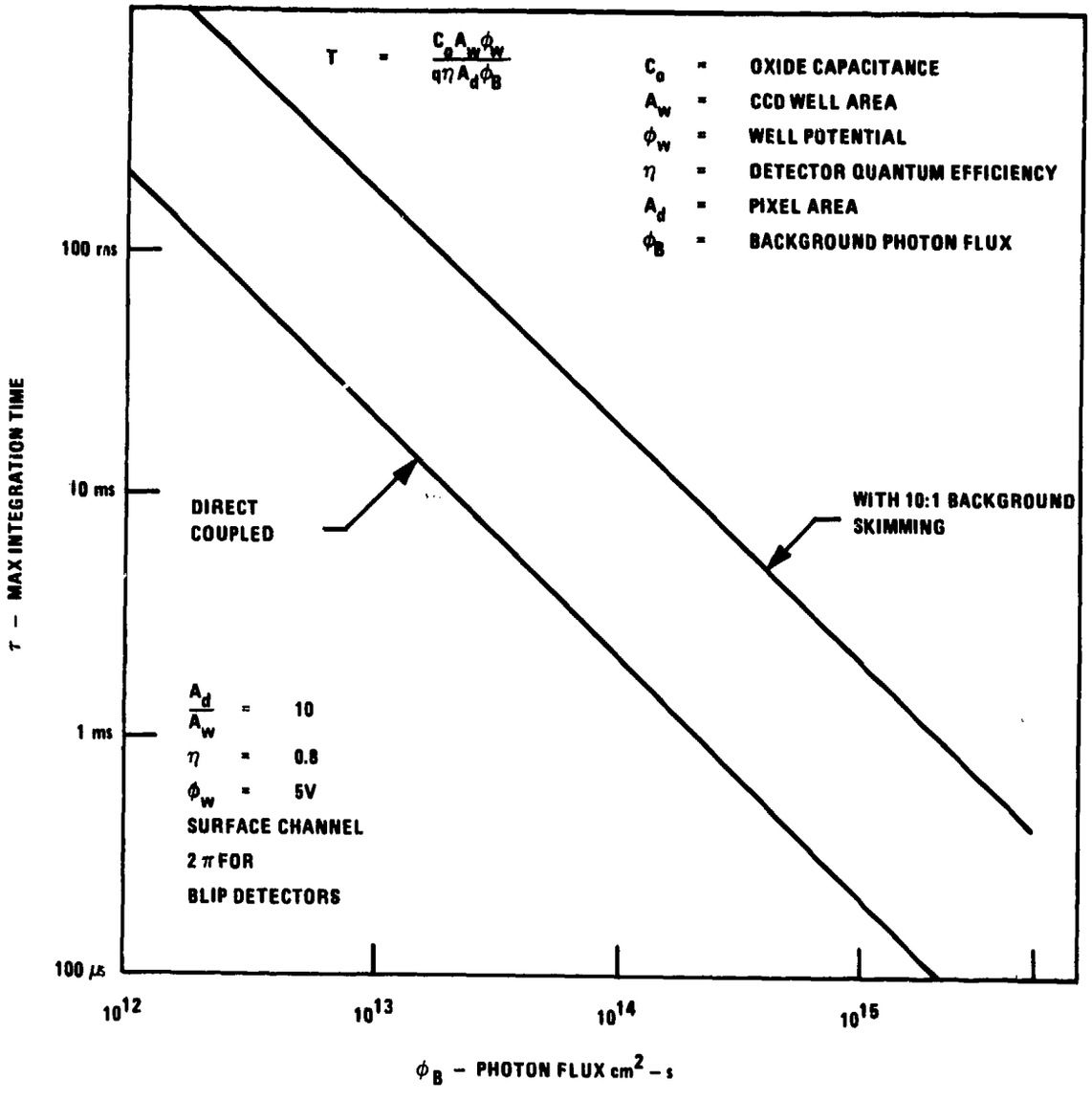

Figure 4-1. Maximum Integration Time vs. Background Photon Flux for Direct Coupled BLIP Detectors into Single Input Well

not only permits the detector signals to be multiplexed off the focal plane but can also act to implement such critically important signal processing functions as background suppression, responsivity normalization, anti-blooming, thresholding, frame comparison, MTI functions, correlation, and convolution. Since much of the signal processing can be done either on or off the focal plane, the question becomes one of determining the partitioning of the processing functions to determine where they would best be performed. This determination is made by considering real estate limitations, photolithography limitations, and power requirements.

The signal readout can be organized through variety of techniques, one of which is shown in Figure 4-2. In this case, the detector signal is integrated into the appropriate storage wells of the CCD, and at the end of the integration period (i.e., frame time) all of these signal charges are simultaneously dumped into the vertical shift registers. Since the charge storage wells can receive signals independently of the shift registers, the detector signal can be integrating the next frame of information while the vertical shift register parallel shifts the first frame signal into the high-speed horizontal readout register and into the output amplifier stage. Assuming a frame rate of 1/60 second, we can calculate the clocking speed requirements for the horizontal and vertical shift registers as a function of the array size (Table 4-1). These data rates represent relatively modest CCD clocking requirements.

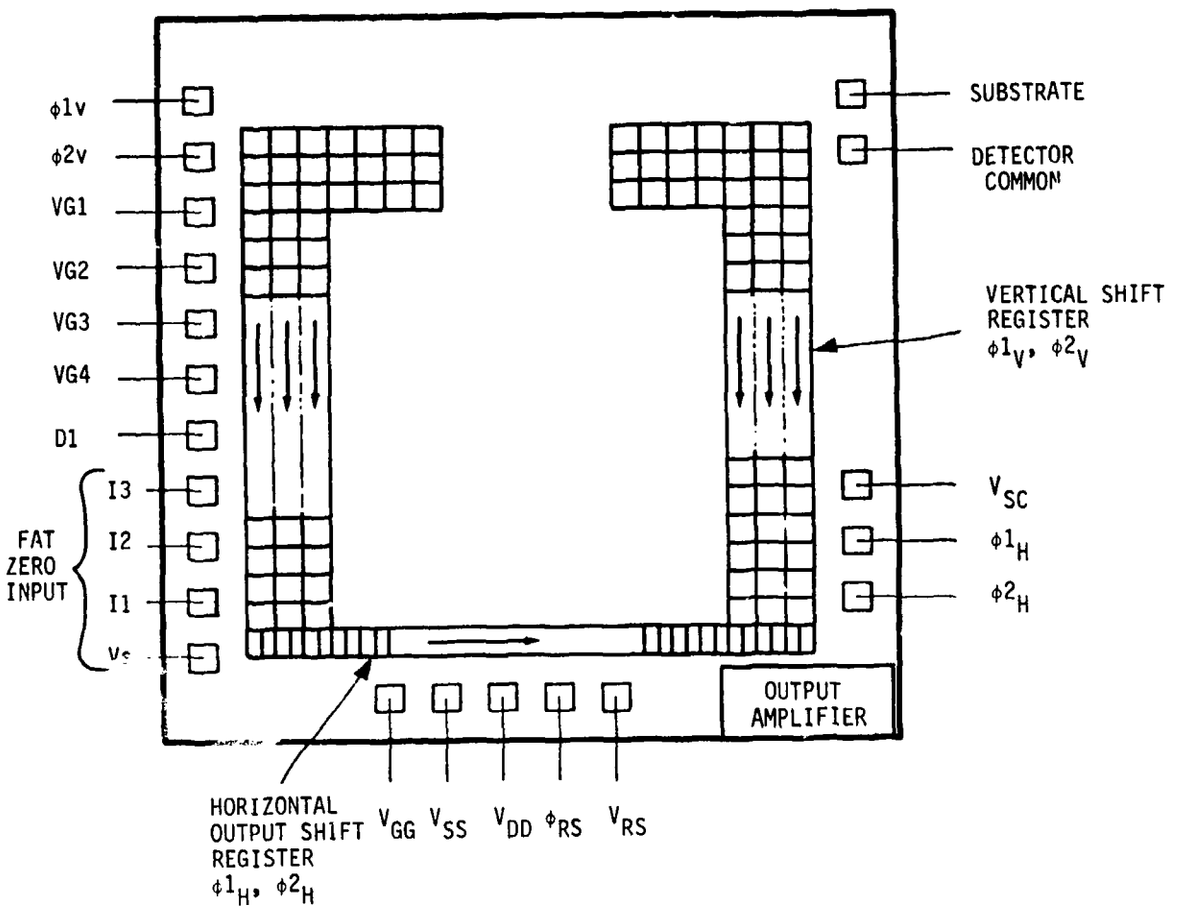

Figure 4-2. Typical Parallel/Series Staring Detector/CCD Arra yout

TABLE 4-1. FOCAL PLANE OUTPUT DATA RATES

	NUMBER OF DETECTORS		
	64 x 64	128 x 128	256 x 256
Vertical Register	3.8 kHz	7.7 kHz	15.4 kHz
Horizontal Output Register	246 kHz	0.98 MHz	3.9 MHz

Operation of this type of focal plane readout organization has been demonstrated on Honeywell's 2181 CCD chip shown in Figure 4-3. This chip is a 32 x 32 element IR focal plane readout chip which is an N-channel, buried channel structure that includes a bias-charge injector circuit at the end of each parallel shift register. The bias-charge injector is used to evaluate the chip performance during testing and also to inject a bias charge to improve transfer efficiency (if necessary). The photo also shows the detector substrate contact pads and the detector/CCD alignment marks necessary for alignment of the detector with the CCD during the flip-chip operation. The chip has a pixel size of 4 x 4 mil with 1 x 1 mil bump interconnects.

Figure 4-4 shows a corner detail of the 2181 CCD which shows the parallel-to-serial transfer lines and the source-follower output amplifier.

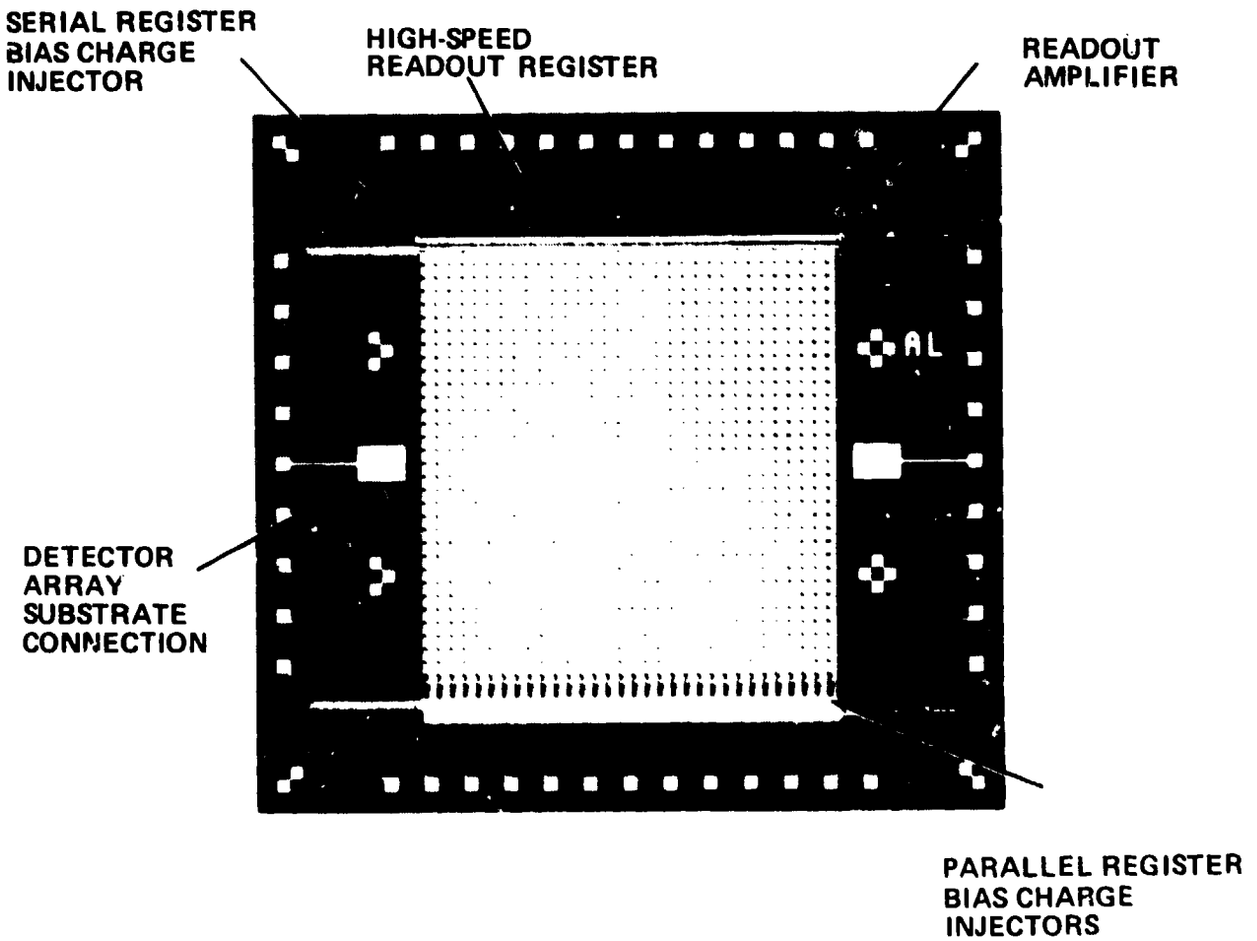

Figure 4-3. Honeywell 2181 Focal Plane CCD Chip

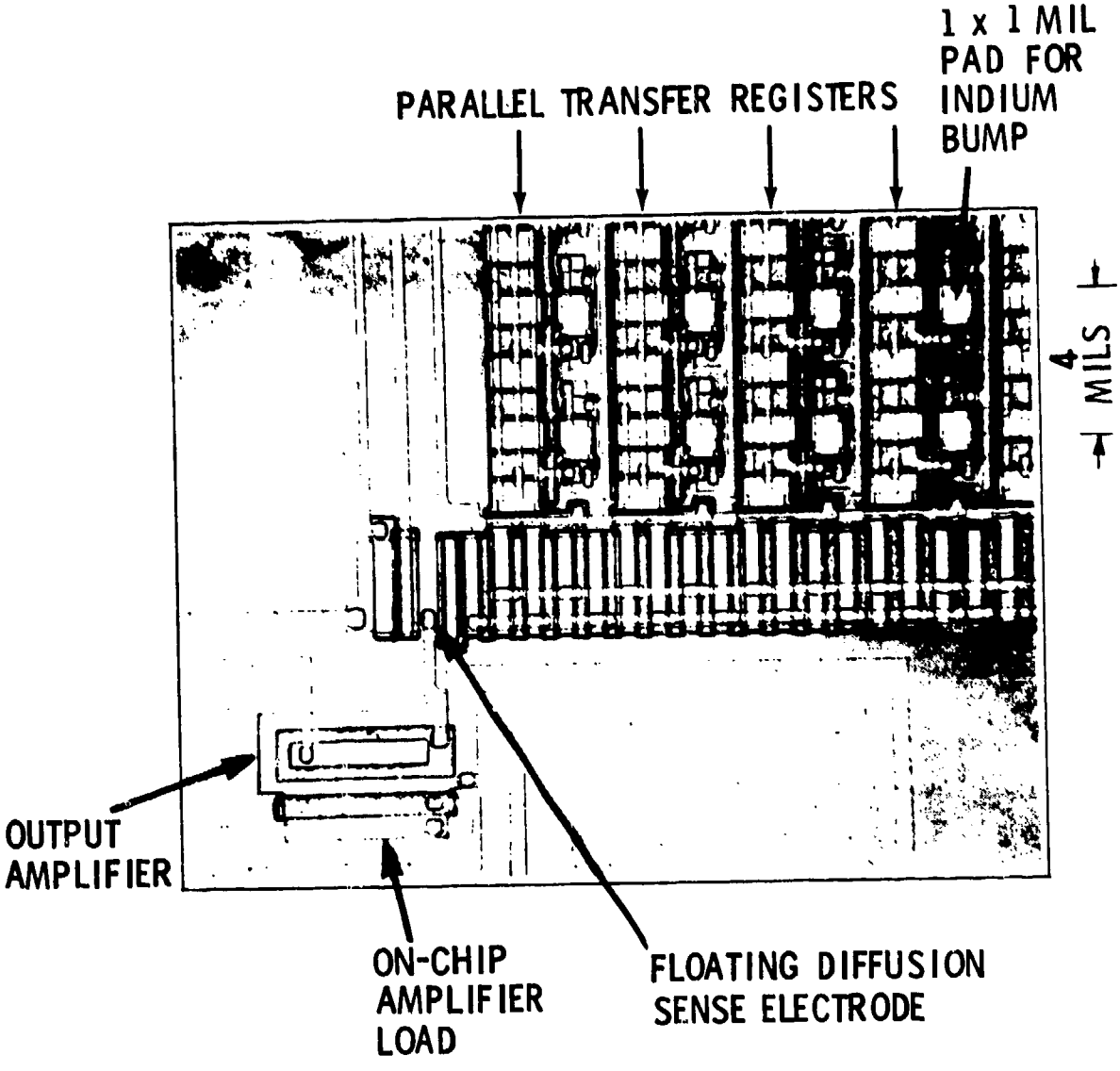

Figure 4-4. Corner Detail of 32 x 32 CCD Focal Plane Electronics Chip Showing Floating Diffusion Output Amplifier and Parallel-to-Serial Register Transfer Lines

FACTORS INFLUENCING FOCAL PLANE SIZE

The maximum, or optimum, number of detectors which can be placed on the focal plane is determined by many factors, including the power dissipation limitations, photolithography limitations, and processing yields. These factors are indicated in Figure 4-5 and can be conveniently broken down into four main factors:

- Detector density
- CCD processor cell and chip size
- Number of detector chips per CCD processor
- Number of detector/CCD chips per focal plane

Here, the CCD chip size and detector density will determine a module size. A multiplicity of these modules may be assembled into an array of modules which then make up the complete focal plane assembly.

Backside Illuminated Arrays

In hybrid focal plane structures, several approaches can be taken to mechanically interconnect the detectors with the CCD array. One technique shown in Figure 4-6 shows the method of bump-mounting the detectors to the CCD. In this case, indium bumps are electroplated onto the detector diodes which have been fabricated on an IR transparent substrate. Indium bumps are similarly plated on the input nodes to the CCD, and the detector and CCD array are then flip-chip bonded together by thermo-compression mating. Figure 4-7 shows a photograph of a 32 x 32 element PbTe detector array fabricated on a BaF_2 substrate which has been

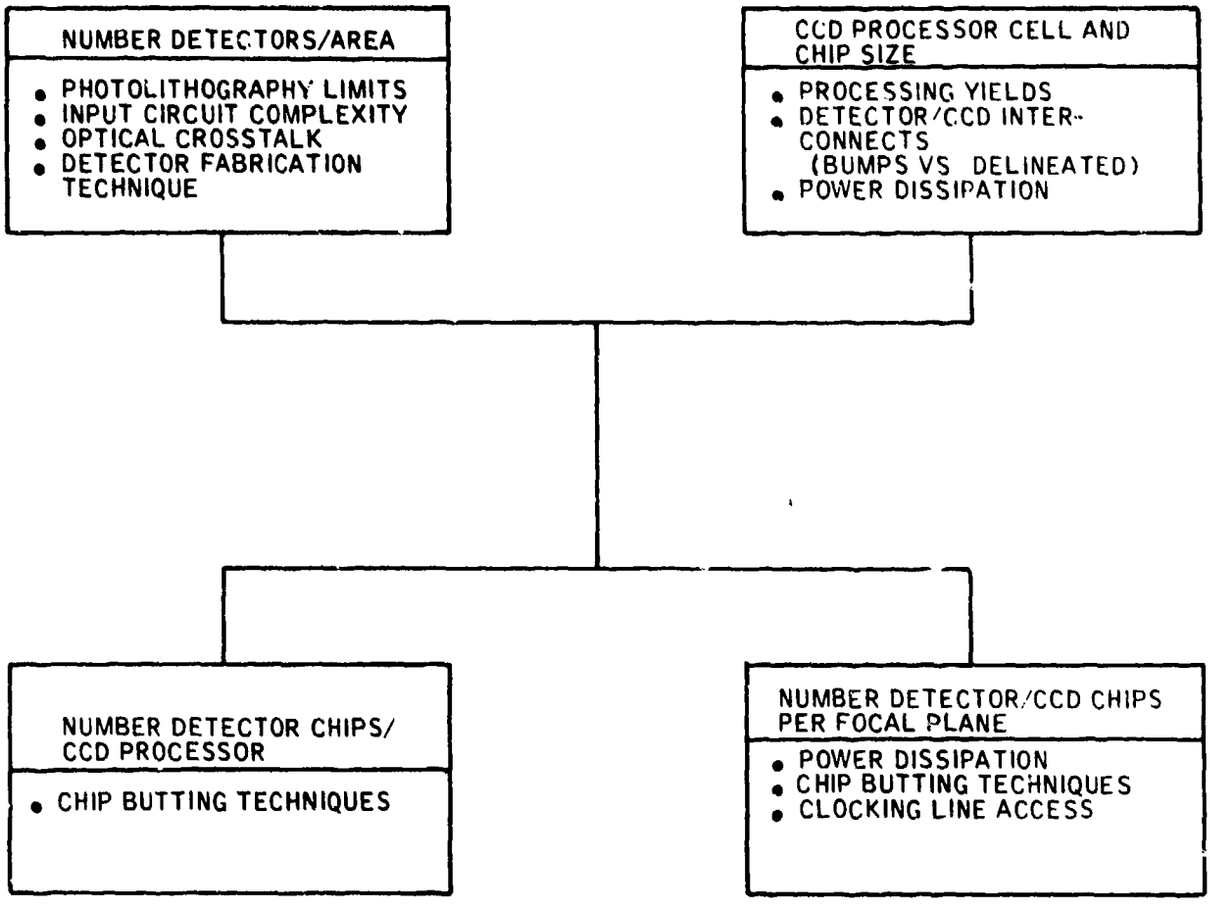

Figure 4-5. Factors Influencing Focal Plane Size and Detector Density

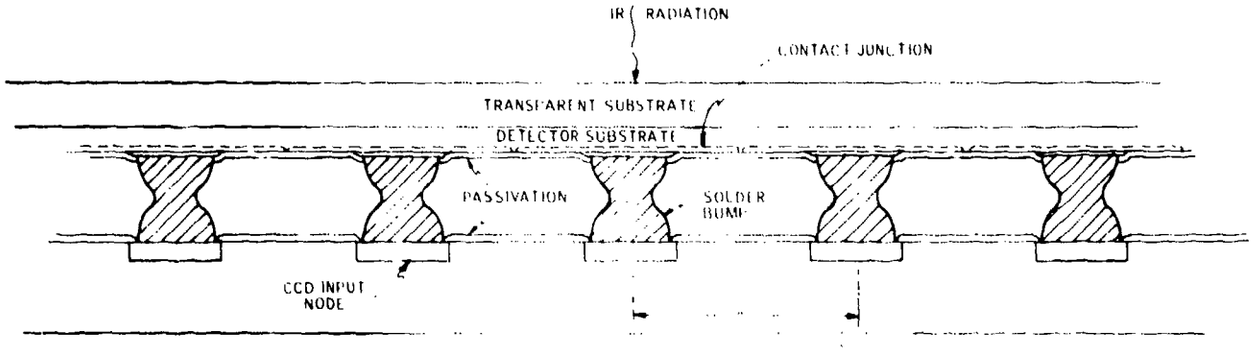

Figure 4-6. General Configuration of the Solder Bump Detector/ CCD Interface Used for Backside Illuminated Detector Structures

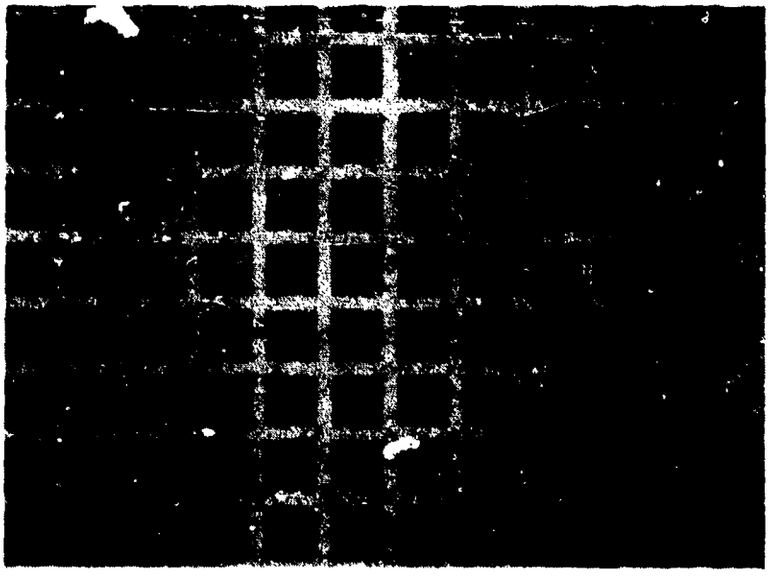

Figure 4-7. 32 x 32 PbTe Detector Array with Electroplated Indium Bumps

electroplated with indium bumps and is ready for mating to a 32 x 32 element CCD array. Detectors are on four-mil centers, and the indium bumps are 1 x 1 mil.

This bump interconnect approach used in conjunction with backside illuminated detectors is capable of making detector arrays on as small as 1 x 1 mil centers since the only size limitation is with the minimum bump size and spacing that can be fabricated. Current technology permits fabrication of bumps 0.5 x 0.5 mil on 1 mil centers.

Front Side Illuminated Arrays

An alternate approach to detector/CCD interconnects is shown in Figure 4-8. With this technique, bulk semiconductor materials such as HgCdTe are bonded onto the passivated CCD substrate. After the HgCdTe has been polished to its final thickness ($\simeq 10\mu m$), channels are etched in the material to gain access to the CCD input contacts protruding through the CCD passivation layer. An insulating layer protects the etched edge of the HgCdTe and an evaporated top contact is then photolithographically defined which connects the detector top contact to the CCD input contact.

With this approach the limiting detector density is primarily determined by the etched channel width necessary for making the detector/CCD electrical interconnect. These critical dimensions are limited by current photolithography techniques. Figure 4-9 indicates the dimensions which determine the detector active area fill factor. Table 4-2 shows the projected dimensional factors along with the fill factors for various pixel sizes using conventional photolithographic printing techniques.

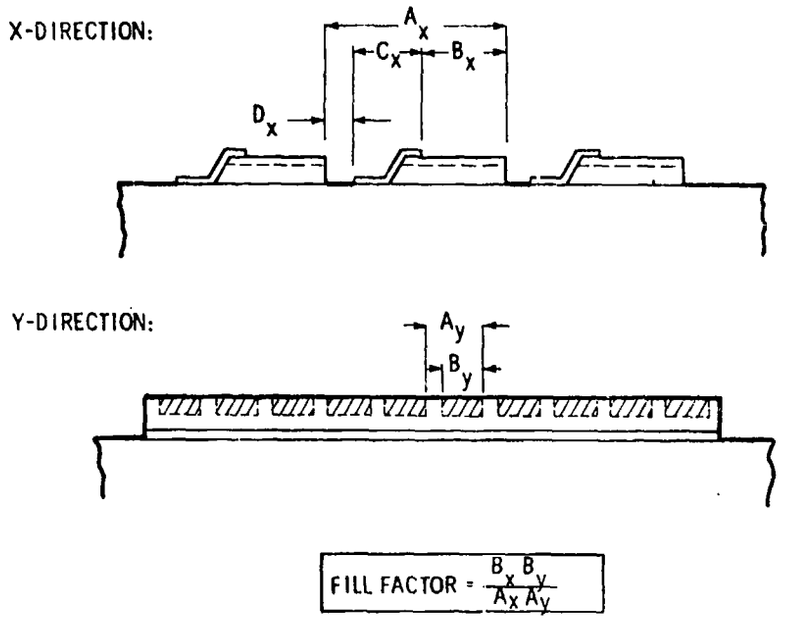

Figure 4-8. Planar HgCdTe Hybrid Focal Plane Structure

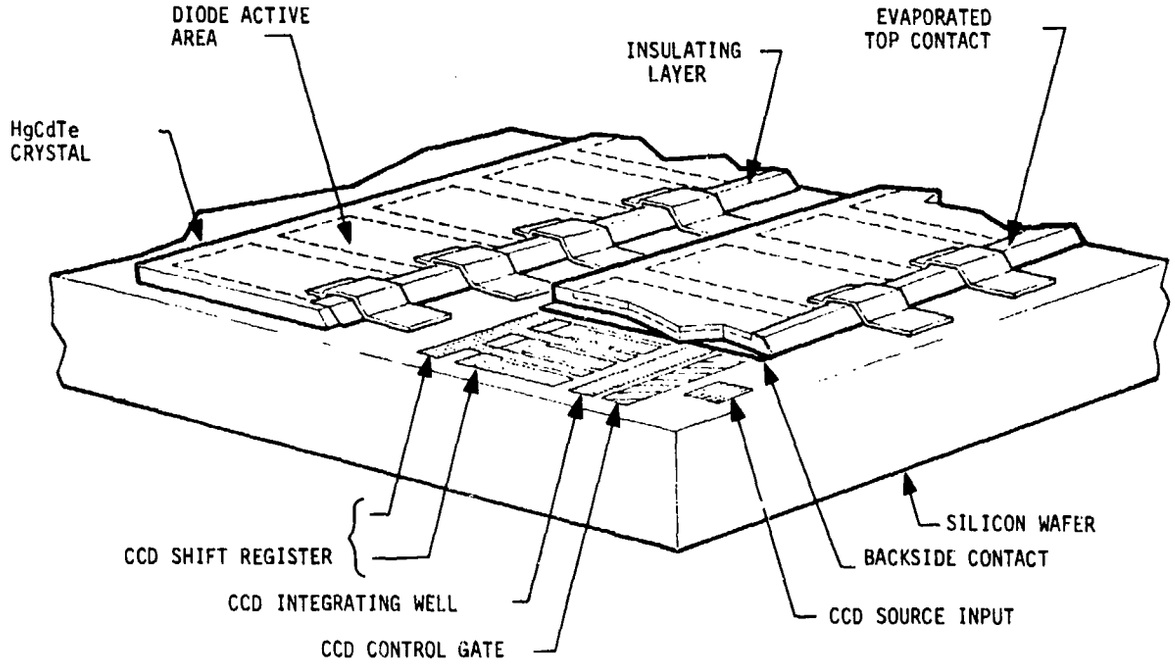

Figure 4-9. Fill Factor Considerations for Mosaic Arrays

TABLE 4-2. PROJECTED DETECTOR DIMENSIONS FOR PLANAR HYBRID STRUCTURE

PIXEL SIZE		DETECTOR SIZE		FILL FACTOR
Ax	Ay	Bx	By	(%)
0.001	0.001	0.0005	0.0007	35
0.002	0.002	0.0015	0.0017	64
0.003	0.003	0.0025	0.0027	75
0.004	0.004	0.0035	0.0037	81

It can be seen from this table that detector sizes down to 2 x 2 mil are attainable with moderate fill factors using this approach.

Optical and electrical cross talk from element to element can also place restrictions on the detector packing density. The primary source of cross talk in high-density staring focal planes will probably be due to the minority carrier diffusion length in the undepleted region of the detector. Detailed calculations of detector cross talk for thinned HgCdTe PV detectors are given in the following subsection which characterizes the tradeoff between detector size, quantum efficiency, and cross talk for detectors as small as 1 x 1 mil. Special detector designs have been developed which should permit cross talk levels of less than 5 percent between adjacent detectors while maintaining a high quantum efficiency on backside illuminated 1 x 1 mil detectors.

Cross talk effects due to transfer inefficiency in the CCD are represented by a function of the following form:

$$\text{Cross talk} = N\epsilon + \frac{(N\epsilon)^2}{2}$$

where N = number of transfers, ϵ = transfer inefficiency. For $\epsilon = 10^{-5}$ and a 128 x 128 SPS readout CCD, the cross talk term calculates to a negligible 0.5 percent.

Table 4-3 lists the salient features of a TE-cooled staring focal plane structure which will be characteristic of systems in the near future (2 to 5 years).

PV DETECTOR PERFORMANCE

The detector requirements for future TE-cooled backside illuminated focal planes are listed in Table 4-4.

Several PV detector materials are possible candidates for use in these applications; they include:

HgCdTe

InAsSb

InGaSb

PbTe

PbSnTe

TABLE 4-3. CHARACTERISTICS OF NEAR-FUTURE TE-COOLED FOCAL PLANE

CCD readout electronics
PV HgCdTe detectors
Bump interconnect detector/CCD coupling
Automatic background suppression
Antiblooming
Chip size = 600 x 500 mil
1 x 1 mil cells
512 x 375 pixels
Cross talk < 5 percent
Quantum efficiency > 50 percent
λ_c = 4.2 or 5.0 μm
Chip butting on two sides only (if needed)
30 to 60 fps frame rate

TABLE 4-4. DETECTOR REQUIREMENTS FOR FUTURE TE-COOLED BACKSIDE ILLUMINATED FOCAL PLANES

Detector size = 1 x 1 mil to 3 x 3 mil
Cross talk < 5 percent
Quantum efficiency > 50 percent
λ_c = 4.2 or 5.0 μm
Bump interconnects to CCD
Highest possible R_oA product
Operating temperature > 190 K
Thinned backside illuminated

The Pb-salt detectors are characterized by their relatively high capacitance/area (0.5 to 1.0 F/cm^2) and large thermal expansion coefficient. The large expansion coefficient of these detectors limits the ultimate size of the focal plane that can be fabricated with the flip-chip bump interconnect approach to approximately 200 x 200 elements. This differential expansion coefficient between detector and the silicon CCD substrate is greatly reduced with the other detectors listed and these can therefore be considered for eventual fabrication into very large arrays.

The first three detectors, HgCdTe, InAsSb, and InGaSb, must be considered as the three most promising detector materials for use in the TE-cooled staring focal plane application since all can theoretically meet similar

bandwidth and D* values. Table 4-5 lists the pertinent characteristics of the detector candidates.

The backside illuminated detector focal planes require the use of a thinned detector material so that the radiation is absorbed within the carrier diffusion length. Thinned detector arrays as well as "thick" HgCdTe detectors have been characterized and the results are presented here.

HgCdTe Detector Performance

Data at 193 K for over 230 small-area 3 to 5 μm HgCdTe n^+ -on -p junction photodiodes are shown plotted as a function of diode cutoff wavelength λ_{co} in Figure 4-10.

The open data points in Figure 4-10 are average values for the product of the junction zero-bias voltage impedance R_o and the optical area A_{op} (0.001 in. x 0.001 in. as determined by an optical mask) for three arrays. The more physically significant parameter would be R_oA_{diff}, where A_{diff} is the area over which lateral diffusion of electron-hole pairs takes place. Since the minority-carrier diffusion length L_e is on the order of 20 μm, A_{diff} could be as much as nine times larger than A_{op}; thus the R_oA_{op} product certainly is a conservative estimate of junction quality for these optically masked arrays. Because of the presence of the optical mask, it is not possible experimentally to determine A_{diff} by a spot scan.

TABLE 4-5. DETECTOR CHARACTERISTICS

Detector	λ_c (μm)	C/A ($\mu F/cm^2$)	R_oA (Ω-cm^2)	Notes
HgCdTe	5.0	0.01	5 at 193 K	Experimental data (1)
	4.2		25 at 193 K	Experimental (1)
InAsSb	4.8	0.5	13 at 195 K	Experimental (2)
InGaSb	5.0	0.1 - 0.01	7 at 195 K	Theoretical (3)
PbTe	4.7		22 at 170 K	Experimental (1)
PbSeTe	5.0	0.5	20 at 170 K	

(1) Honeywell IR&D programs

(2) 1978 IRIS proceedings

(3) NVL contract report DAAK70-76-C-0249

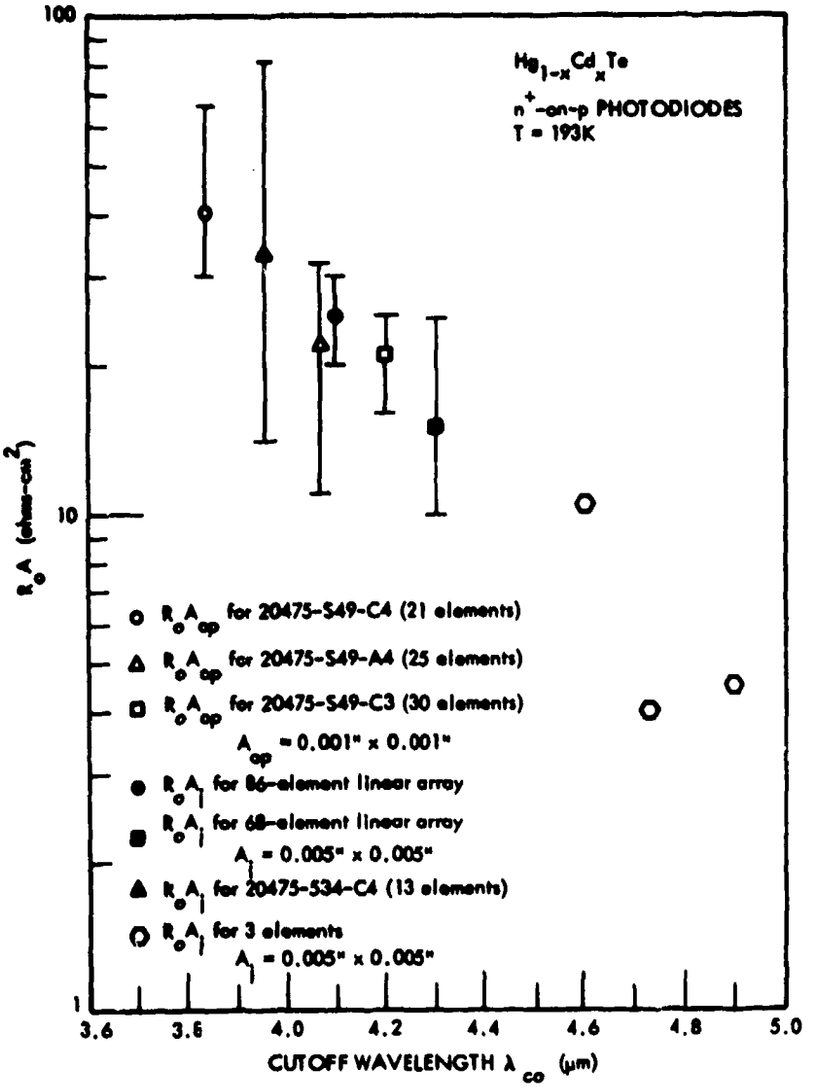

NOTE: THE DATA POINTS REPRESENT AVERAGE VALUES FOR THE ARRAYS LISTED, WHILE THE BARS REPRESENT THE RANGES OF THE VALUES.

Figure 4-10. R_oA Products for 233 n^+-on-p HgCdTe Small-Area Near-Infrared Photodiodes at 193 K, Plotted vs. Cutoff Wavelength

The remaining data in Figure 4-10 are for the R_oA_j product for two linear arrays and for some isolated elements. Here A_j is the actual junction implant area.

Extrapolation of these data to the case of a cutoff wavelength of 4.4 μm at 193 K indicates an "average" value for R_oA of about 13 ohms-cm^2 and a "best element" value in excess of 20 ohms-cm^2.

Figure 4-11 shows R_oA as a function of temperature for a 68-element linear HgCdTe photodiode array. The active area of each element was 0.005 in. x 0.005 in. The spectral cutoff of the array was 4.3 micrometers at 193 K. The average R_oA at 193 K was 15Ω-cm^2 with the best element having a value of 30Ω-cm^2. At 146 K the average R_oA was 900Ω-cm^2 with a best element at 2000Ω-cm^2. Analysis of the forward

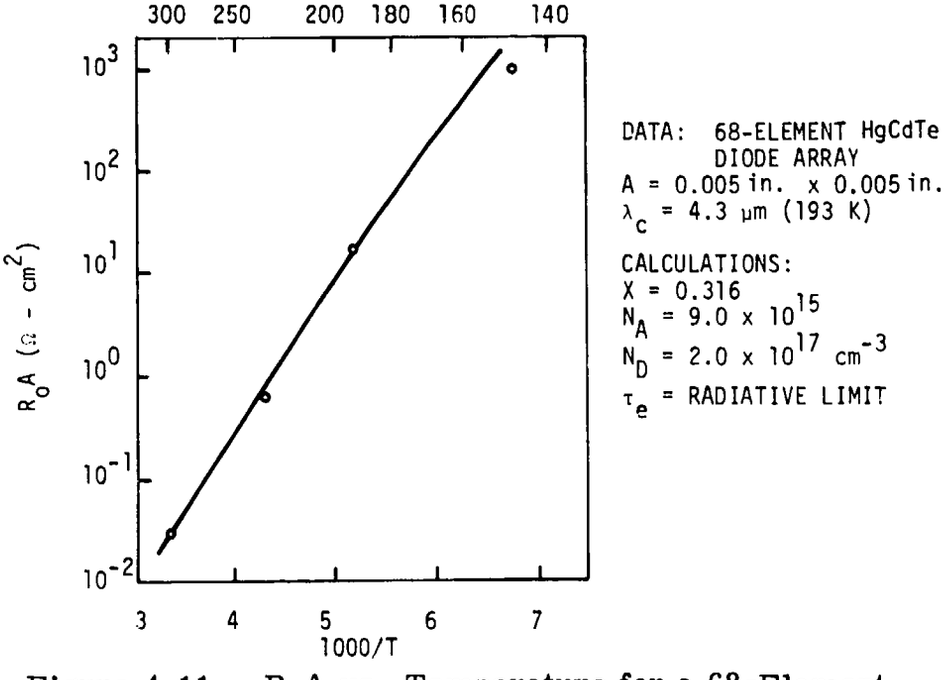

Figure 4-11. R_oA vs. Temperature for a 68-Element n^+-on - p Diode Array

current-voltage characteristics and of the relationship between R_o and the saturation current has verified that the diodes are in fact limited by diffusion current at temperatures above approximately 140 K.

Figure 4-12 shows R_oA as a function of temperature for an 86-element linear array of HgCdTe photodiodes with λ_c = 4.15 micrometers at 193 K. The average R_oA at 193 K was 25.4 Ω-cm^2 with one-sigma deviation of 6.8Ω-cm^2. At 146 K the average R_oA was 900Ω-cm^2. The best elements displayed R_oA = 35Ω-cm^2 at 193 K and 2000Ω-cm^2 at 146 K. The diodes were limited by diffusion current with minority carrier lifetime approaching the radiative limit. The R_oA continued to increase as the temperature was decreased to 77 K. The average R_oA at 77 K was 5×10^4 Ω-cm^2.

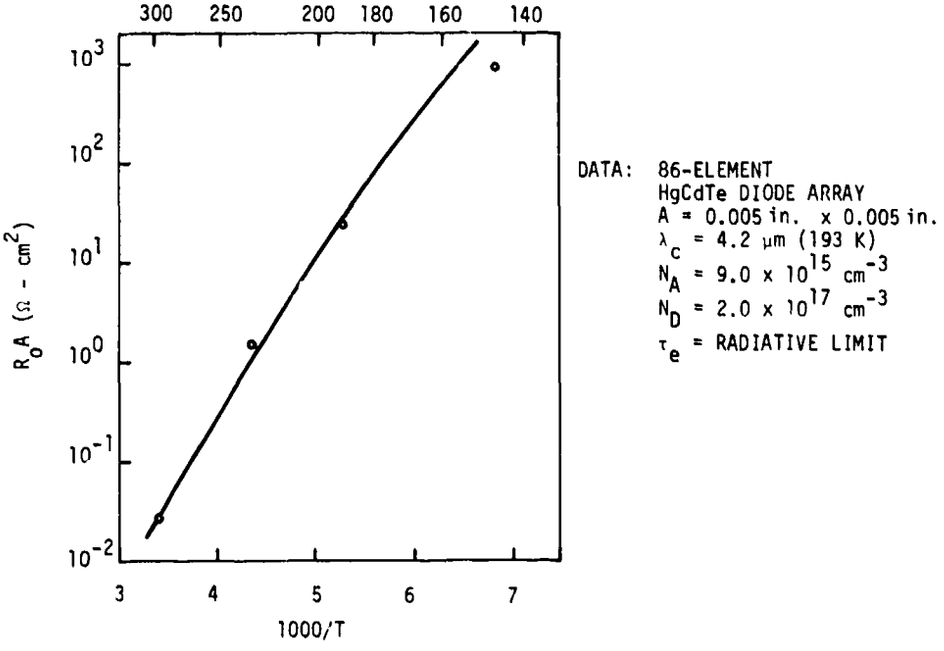

Figure 4-12. R_oA vs. Temperature for an 86-Element n^+-on - p Diode Array

Data for uniformity of R_oA product and current responsivity are shown in Figures 4-13 and 4-14.

Excellent diode I-V characteristics are obtained with these detectors. Figure 4-15 shows typical I-V characteristics for a 4.2 μm detector operating at T = 195 K. The quality of the detectors can be seen by observing the large increase in detector dynamic resistance upon reverse biasing the detectors (Figure 4-16). These excellent reverse bias characteristics allow the use of new input coupling schemes in which detector reverse biasing or operating off of zero bias is used.

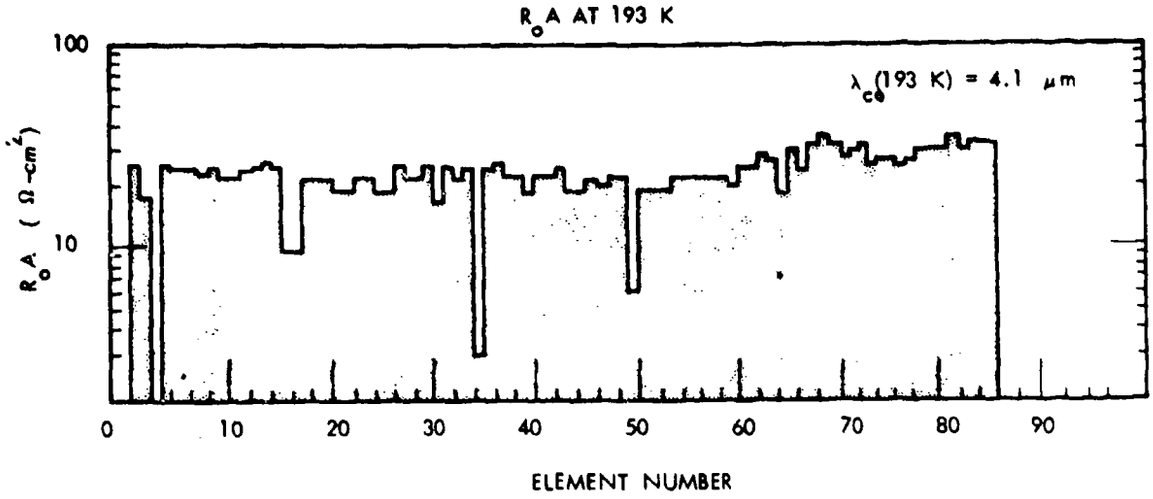

Figure 4-13. R_oA Data at 190 K for an 86-Element n^+-on - p HgCdTe Photodiode Array

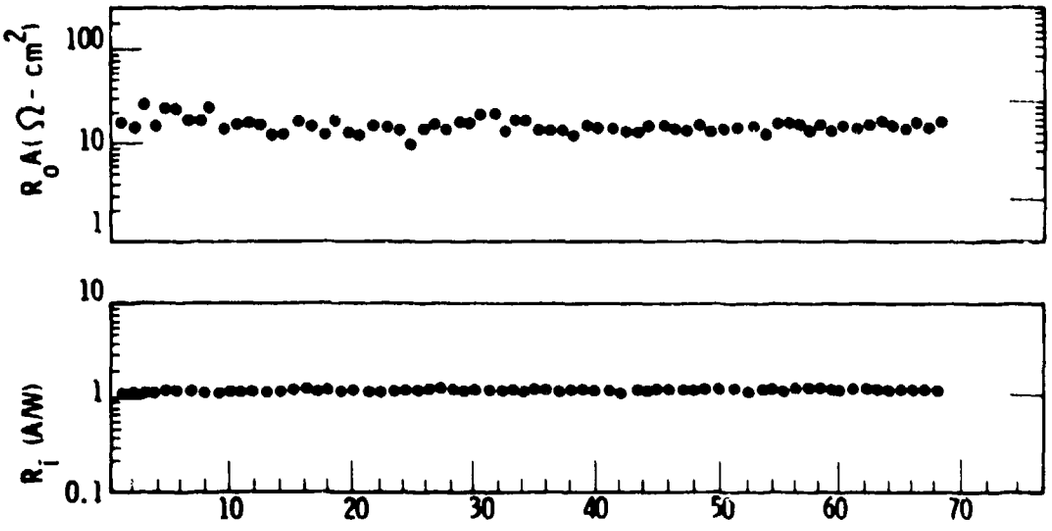

Figure 4-14. R_oA and Current Responsivity Data for a 68-Element n^+-on - p HgCdTe Photodiode Array

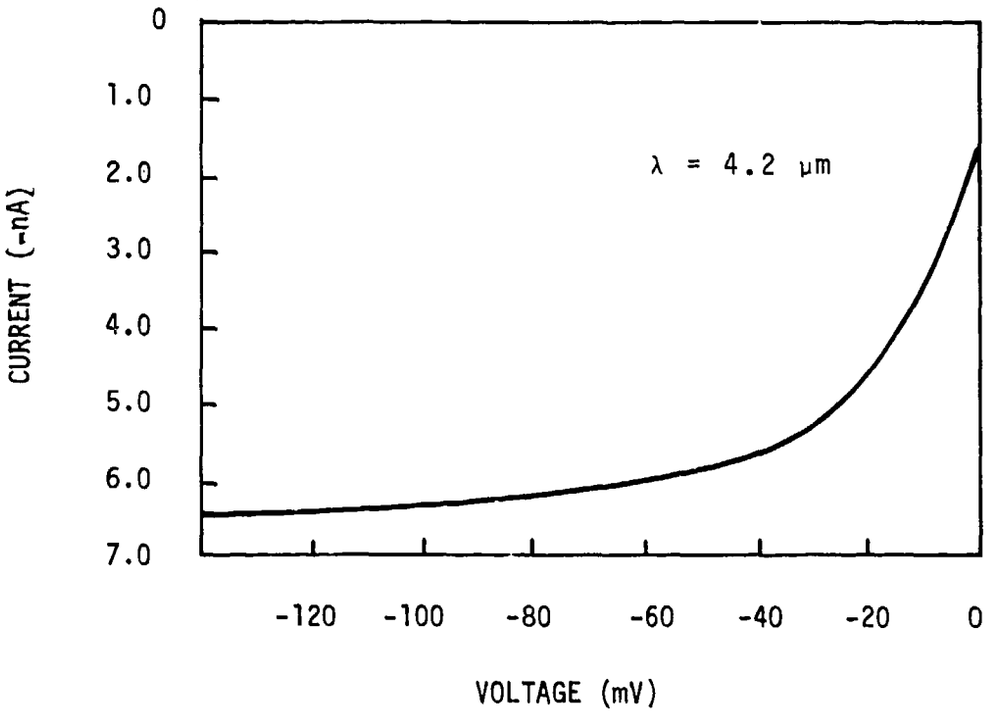

Figure 4-15. I-V Characteristics of R_oA = 26 ohm-cm^2 Diode

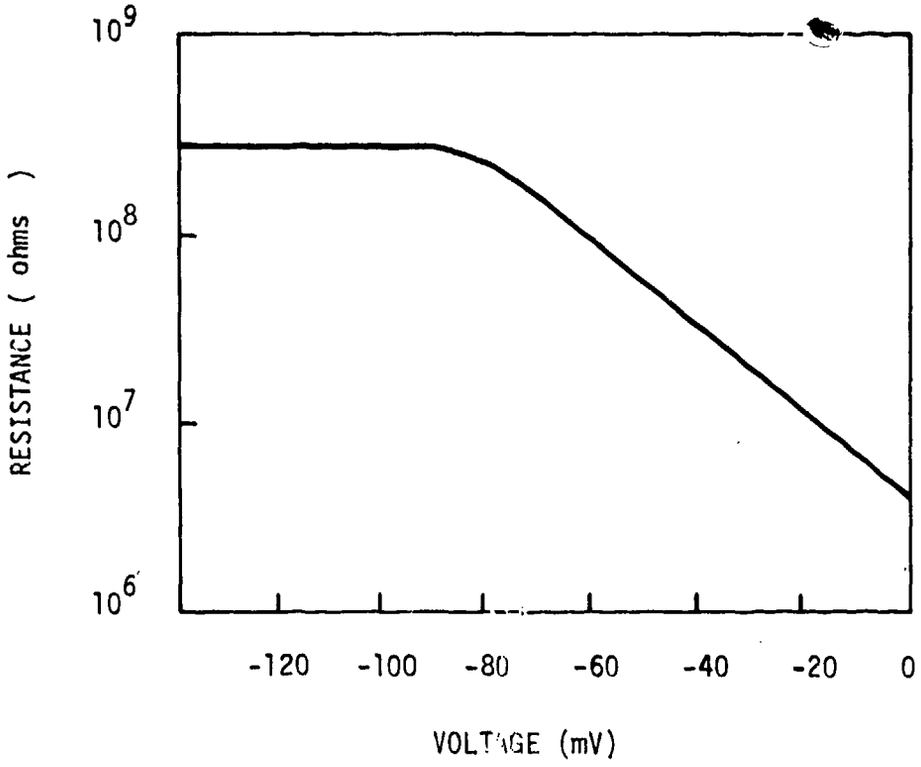

Figure 4-16. Increase of Detector Resistance with Respect to Reverse Bias (R_oA = 26 ohm-cm^2)

HgCdTe Performance on Thinned Diodes

Thin diodes are needed for hybrid focal plane configurations. To find out whether any structural or processing problems would arise with such thin photodiodes, experiments were performed with thin (<12μm) n^+ - on - p $Hg_{0.7}Cd_{0.3}Te$ photodiodes on both CdTe and Si substrates (made under NRL contract N00173-77-C-0355).

Three n^+-on -p $Hg_{0.7}Cd_{0.3}Te$ photodiodes were processed on CdTe substrates with an overall final thickness of about 10μm. Data for the average R_oA_j products of these "thin" arrays are shown in Table 4-6. Data for a conventionally processed "thick" array, from nearby starting material, are also included in Table 4-6. Each array contained junction areas A_j that ranged from $0.13 \times 10^{-4} cm^2$ to $4.8 \times 10^{-4} cm^2$.

The data show that R_oA_j products in "thin" n^+-on -p photodiodes on CdTe substrates can be as large as those obtained on conventionally processed "thick" structures.

A p-p^+ backside layer was not included in these thin photodiode arrays. The backside of these thin arrays' p- region was treated with a ZnS sputtered layer, which is known to accumulate p-type HgCdTe, so that some degree of isolation of the minority-carriers from the backside surface probably was present. Because the thin p-type region is less than a minority-carrier diffusion length from this backside surface, the R_oA_j product will depend on this degree of accumulation.

Detector Design Considerations

Figure 4-17 shows a cross sectional diagram of a backside illuminated detector array. Several key items are of particular importance in the design of the detector array. They are:

- Detector substrate
- Detector/substrate adhesion
- Quantum efficiency

TABLE 4-6. R_oA_j DATA FOR n^+-on - p $Hg_{0.7}Cd_{0.3}Te$ PHOTODIODES

	R_oA_j Product (ohms-cm^2)		Number of Elements	λ_{co} (μm)	λ_{peak} (μm)
	Average	Standard Deviation			
"Thick" Array					
20475-534-C4	34.4	20.72	13	3.96	3.70
"Thin" Arrays					
20574-533-3DE	26.5	9.65	42	4.02	3.70
20574-533-4AB	19.7	8.28	37	4.02	3.80
20574-533-4DE	34.3	7.73	39	4.04	3.80

All data for T = 193 K

Note: The "thick" array was processed by conventional techniques. The "thin" arrays processed on CdTe substrates were about 10 μm in overall thickness.

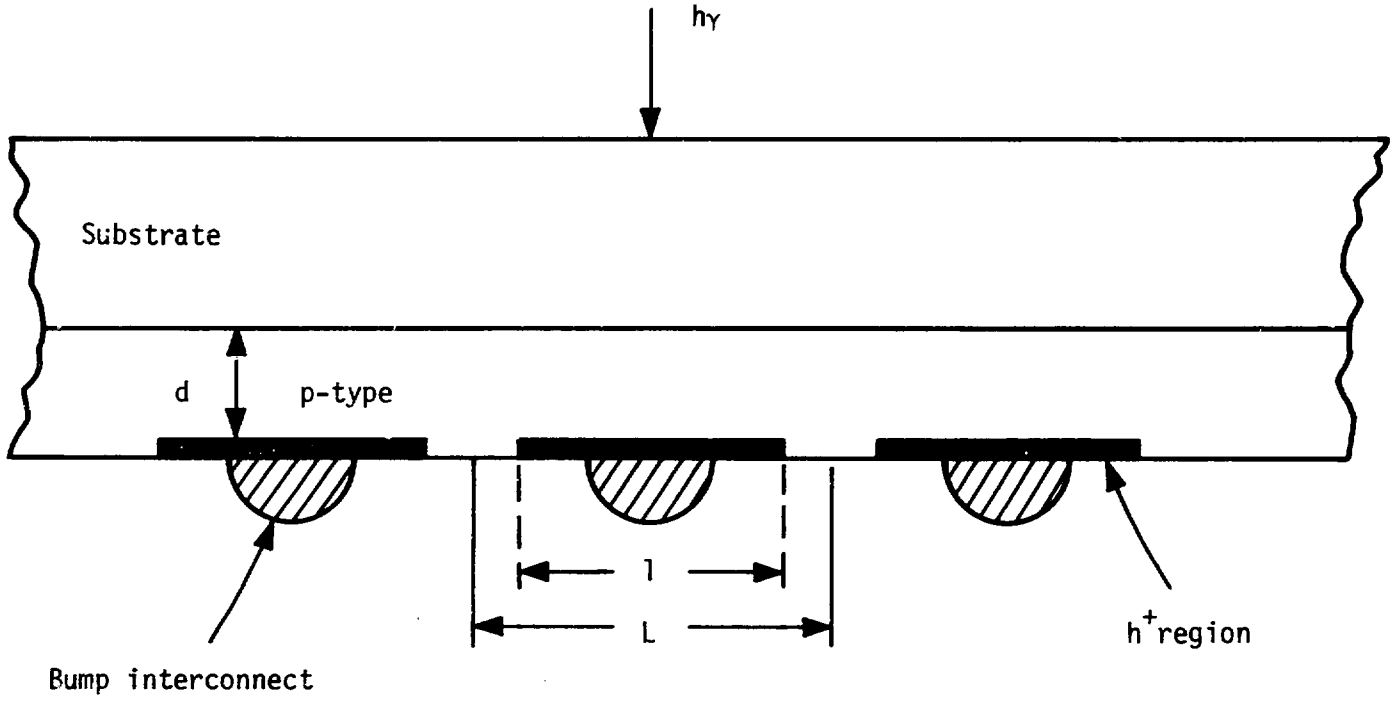

Figure 4-17. Cross Sectional Diagram of Backside Illuminated Detector Array with Bump Interconnects

- Crosstalk
- Detector thickness

Detector Substrate

The detector substrate can be either an integral part of the detector array (i.e., InAsSb epitaxially grown on GaSb substrates or epitaxial HgCdTe on CdTe substrate) or a separate material where the detector is attached (via e.g., IR transparent epoxy) to an IRTRAN or sapphire type of substrate. The substrate selection is based upon thermal expansion, or detector growth, compatibility.

The selection of the substrate material can act to modify the detector spectral characteristics. Figures 4-18 and 4-19 demonstrate this effect. Figure 4-18 shows the spectral response of a 4.8μm detector which has been attached to an IRTRAN II (ZnS) substrate. It can be seen that the spectral response is characteristic of the HgCdTe detector alone with the exception of some small "dips" in the response due to multiple interference effects with the thin epoxy layer. Figure 4-19 shows the spectral response of a 5.3μm detector which has been epoxied down to an HgCdTe ($x = 0.4$) substrate. In this case the spectral response goes to zero at the long wavelength cutoff of the substrate which is at about 3μm. The dips observed are again multiple interference effects between the substrate, epoxy, and detector layers and are not due to absorption effects.

The detector thickness, quantum efficiency and crosstalk are closely interrelated to one another and require careful analysis to achieve an optimum performance focal plane.

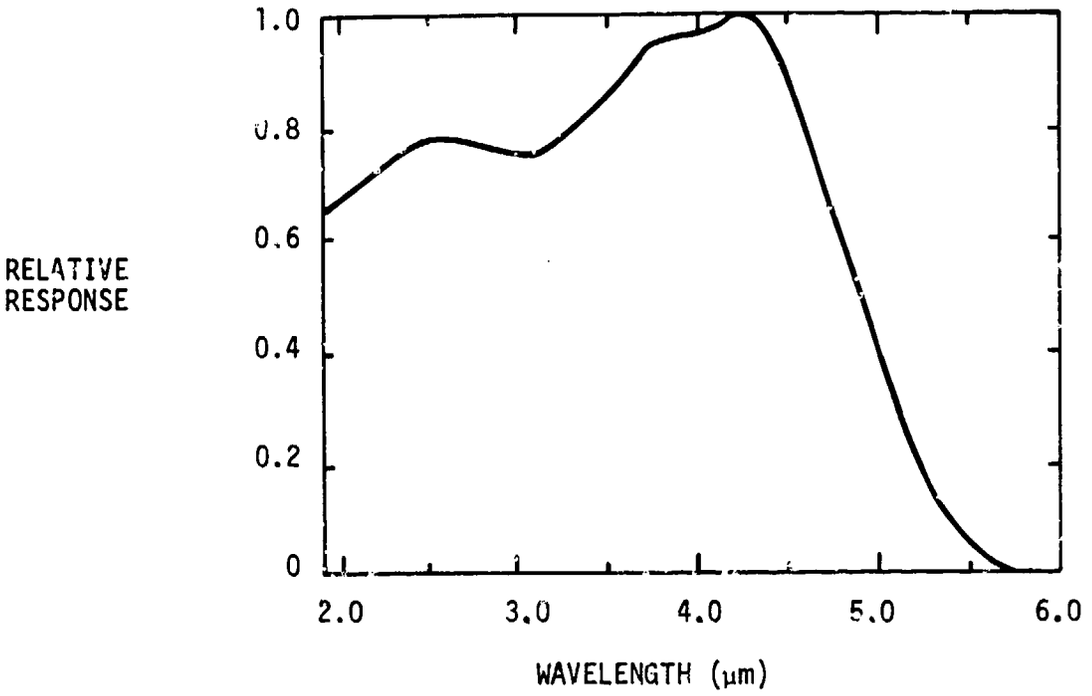

Figure 4-18. Spectral Response of Backside Illuminated HgCdTe on IRTRAN II Substrate

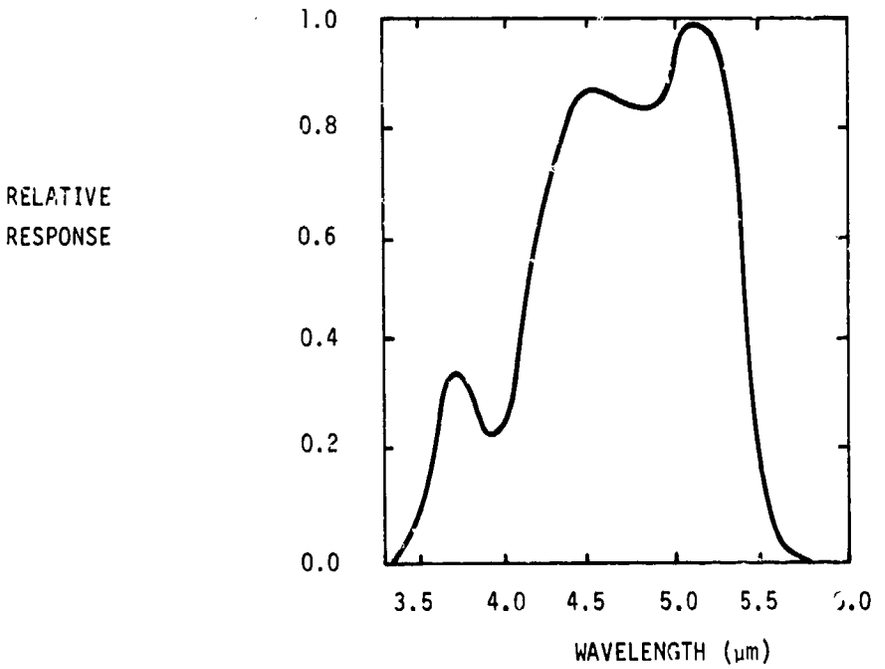

Figure 4-19. Spectral Response of Backside Illuminated HgCdTe Photodiode on HgCdTe (x = 0.4) Substrate

Quantum Efficiency for n^+ - p-p^+ Photodiodes

Figure 4-20 shows a detailed cross section of a typical HgCdTe detector structure.

Three factors can degrade the diode quantum efficiency from the ideal 100 percent value:

a. Reflection losses at the air-detector interface. These will be overcome by antireflection coating and are not discussed further.

b. Absorption of photons in the p^+ layer and subsequent loss due to recombination before the photon reaches the n^+-p junction.

c. Absorption of photons in the p layer and subsequent recombination as in b above.

The standard treatment of c assumes diode thickness much less than diode length or width and suggests a quantum efficiency η given as

$$\eta = (\cosh \frac{d}{L_e})^{-1} \qquad (4\text{-}1)$$

where d = detector thickness and L_e = minority carrier diffusion length. Building in the p^+ layer, and under the same assumptions as those used to derive Equation (4-1), the following more general expression is obtained for the quantum efficiency for radiation incident on the p^+ face of the photodiode:

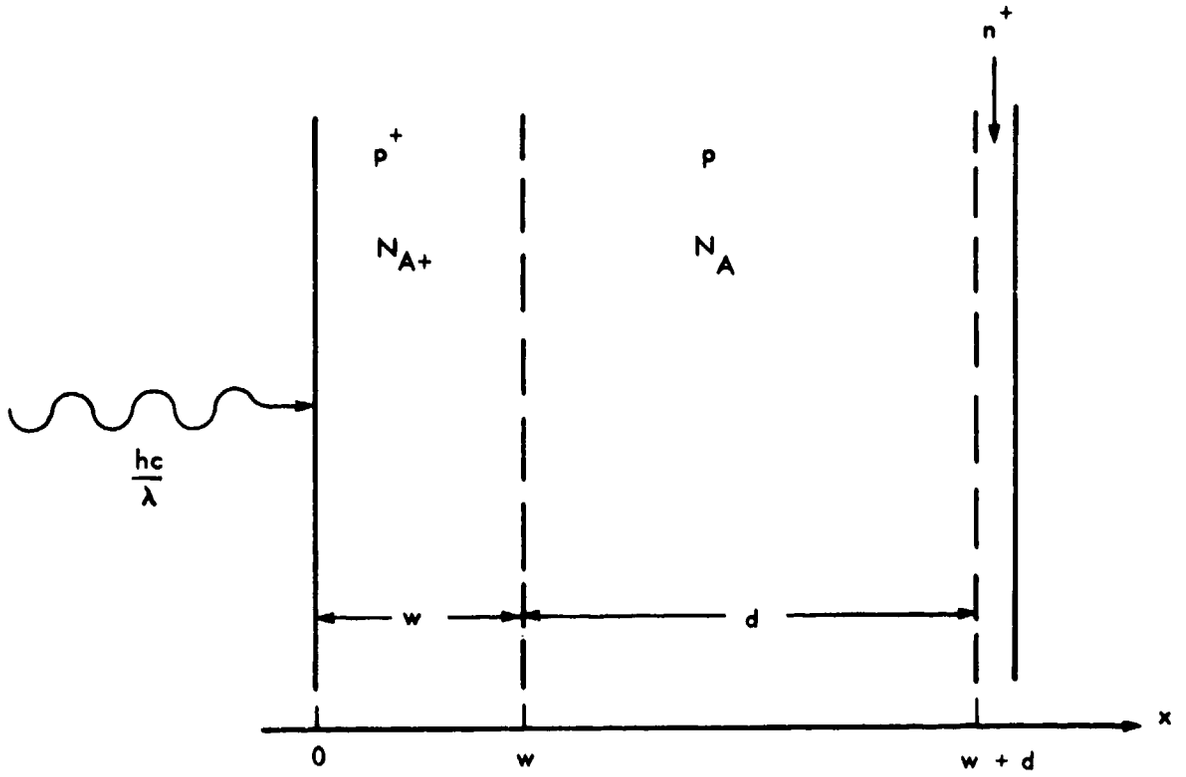

Figure 4-20. Cross Section of Detector Array

$$\eta = \frac{1}{\cosh\left(\frac{d}{L_e}\right) \cos h\left(\frac{w}{L_{e+}}\right)} \left[\frac{1}{1 + H_\infty \tanh\left(\frac{d}{L_e}\right) \tanh\left(\frac{w}{L_{e+}}\right)}\right] \quad (4\text{-}2)$$

$$\text{where } H_\infty = \frac{N_A}{N_{A+}} \left[\frac{\tau_e N_{e+}}{\tau_{e+} N_e}\right]^{1/2}$$

So that the p^+-region will not reduce the overall quantum efficiency, Equation (4-2) says that we must have $w << L_{e+}$ and, again assuming a thin p-region ($d << L_e$), that we must have

$$\frac{N_A}{N_{A+}} \left[\frac{\tau_e}{\tau_{e+}} \frac{\mu_{e+}}{\mu_e}\right]^{1/2} \frac{w}{L_{e+}} \frac{d}{L_e} << 1$$

If, therefore, H_∞ is small, and if w is much less than L_{e+}, Equation (4-2) reduces to Equation (4-1), the conventional expression for photodiode quantum efficiency. The derivation of Equation (4-2) is based on the approximation that all the radiation absorbed in the p^+ layer is absorbed near the outer face of the layer; thus, we have neglected surface recombination.

These considerations notwithstanding, it is incorrect to consider the photodiode width and length to be much greater than diode thickness. Lateral diffusion effects will play a greater role in determining the quantum efficiency than either Equation (4-1) or (4-2) would suggest. Indeed, from Equation (4-1), and with d = 10μm and L_e = 20μm, we derive η = 0.9. The more careful lateral analysis suggests $\eta \cong 0.6$. That analysis is presented in the next section, which treats the implications of lateral diffusion on both quantum efficiency and cross talk.

Figure 4-21 shows a typical plot of the measured quantum efficiency of HgCdTe detectors (λ = 4.2μm) as a function of the detector thickness. It can be seen that a maximum is observed with a thickness of 5 to 8μm and gradually decreases with increasing thickness.

Cross Talk Calculations for Backside Illuminated Arrays

Lateral diffusion of carrier pairs generated at the front surface of the p-type base region will give rise to some loss in quantum efficiency for individual elements and, more important, to interelement cross talk.

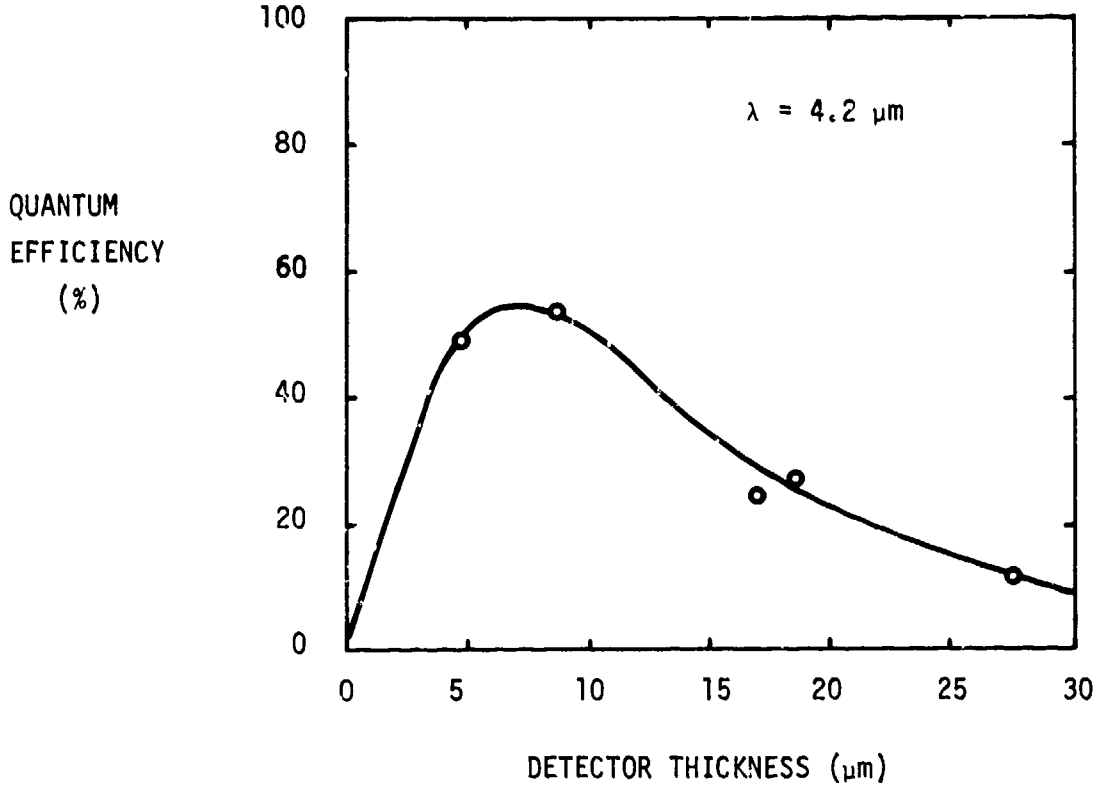

Figure 4-21. Measured Quantum Efficiency vs. Detector Thickness at T = 193 K for PV HgCdTe (λ = 4.2 μm)

Figure 4-22 illustrates qualitatively the spot scan profiles of an individual element of the mosaic for the ideal case of no lateral diffusion and for the realistic case with lateral diffusion.

By symmetry, the 50 percent contours will be straight lines at a distance L apart, where L x L is the cell size. In this case one can see that the optical area and the diffusion area will be about equal:

$$A_{op} \approx A_{diff} \approx L \times L$$

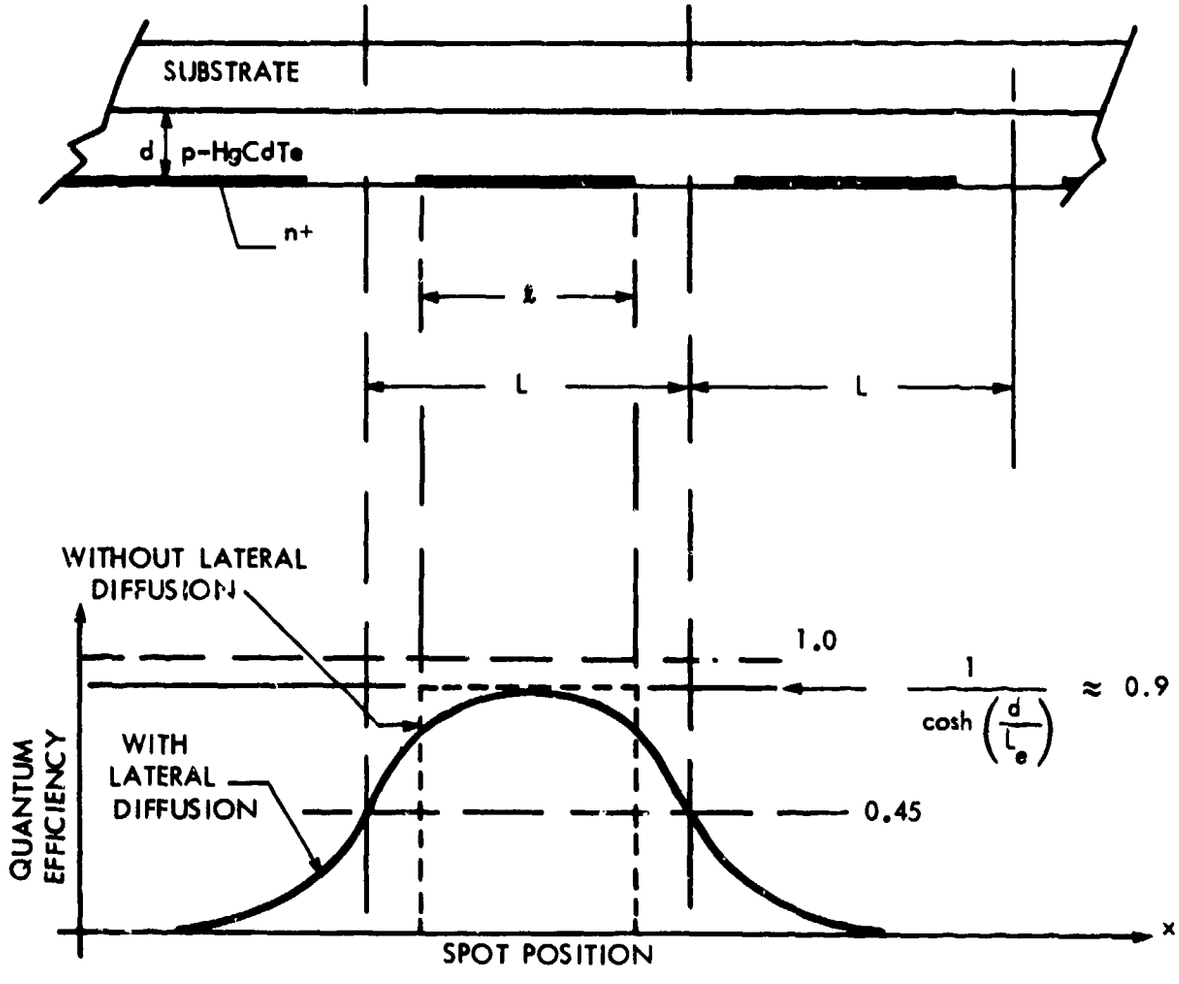

Figure 4-22. Response of One Detector Element of a Backside-Illuminated Array to a Spot of Incident Radiation as a Function of Spot Position

Numerical solutions have been obtained for the cross talk and quantum efficiency of backside-illuminated HgCdTe detector arrays using a thermal conduction computer program. The results indicate that for nominal 1.5 mil square detectors the detector thickness must be under 0.5 mil to limit the cross talk to less than 10 percent. Both crosstalk and quantum efficiency depend strongly on detector thickness, so careful fabrication control on thickness will be necessary to make large backside-illuminated detector arrays.

Description of Cross Talk Analysis--The calculations are based on the detector configuration shown in Figure 4-23. The detector junction areas are assumed to be completely contiguous in a square matrix. One detector is uniformly illuminated while the rest are dark.

The quantum efficiency and cross talk calculations are based on a general solution of the minority carrier flow problem in the detector. The carrier flow is described by two equations: the continuity equation, and the equation of motion. The steady state continuity equation is

$$\vec{\nabla} \cdot \vec{nv} = G - \frac{n}{\tau} \qquad (4\text{-}3)$$

where the term of the left-hand side describes flow of carriers out of a unit volume, and the terms on the right-hand side represent carrier generation due to optical absorption and carrier loss due to recombination within the unit volume. The total excited minority carrier number is given by $N = \int G \, dVol.$* The equation of motion reduces to

*G is limited to excitation in one detector volume.

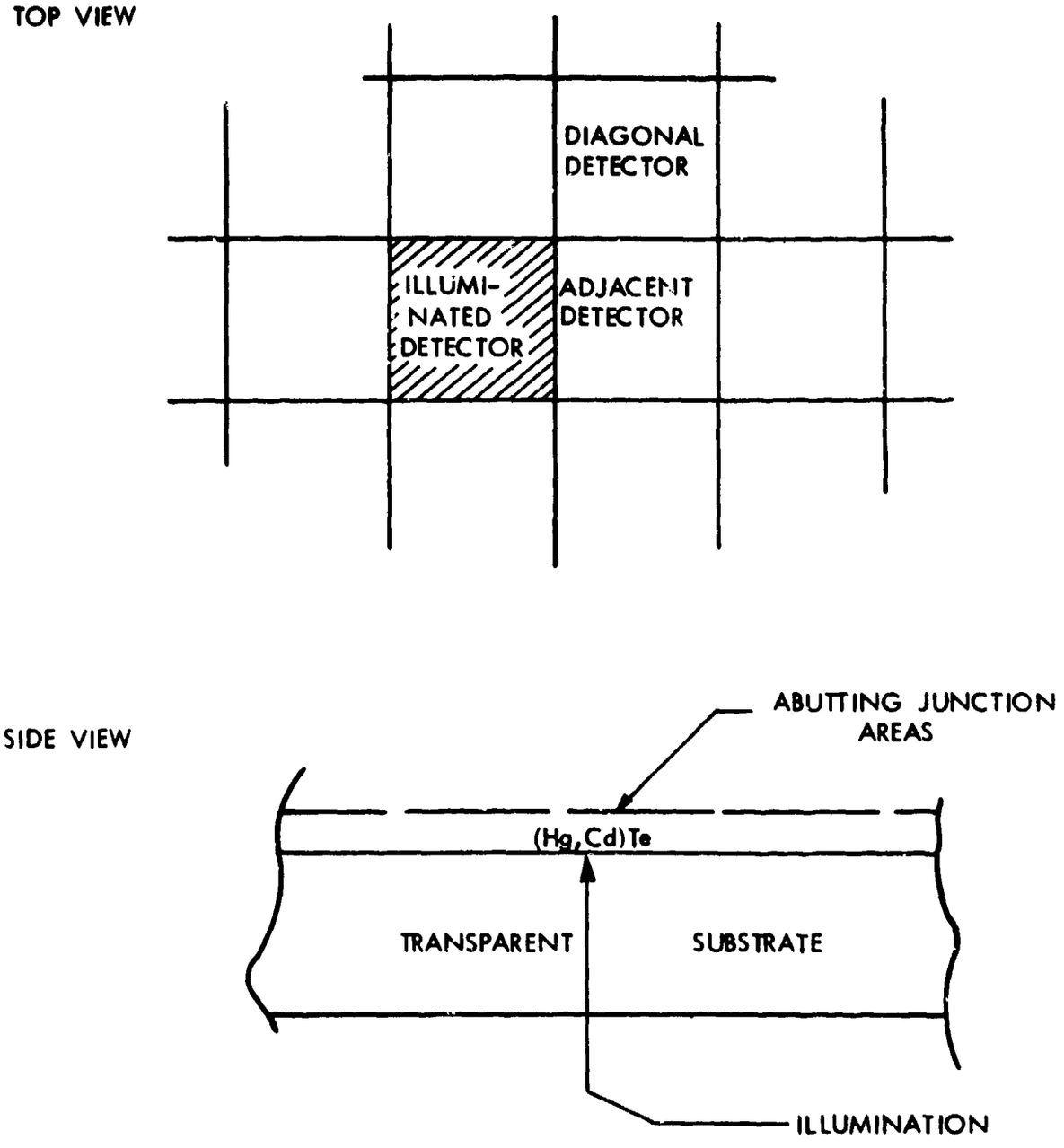

Figure 4-23. Detector Configuration Used in Cross Talk Analysis

$$\vec{nV} = -D\vec{\nabla} n \tag{4-4}$$

when the minority carrier density n is much less than the majority carrier density. The term nV is the carrier flow anywhere within the detector. Combining Equations (4-3) and (4-4) we obtain the general differential equation which must be solved:

$$L^2 \nabla^2 n + \tau G - n = 0 \tag{4-5}$$

where

$$L^2 = D\tau$$

Once n(x, y, z) has been determined, the current flow to the junction is given by an integration of the current density over the junction area:

$$1 = \int_{A_j} \vec{J} \cdot \vec{dA} = \int_{A_j} nq\vec{V} \cdot \vec{dA} \tag{4-6}$$

The solution of Equation (4-5) depends critically on the boundary conditions at the edges of the detector array. For the backside-illuminated structures considered here, most of the photon absorption takes place in the thick p layer. An accurate approximation to the actual diode structure is that the diode n^+-layer is assumed to have negligible thickness. Any carrier which reaches the edge of the junction depletion region is rapidly swept across the junction to the n-side by the built-in junction electric field. The boundary condition on the minority carrier density is n(junction) = 0. The

boundary condition over the remainder of the detector periphery depends on the nature of the surface passivation. A phenomenological term which describes the "quality" of the surface passivation is the surface recombination velocity S, which describes the loss of minority carriers due to recombination at the surface. The boundary condition at a passivated surface is given in terms of the surface recombination velocity by

$$n(\text{surface})\, S = D \vec{\nabla} n \cdot \hat{\varepsilon}_n \Big|_{\text{surface}} \tag{4-7}$$

where $\hat{\varepsilon}_n$ is the normal to the surface.

A complete analysis has shown that the critical parameter for the surface boundary condition is the dimensionless ratio $S/L/\tau$ when $S/L/\tau$ is much less than one, the boundary condition reduces to $\vec{\nabla} n \cdot \hat{\varepsilon}_n \Big|_{\text{surface}} = 0$. The factor L/τ is a characteristic "diffusion velocity" which for 3 to 5μm HgCdTe at 195 K is approximately 10^4 cm/s. Measurements on passivated HgCdTe surfaces have shown that S is typically below 100 cm/s, so $S/L/\tau \sim 0.01$.

The differential equation, boundary conditions, and solution for current collection efficiency are summarized in Table 4-7.

The quantum efficiency is calculated by letting $\vec{dA}$ range over the junction of the detector which is illuminated, while the cross talk to another detector is calculated by letting $\vec{dA}_j$ to range over some unilluminated junction.

TABLE 4-7. CURRENT COLLECTION EFFICIENCY SUMMARY

Differential Equation $L^2 \nabla^2 n(x,y,z) + \tau G(x,y,z) - n(x,y,z) = 0$	
Boundary Conditions:	
At a passivated surface	$\vec{\nabla} n \cdot \hat{\varepsilon}_n \Big\vert_{\text{surface}} = 0$
At a junction	$n = 0$
Quantum efficiency	$n = \dfrac{\int qD \vec{\nabla} n \ \vec{dA}}{\int G \, dVol}$

Because of the mixed nature of the boundary conditions (n specified over part of the surface, n specified over the remainder of the surface), an analytical solution to Equation (4-5) for physically interesting geometrical configurations is difficult to obtain. Fortunately, because of the similarity of the minority carrier flow problem to the heat flow problem, numerical computation techniques originally derived for thermal conductivity may be readily used for cross talk calculations.

The equation describing heat flow in a homogeneous solid is

$$\frac{k}{pc} \nabla^2 T \dot{Q} = 0 \qquad (4\text{-}8)$$

This equation is solved using a thermal conduction computer program which uses a finite difference algorithm. T is identified with n, and $\dot{Q}$ is identified with (τG - n). The detector array is divided into a set of nodes, and the computer derives a self consistent solution for the heat (carrier) input to and output from each node. Then the heat (carrier) flow to the surface is summed over each detector junction area to give the quantum efficiency and cross talk.

The results of the analysis are shown in Figures 4-24 and 4-25. Figure 4-24 shows that, for a fixed base thickness of 12.5μm, a 0.002 in. x 0.002 in. cell size, and a minority-carrier diffusion length L_e of about 20μm, an interelement cross talk of about 7 percent for adjacent elements (about 1 percent for diagonal elements) and a quantum efficiency of about 60 percent can be expected. The goal for the base thickness is 10μm, so that (judging from the trends of Figure 4-25) one might expect cross-talk for adjacent elements to be more like 5 percent and quantum efficiency to be more like 65 percent.

The numerical results are summarized in Table 4-8. For these results the optical absorption coefficient was taken to be 3000 cm^{-1}.

The large value of adjacent element cross talk which these calculations indicate is primarily due to lateral diffusion of optically generated electron-hole pairs from one unit cell of the mosaic to the next. This can be reduced, of course, by reducing the minority-carrier diffusion length L_e, but what we want to have is material with τ_e, and hence L_e, as long as possible to obtain maximum R_oA.

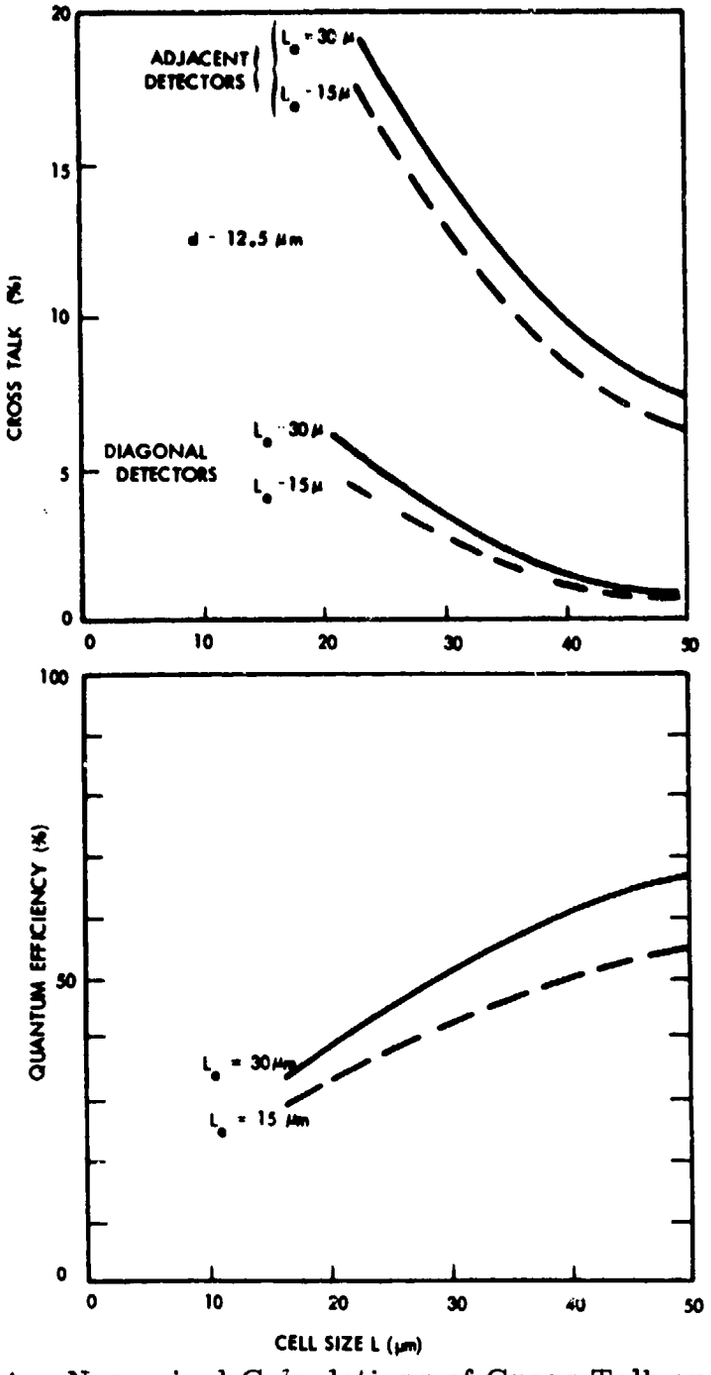

Figure 4-24. Numerical Calculations of Cross Talk and Quantum Efficiency vs. Mosaic Cell Size L, for a Fixed p-Type, Base Thickness d = 12.5 μm, and for Two Values of Electron Diffusion Length

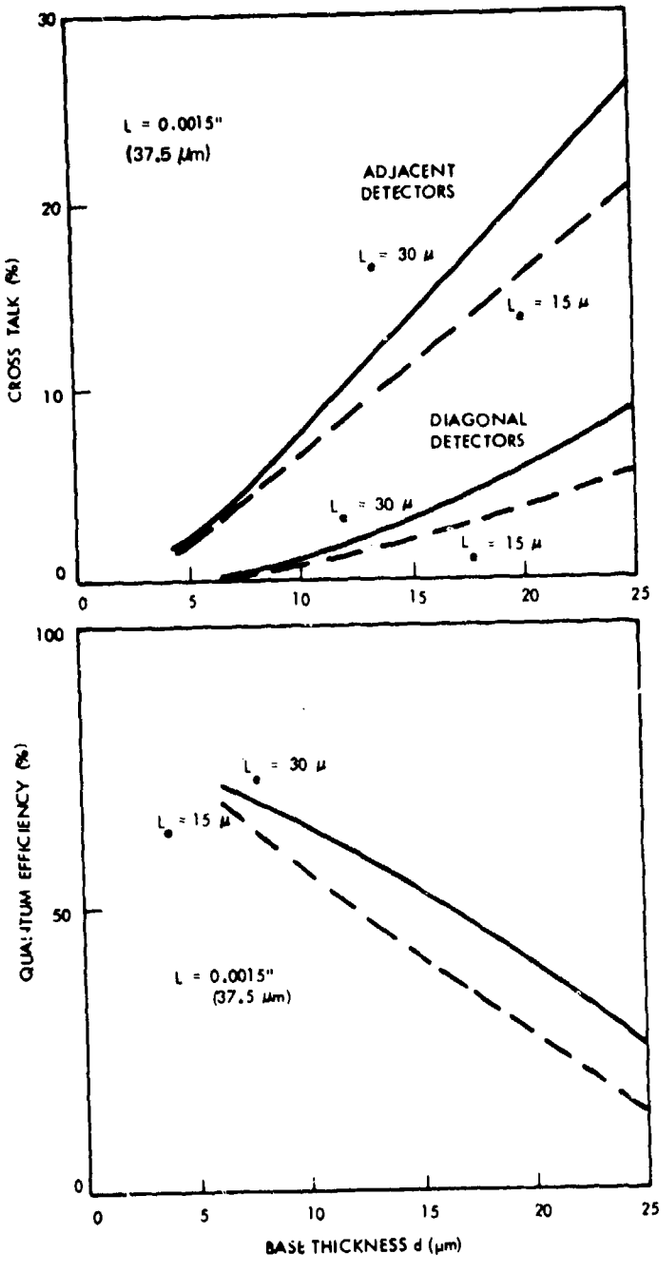

Figure 4-25. Numerical Calculations of Cross Talk and Quantum Efficiency vs. Base Thickness d, for a Fixed Cell Size L = 0.0015 in., and for Two Values of Electron Diffusion Length

TABLE 4-8. NUMERICAL CROSS TALK CALCULATION RESULTS

Detector ℓ (μm)	Thickness d (μm)	Diffusion Length L_e (μm)	Cross-Talk (%)		Quantum Efficiency (%)
			Adjacent	Diagonal	
37.5	12.5	15	9.3	1.4	48.6
37.5	12.5	30	10.7	1.8	58.4
37.5	6.25	15	3.3	0.2	68.0
37.5	6.25	30	3.5	0.2	71.8
37.5	25.0	15	20.8	5.5	14.6
37.5	25.0	30	26.3	9.0	25.7
25.0	12.5	15	16.0	3.8	37.8
25.0	12.5	30	17.9	4.7	44.8
50.0	12.5	30	7.1	0.7	54.4
50.0	12.5	30	7.1	0.7	66.8

One method of reducing the cross talk is to further reduce the base thickness d. Cross-talk varies almost linearly with base thickness (see Figure 4-25) and R_oA varies inversely with d so that reducing the base thickness simultaneously reduces cross talk and increases R_oA.

FOCAL PLANE READOUT ELECTRONICS

Input Coupling Analysis

Several input coupling circuits were analyzed for use in the staring focal plane application. All circuits fall into two broad classifications: source coupling techniques and gate coupling techniques.

The basic problem in dealing with the small input cells is that extensive background suppression is required due to the limited charge-handling capability of the small cells. This analysis concludes that source coupling, while reducing the input 1/f noise effects considerably, requires quite complex dc supression techniques, thus pressing the fabrication technology if these circuits are to be fabricated in small unit cell sizes.

Most gate-coupled input circuits suffer from input gate 1/f noise problems at these low frequencies and therefore tend to need high input stage gain requirements to get above the 1/f noise. In addition, high reset noise levels are found on several of the circuits analyzed when the circuits are reduced to very small (1 x 1 and 2 x 2 mil) cell sizes. Honeywell's Multiple Sample Injection (MSI) input is shown to operate in a unique manner such that high performance levels can be obtained using this simple, low component count input technique.

Source Coupling--The frame rate possible with source-coupled inputs is limited to about 1000 frames per second due to the limited background suppression factors that are achievable with present and near future state-of-the-art threshold uniformities. The use of zero-bias source-coupled detectors requires a preamp stage if detector-limited performance

is to be achieved, but this demands considerable area which is not available with small cell sizes, such as 2 x 2 mil or 1 x 1 mil.

Figure 4-26 shows the frame rate possible as a function of the cell size for a background suppression level of S = 1 and S = 10. The large cells have a larger fraction of real estate available for charge storage than do the smaller cells and therefore lower frame rates are possible. Even with a 4 x 4 mil cell and a background suppression factor of S = 10, we can still only achieve a 500 fps frame rate for the RA = 40Ω - cm^2 detector with f/1 optics.

If other approaches were not available, source coupling could be used by multiple readout and storage in registers off the focal plane. Although clearly possible, this method has significant disadvantages:

- Increased system complexity, power dissipation, and size requirements
- Excessive output data rates required for the large focal planes of future systems

An example of the high speed data rates required for large focal planes is seen by considering a 512 x 375 array with the desired frame rate of 30 fps. The output data rate required if the focal plane is read out at 10 times this rate and the information stored off the focal plane is f_c = 57.6 MHz, well beyond present state-of-the-art. Reduction of this data rate would involve further system complexity in requiring storage in multiple registers and would entail further readout processing.

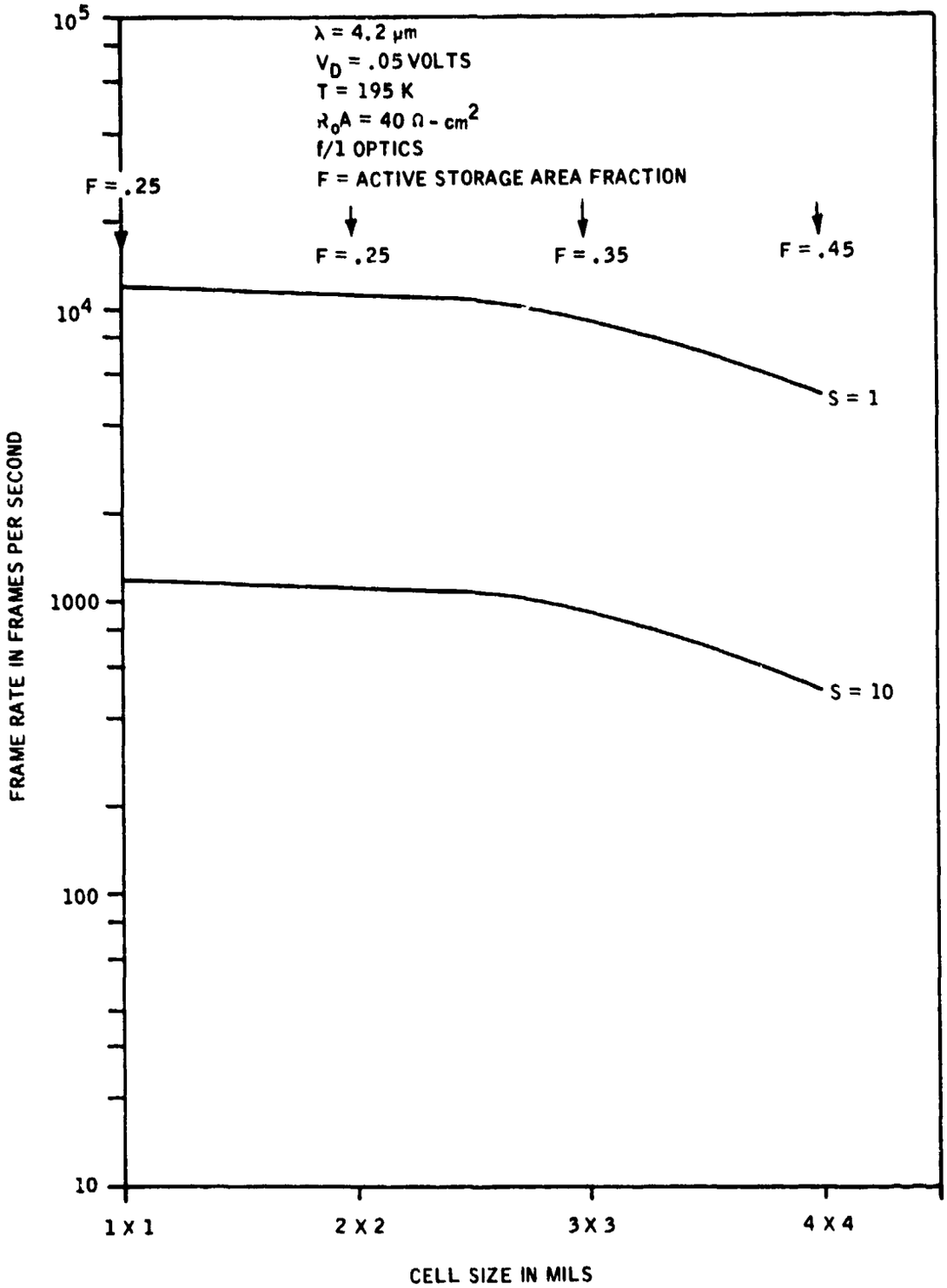

Figure 4-26. Source-Coupled Input Frame Rate vs. Cell Size for Different dc Suppression Factors, S

Gate Coupling Inputs--Three prime candidate input circuits were analyzed for performance in a 2 x 2 mil and 1 x 1 mil configuration. These circuits are

- Multiple Sample Injection (MSI) Input
- Direct gate coupled
- Modified MOSFET Gain Input
- Subthreshold MOSFET Amplifier Input
- Bipolar preamp input

Table 4-9 shows a summary of the five different gate coupled input circuits which were characterized. The conclusion reached from the analysis are the following:

1. The MSI input combines the features of simple, low component count configuration which permits fabrication of CCD cell sizes to 1 x 1 mil and less while maintaining a near-unity input noise figure.

2. The direct gate coupled input requires relatively large input currents in order to achieve a low input noise figure. Alternatively this input can be operated at low frame rates but with a high input noise figure.

3. The reset noise on the Modified MOSFET and Subthreshold Amplifier inputs limits the input noise figure to the mid-teens for small cell sizes. Again, however, a low input noise figure can be achieved if a large cell size can be utilized.

TABLE 4-9. PERFORMANCE AND LAYOUT CHARACTERISTICS OF VARIOUS V GATE COUPLED INPUT CIRCUITS

	MSI Input	Direct Gate Coupled	Modified MOSFET GAIN	Subthreshold MOSFET Amplifier INPUT	Bipolar Preamp
Minimum Cell Size	≤ 1 x 1 mil	≤1 x 1 mil	> 3 x 4 mil	3 x 4 mil	4 x 4 mil
Minimum Frame Rate	30 fps	60 fps	60 fps	60 fps	30 fps
Input Noise Figure	≈ 1.0	≈ 10.0	≈1 (3 x 4 mil cell) ≈ 14**	≈ 1 (3 x 4 mil cell) ≈ 15*	≈ 1.0

* Calculated by assuming that it could be fabricated in a 1 x 1 mil cell

MSI Input--The MSI input analysis is described in Appendix A. The following subsections summarize the performance calculations made for the other gate-coupled circuits.

Direct Gate-Coupled Input--One approach to coupling the photovoltaic detector to the CCD is by directly connecting the detector to the input MOSFET gate, as shown in Figure 4-27a. The advantage of this approach is that the detector is floating, so the detector background current does not flow into the storage well under ϕ_W. However, there is a condition on the input gate current: it must be sufficiently high to keep the noise of the input MOSFET below that of the detector. The input noise figure as a function of input current is calculated below, with reference to the noise equivalent circuit of Figure 4-27b. The input noise figure referred to an open circuited detector without CCD readout is

$$NF = \left[1 + \frac{I_B + 2I_S}{I_O} \right]^{1/2} \qquad (4\text{-}9)$$

where I_B = background generated current
I_S = detector saturation current
I_O = CCD input current

This result is plotted in Figure 4-28 for a 2 x 2 mil detector at T = 190 K.

It can be seen that relatively large input currents are required to achieve a low input noise figure. These higher input currents are incompatible with the CCD receiving well capacity as indicated in the figure. The receiving well (assuming $A_{Rw} = 0.25\ A_D$) current for a 60 frame per second input is about 6×10^{-11} amps maximum.

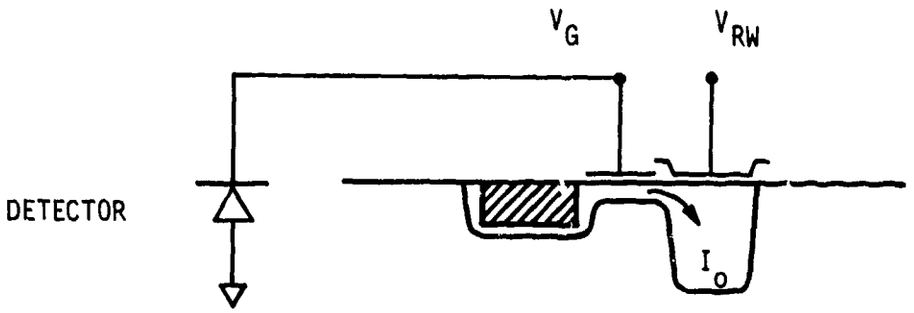

Figure 4-27a. Direct Gate-Coupled Circuit

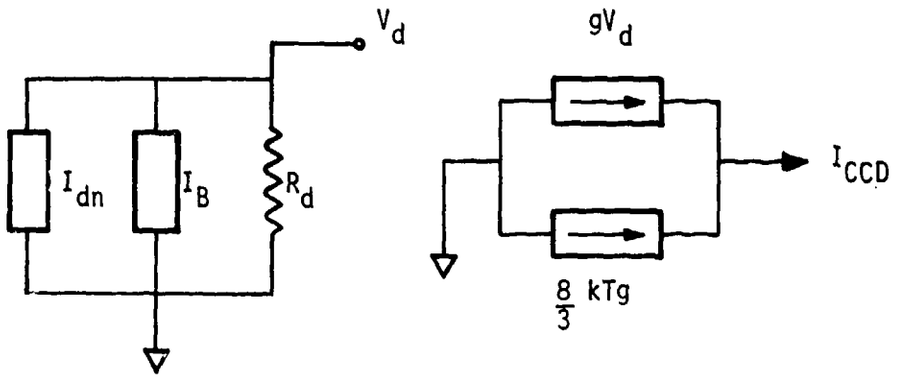

Figure 4-27b. Gate-Coupled Noise Equivalent Circuit

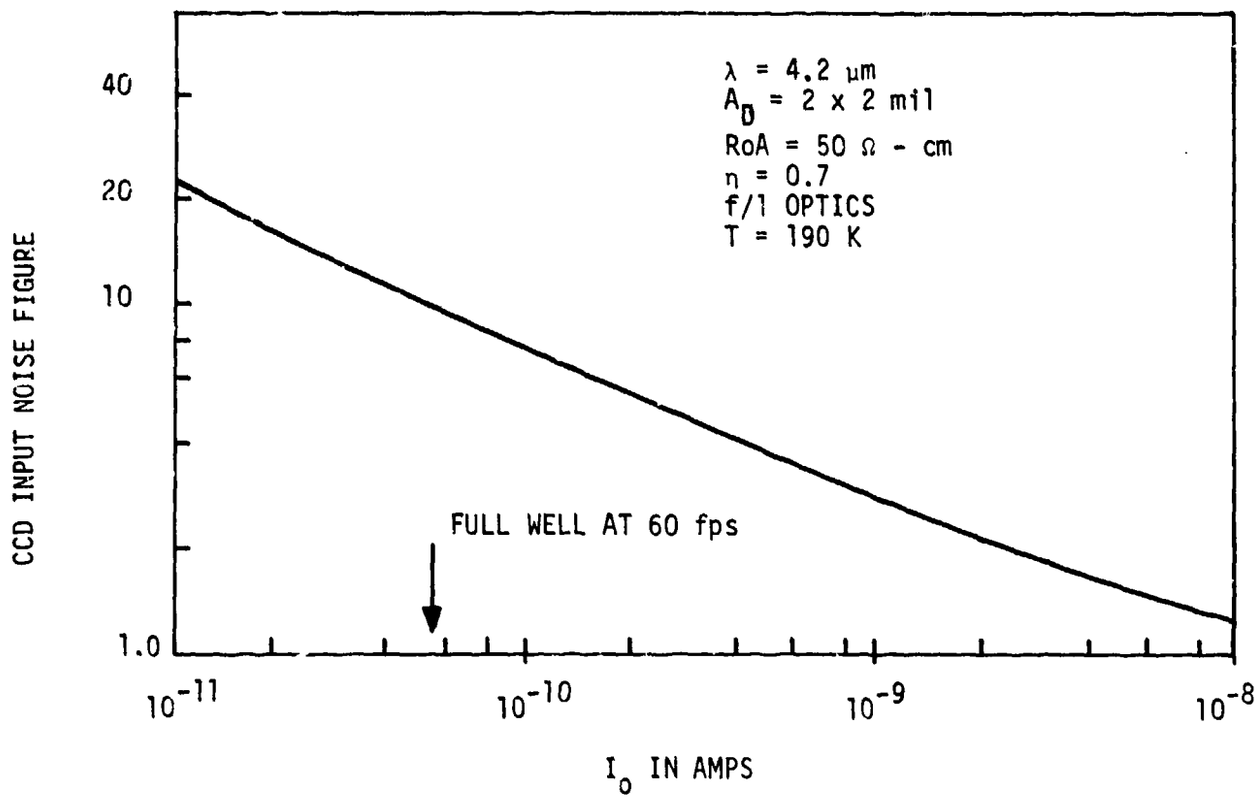

Figure 4-28. Noise Figure for Direct Gate-Coupled Input as a Function of CCD Input Current

This current requirement for the gate-coupled input can be reduced by providing a detector signal voltage gain between the detector and CCD input gate. The input current level can then be reduced by a factor equal

to the square of the gain. The increase in integration time needed is about a factor of 100 so that an input stage gain of 10 should get to the desired 60 frame per second rate.

Modified MOSFET Gain Input--One drawback to the gate-coupled input described earlier is the large amount of current which must flow into the CCD storage well to make the noise of the input MOSFET lower than the detector noise. Because of the limited storage well area, this large current results in a very short frame time. This current can be significantly reduced if some gain is introduced between the detector and the input gate.

Figure 4-29 shows a diagram of this gate-coupled input circuit. In this case, the MOSFET (Q1) provides the necessary current-to-voltage conversion which is then ac coupled onto the first input gate (V_g) of the CCD. The voltage-to-current conversion is thus accomplished through the modulation of the CCD input current. Since the CCD receiving well (V_{RW}) is of necessity small, the input gate must be operated in the subthreshold region with the injected charge integrated under V_{RW}. Notice that the injected charge is related exponentially to the ac component of the diode current (this is generally assumed small enough to linearize the relationship).

The noise analysis of this circuit is relatively straightforward. The detector/input noise figure, defined relative to the noise of the detector alone at zero bias, is given by

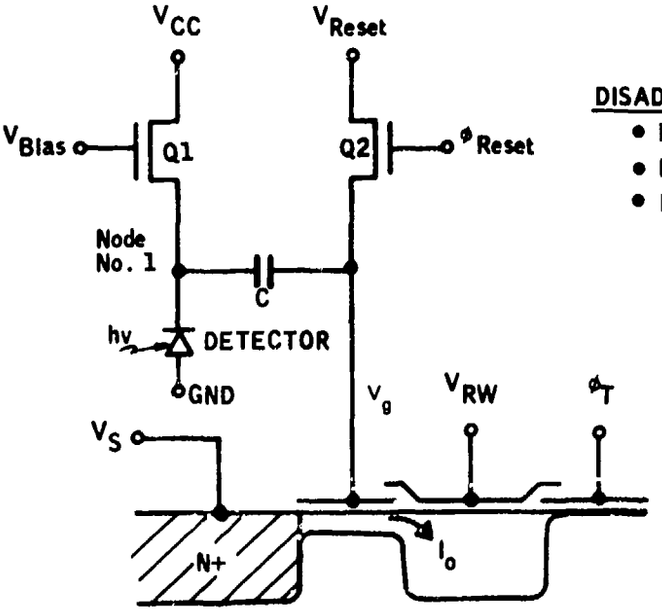

DISADVANTAGES

- HIGH COMPONENT COUNT
- HIGH RESET NOISE
- HIGH INPUT NOISE FIGURE

INPUT CIRCUIT DIAGRAM

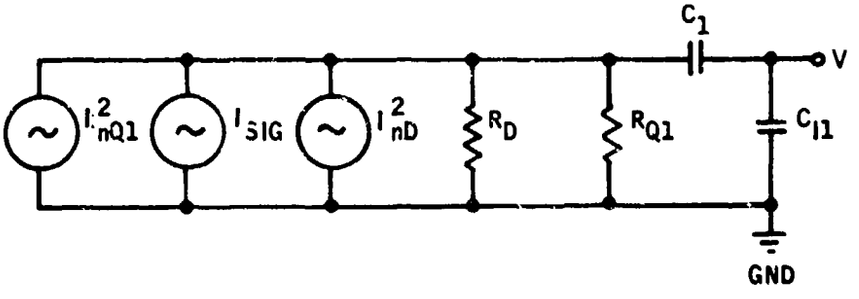

SMALL SIGNAL A.C. MODEL

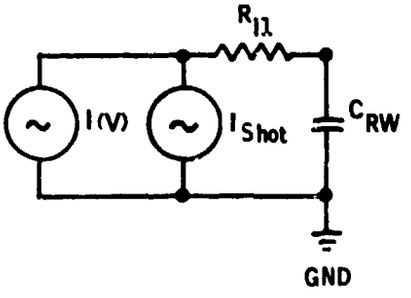

Figure 4-29. Modified MOSFET Gain Input Structure

$$NF = \left[\frac{1 + \left(\frac{KT}{q}\right)^2 \left(1 + \frac{(g_1 + g_2) R_D}{R_D}\right)^2 \frac{1}{I_o} + \frac{4}{3}\frac{kT}{q} g_1 + I_s\left(1 - \exp - \frac{qV_R}{kT}\right)}{I_B + 2I_s} \right] \tag{4-10}$$

where

$$g_1 = \frac{Z\mu}{L} C_{ox} \frac{kT}{q} \left[\left(1 + \frac{2I}{\frac{Z\mu C_{ox}}{L}} \left(\frac{q}{kT}\right)^2 \right)^{1/2} - 1 \right] \quad (= \text{Bias MOSFET transconductance})$$

$$I_1 = I_B + I_S \left(1 - \exp \frac{-qV_R}{kT} \right)$$

$$g_2 = \frac{qI_o}{kT} \quad (= \text{CCD input transconductance in subthreshold region})$$

I_o = CCD input well current

I_s = detector saturation current

In this expression, 1/f noise of both the detector and the CCD inputs have been neglected. They are readily included, but for a first-order tradeoff on CCD input current and detector parameters, the results are more transparent without the 1/f noise.

Figure 4-30 gives plots of the noise figure (NF) vs. the detector reverse bias for input currents, I_o, of 0.03, 0.1, and 1.0 na. Notice that, to

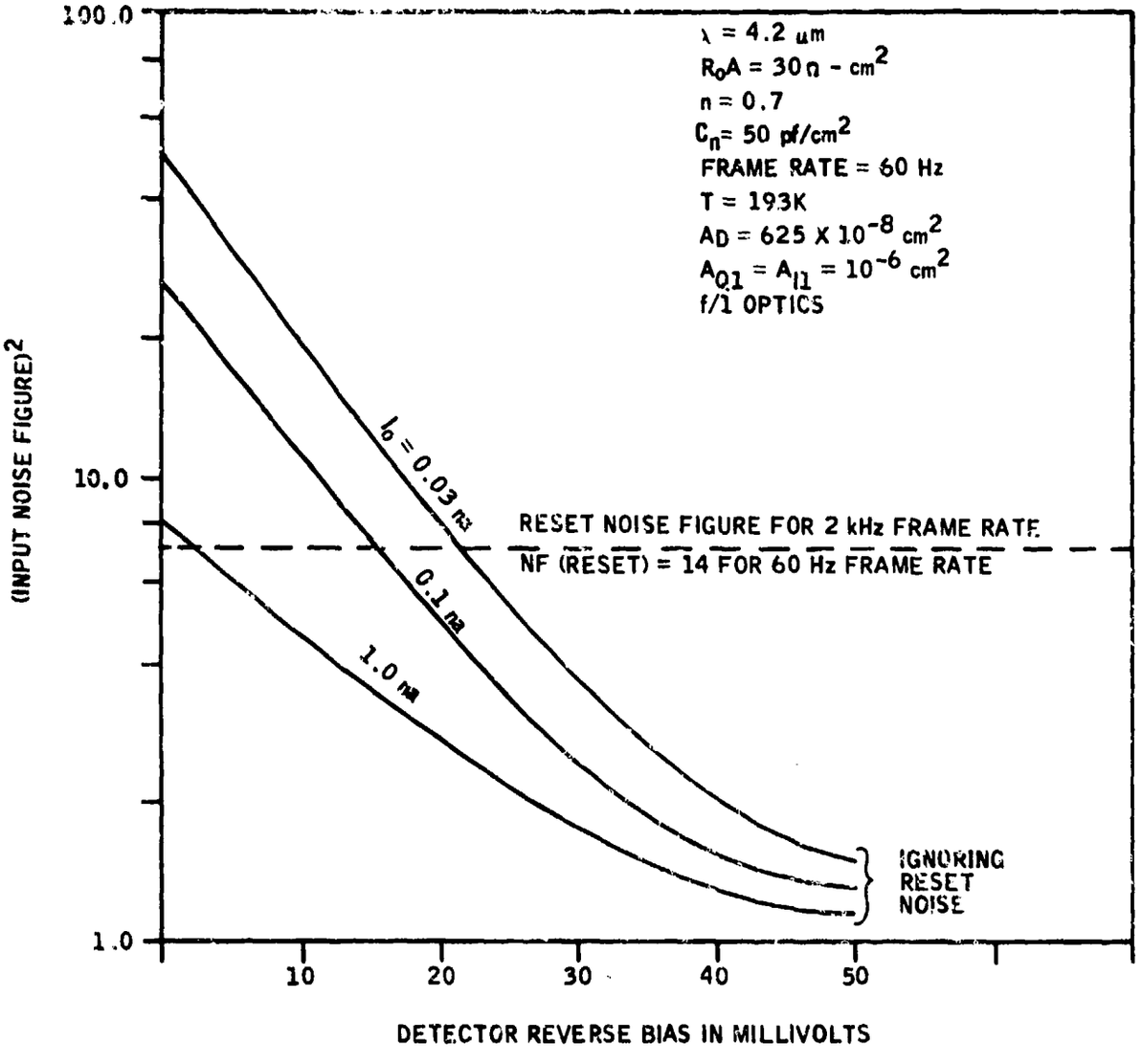

Figure 4-30. Noise Figure vs. Reverse Bias for the Modified MOSFET Input for 4.2 μm Detector

achieve values near unity, it is necessary to reverse bias the detectors to ~40 mV and use input currents of ~1.0 na. This result thus indicates that, although NF values near unity may be obtained by this technique, a 1 mil cell must operate at a frame rate of ~2 kHz to accommodate the integrated input current assuming no additional current suppression functions can be incorporated into the cell. Thus, although this cell can achieve NF values near unity, any advantages obtained by this feature are negated by the high frame rate requirement. (Alternatively, should the input be operated at sufficiently low I_o values to produce low frame rates, the NF value would be very high at attainable reverse biases.)

In addition to the above mentioned frequency limitations, the cell's noise figure performance changes radically when consideration is given to the reset noise of the dc biasing network. (This source of noise is normally neglected in the treatment of preamplifiers and is factored into the curves of Figure 4-30.) For large cell sizes, this source of noise can readily be minimized by enlarging the coupling capacitors. For smaller cell sizes, this is not generally possible, which leads to a dominance of the noise by this term. In general, the noise figure due to the reset only is

$$NF_{Reset} = \left[1 + \frac{kT/C}{2qI_o R_{D1}^2 \Delta f + 4kT\, R_D\, \Delta f} \right] \qquad (4\text{-}11)$$

where

$$R_{D1} \equiv \frac{R_D R_{Q1}}{R_D + R_{Q1}}$$

I_o ≡ total detector current

$C \equiv$ total reset capacitance

$\Delta f \equiv$ noise bandwidth

For a 1 x 1 mil cell size, typical values are $C \cong 10^{-12}$ and $I \approx 7 \times 10^{-9}$ amps, thus yielding

$$NF_{Reset} \approx \begin{cases} 14 \text{ for a 60 Hz frame rate} \\ 2.6 \text{ for a 2 kHz frame rate} \end{cases}$$

Notice that, in either case, the input noise is dominated by reset noise which makes the noise figure essentially flat for reverse biases as shown in Figure 4-30. (An exception would be to modify the input circuit by eliminating the reset MOSFET. This would eliminate the reset noise but would introduce large responsivity dependent offset levels in the CCD.)

Subthreshold MOSFET Amplifier Input--In this technique (Figure 4-31), gain is provided at the V_g electrode by using positive feedback of the signal voltage at node 1 to modify the gate voltage of the pull-up device (node 2). The gain thus obtained is derivable by consideration of the feedback ratio in the subthreshold regime. Quantitatively the result is

$$\text{Gain} = \frac{C_{FB} + C_G + C_1}{C_G + C_1}$$

where

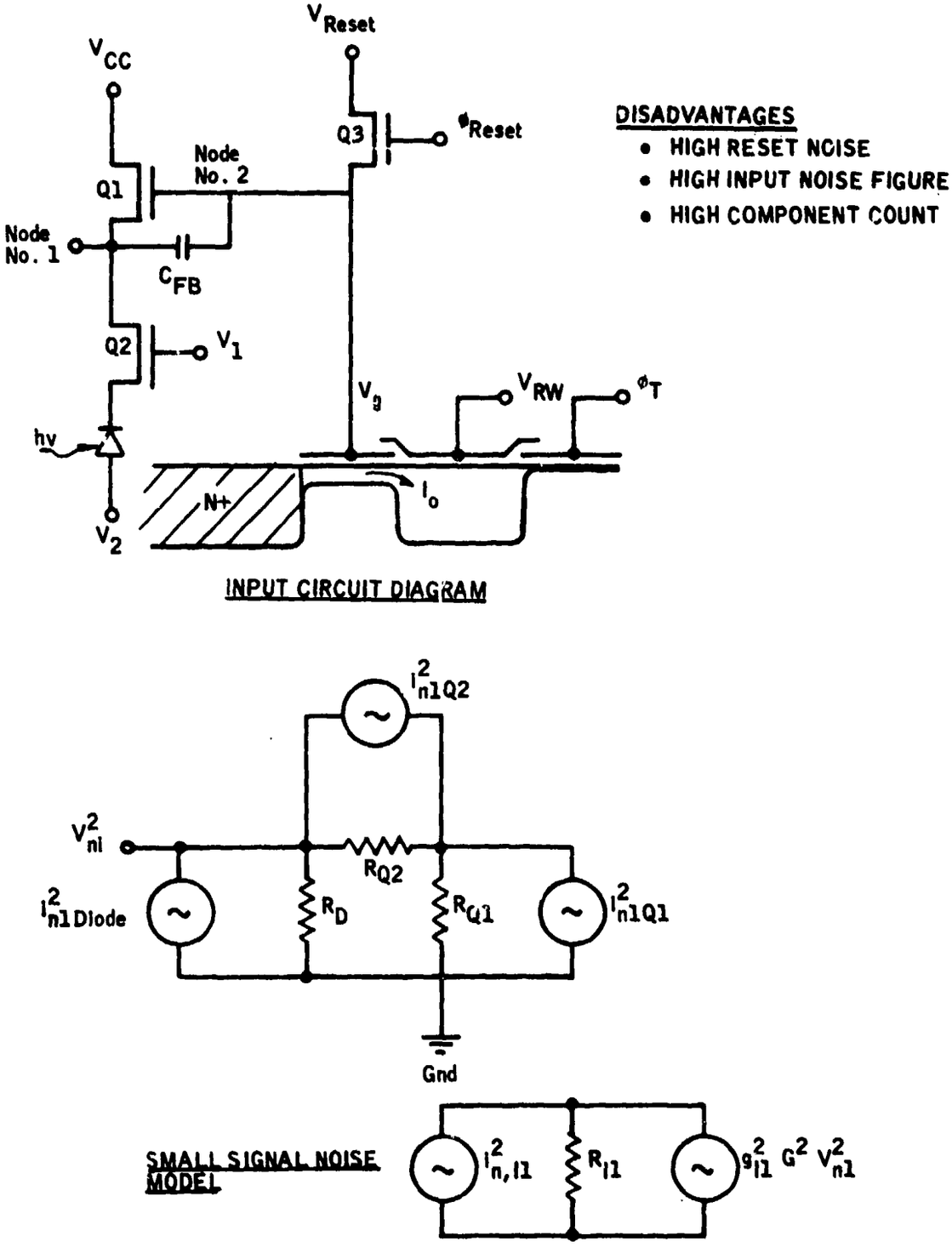

Figure 4-31. Subthreshold MOSFET Amplifier

C_G ≡ gate capacitance of Q1

C_{FB} ≡ feedback capacitance

and

C_1 ≡ the capacitance associated with the reset transistor and the CCD input gate

Notice that the circuit allows for adjustment of the quiescent voltage on V_g by periodic pulsing of the reset gate. Also of interest is the high component count (three transistors and one capacitor) necessary for proper implementation.

Figure 4-32 plots the NF vs. the detector reverse bias with I_o as a running parameter. Notice that, to attain noise figures near unity, it is necessary to run the detector at a reverse bias of approximately 40 mV with a CCD input current of ~0.4 nano amps. This results in frame rates considerably higher than the desired 30 frames per second (again assuming space does not permit further dc charge reductions).

A final point of interest in conjunction with this circuit is the influence of the reset noise on the gate. This noise source again limits the input noise figure to values at or near the mid-teens.

Bipolar Preamp Input--Figure 4-33 shows a bipolar preamp input circuit structure. The bipolar transistor can exhibit low noise characteristics while operating at relatively low power dissipated levels. Additionally,

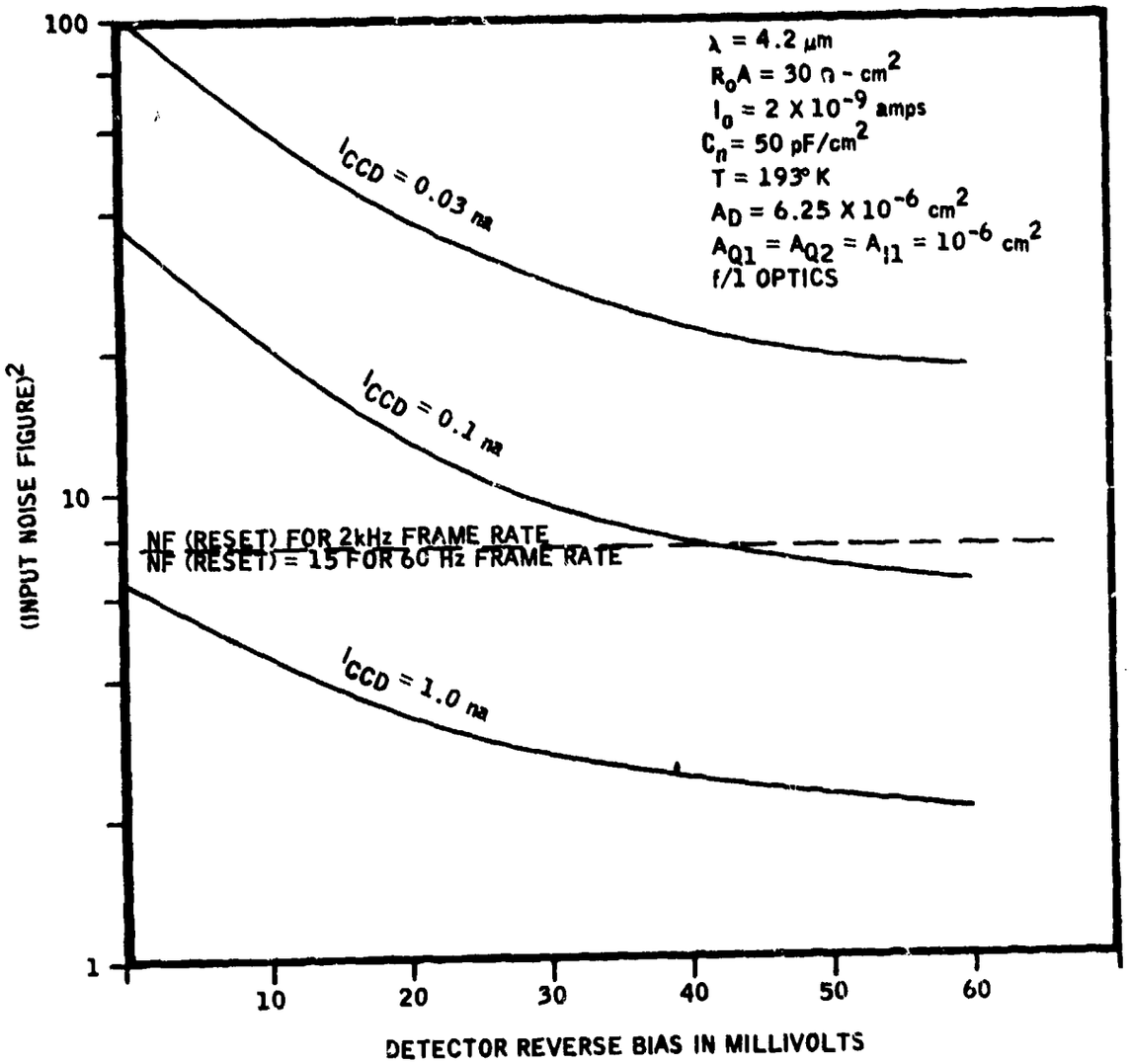

Figure 4-32. Noise Figure Sequenced vs. Detector Reverse Bias for the Subthreshold MOSFET Amplifier Input

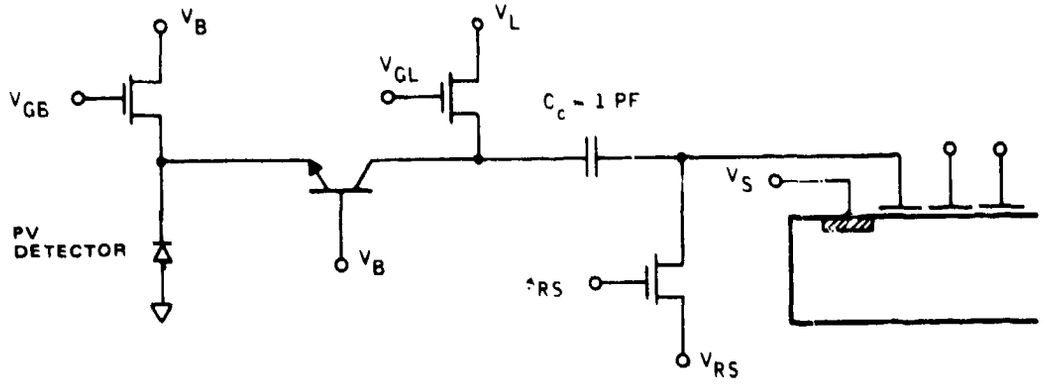

Figure 4-33. Gate-Coupled Bipolar Preamp Input

a favorable 1/f noise characteristic makes them attractive at pre-amplification stages.

This input circuit, however, has several drawbacks, one of which is the unit cell real estate requirements. This input circuit requires three MOSFET transistors as well as the bipolar transistor. In addition, the circuit of Figure 4-33 will exhibit a wide variation in the transistor gain values, unless a feedback resistor (or feedback MOSFET) is incorporated into the circuit for gain stabilization.

The area requirements of four MOSFET and one bipolar transistor, plus the CCD input structure and shift register, place a lower limit on the unit

cell size of about 5 x 5 mil or 4 x 4 mil for the smallest dimensions. This large unit cell limitation greatly limits the potential applications of this structure and therefore does not merit further consideration for this application.

1/f Noise Effects

The effect of 1/f noise components generated at the input gate of the CCD structure can strongly influence the focal plane performance depending upon the detector/CCD coupling circuit and the device processing parameters. Although the exact source of 1/f noise is not precisely known, it is felt that traps at the Si - SiO_2 interface which have a wide range of trapping time constants are responsible for these effects.

As described in contract report DAAK70-76-C-0250 the 1/f noise voltage at the input control gate of a CCD can be described by the following empirically derived equation:

$$V_n^2 = \frac{C_n KT}{C_{ox}^2 A_g f^n}$$

where

C_{ox} = oxide gate capacitance/area

A_g = input gate area

f = reassuring frequency

n = slope constant (typically $0.8 < n < 1.0$)

C_n = processing quality factor (in units of Farads/cm^2)

Figure 4-34 shows a plot of the input referred gate noise voltage V_n as a function of the quality factor, C_n for a direct gate coupled input circuit. Also shown is the detector noise voltage vs. detector size so that a relative comparison can be made between the 1/f noise voltage and the detector noise. It can be seen that to achieve a 1/f noise component at 30 Hz which is less than the detector noise for a 2 x 2 mil cell the C_n factor must be less than about 1 PF/cm^2 for an input gate area of 0.5 x 0.5 mil.

The 1/f noise factor for a source coupled input is attenuated from the numbers shown in Figure 4-34 due to the shunting effect from the input transconductance which attenuates the 1/f noise injected into the receiving well by a factor of $(1/1 + g_m R_D)$.

DETECTOR/CCD MECHANICAL INTERFACE

As mentioned in this section, the use of backside illuminated detectors which are flip-chip interconnected to the CCD readout electronics offer the advantage of high packing density structures and 100 percent detector fill factors over the evaporated lead approach. The flip-chip interconnect consists of forming a ductile material, in the shape of a bump or column, on the detector and CCD contact pads and mating them together either by cold weld, reflow, or ultrasonic bonding. This approach is shown schematically in Figure 4-35. The interconnect material must be ductile enough at low temperature to take up the stress applied through the different thermal expansion coefficients of the CCD readout electronics (silicon) and the

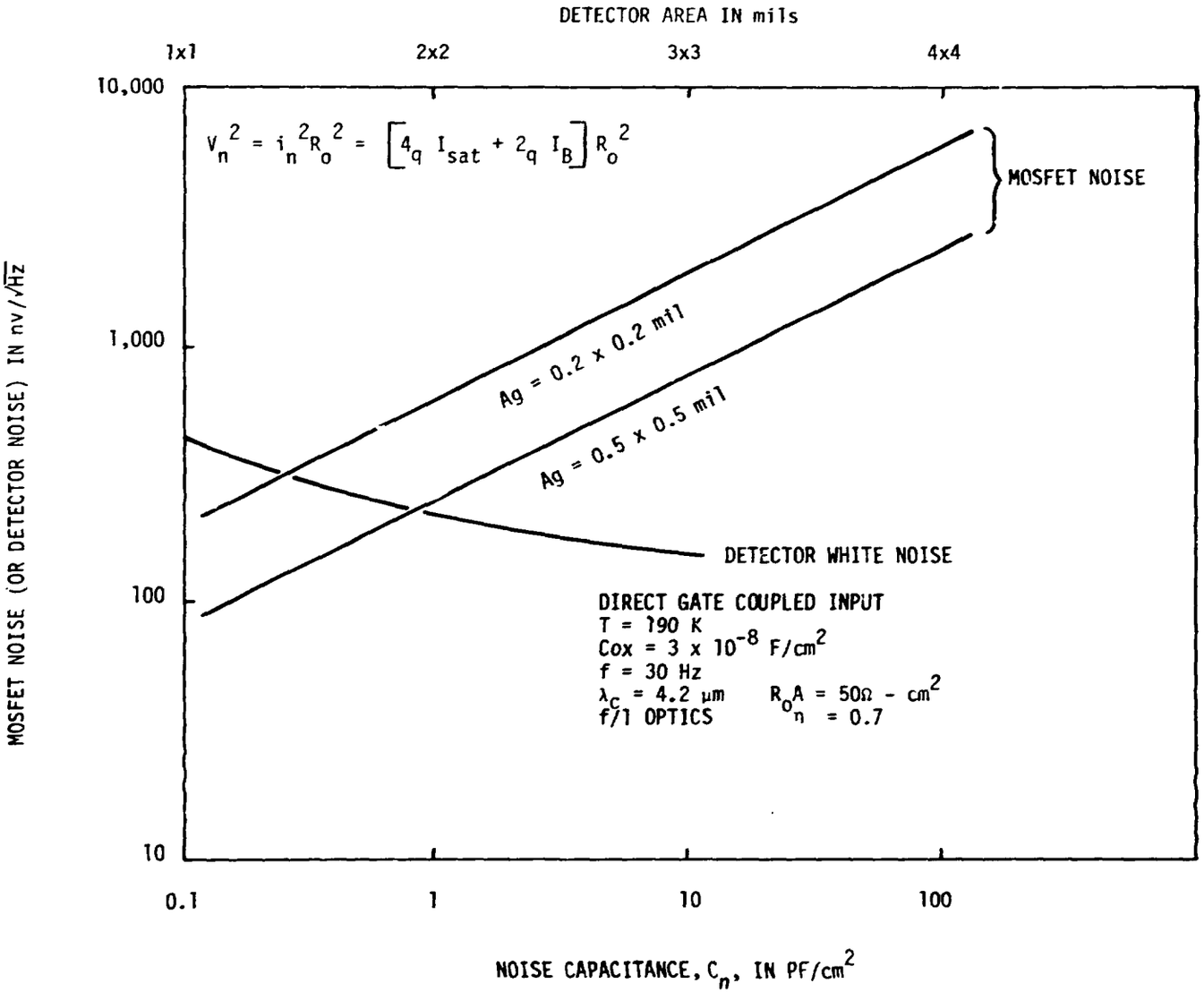

Figure 4-34. Input Gate Noise vs. Noise Capacitance Factor and Detector Noise vs. Detector Area

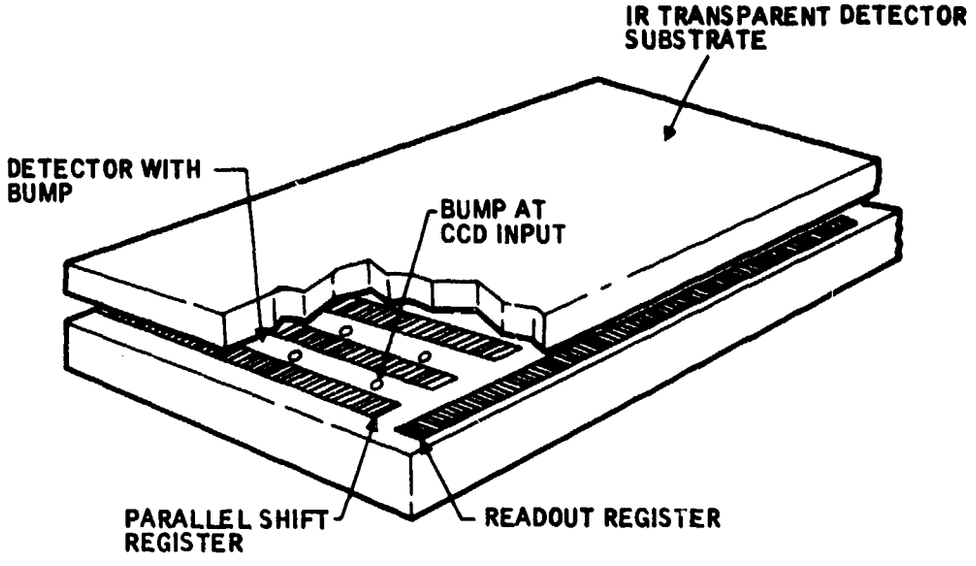

Detector/CCD Flip Chip Focal Plane Array

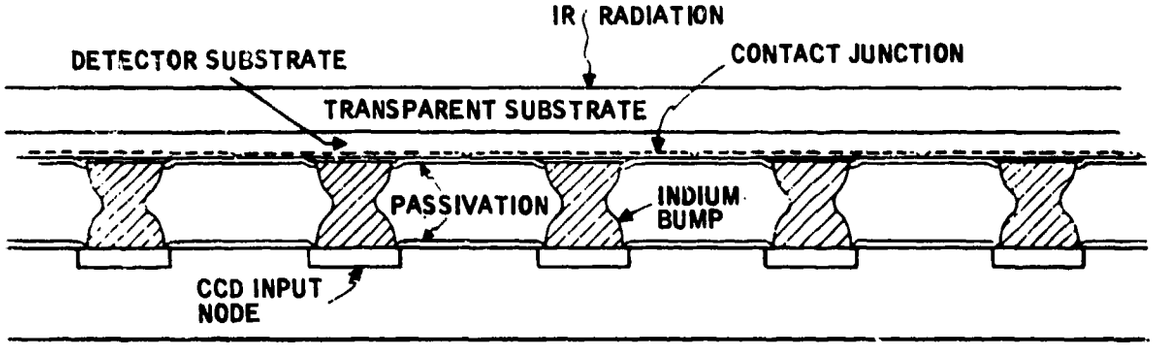

Figure 4-35. General Configuration of the Solder Bump Detector/ CCD Interface Used for Backside Illuminated Detector Structures

detector. Indium is an excellent material choice for use as the interconnect metal. In addition, the indium has excellent adhesion characteristics for gold contact pads used on the CCD. This is due to the fast diffusion coefficient of indium in gold at slightly elevated temperatures. The indium column forms an In/Au alloy at the interface of the bump and gold contact pad providing a natural transition of the two mating elements. The fact that the indium column or bump is an integral part of the CCD contact results in excellent adherence properties.

Any strain within the indium bump will occur in the bump interconnect rather than in the detector and CCD material due to the low yield-stress of indium over a large temperature range. If higher yield-stress materials were used, the interconnect would become brittle at cryogenic temperatures. Choice of materials like Ag and Ga alloys have a lower stress but are difficult to contact at room temperature. Another excellent property of indium is its low melting point which implies a low work-hardening coefficient. A low work-hardening coefficient has an important effect: damage in the indium bump interconnect will not be cumulative upon repeated cooling cycling due to its ability to anneal out damage at room temperatures. Other materials that work-harden easier would fail after a certain number of thermal cycles. Figure 4-36 shows a diagram of a detector array and CCD readout electronics chip after the array has been brought down to operating temperatures. In this case the detector array has a larger thermal expansion coefficient than the silicon CCD substrate, and it has been assumed that the bumps remain aligned at the left side of the diagram. The maximum allowable expansion differential which can be tolerated depends on many factors including:

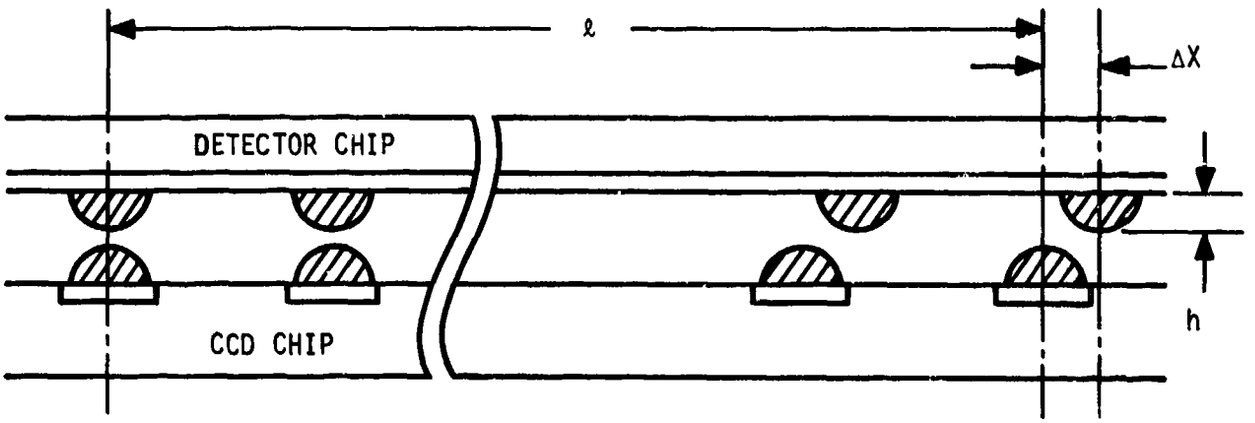

Figure 4-36. Detector and CCD Arrays at Operating Temperature

- Array length
- Thermal expansion coefficient of detector array
- Thermal expansion coefficient of CCD substrate
- Bump height, h
- Bump ductility
- Bump width and spacing
- Focal plane operating temperature

The value of Δx in Figure 4-36 is a function of the relative thermal expansion coefficients of the detector and CCD. Figures 4-37 and 4-38 show a plot of the thermal expansion coefficient and percent contraction as a function of

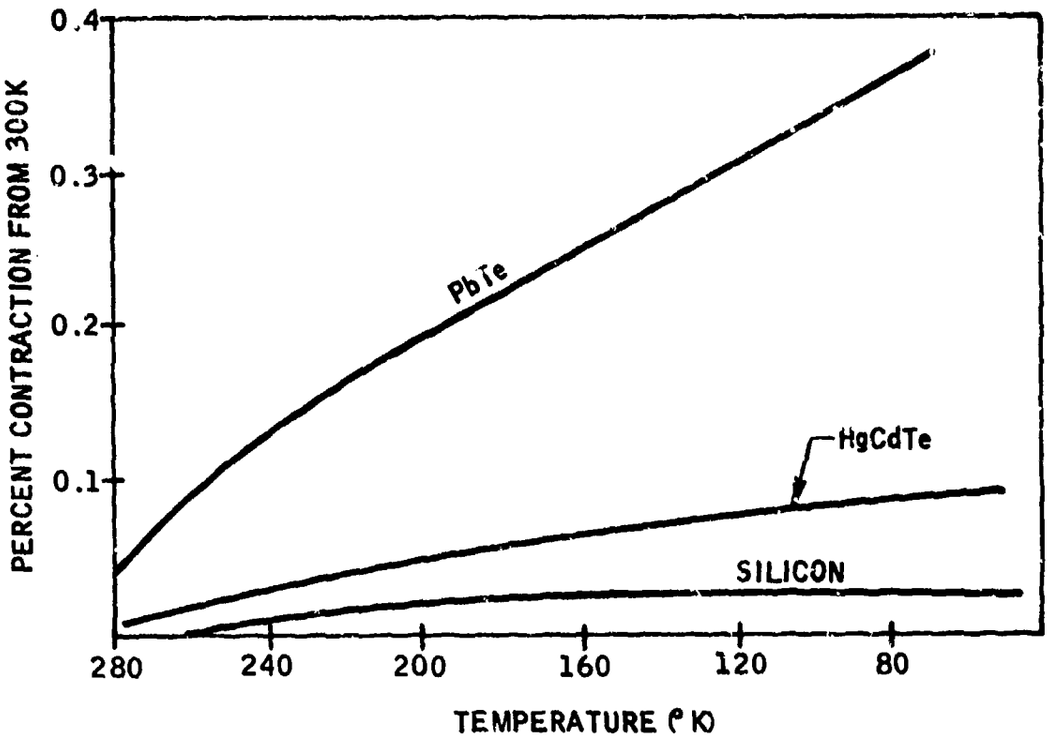

Figure 4-37. Materials' Compatibility with Silicon (Percent Contraction from 300 K to Final Temperature)

the operating temperature for various detector materials. It can be seen that the Pb-salt detector materials have a relatively large expansion coefficient which differs considerably from the CCD silicon substrate. For a 1 x 1 mil or 2 x 2 mil array with bump heights of about 1 mil, the value of Δx should be limited to about 8 μm so that shorting does not occur between adjacent inputs. This means that $(\Delta \ell_{det} - \Delta \ell_{si}) = 8\ \mu m$

Table 4-10 lists the $\Delta \ell$ values for HgCdTe, Pb-salt, and silicon for different total lengths, ℓ, when cycling to 190 K.

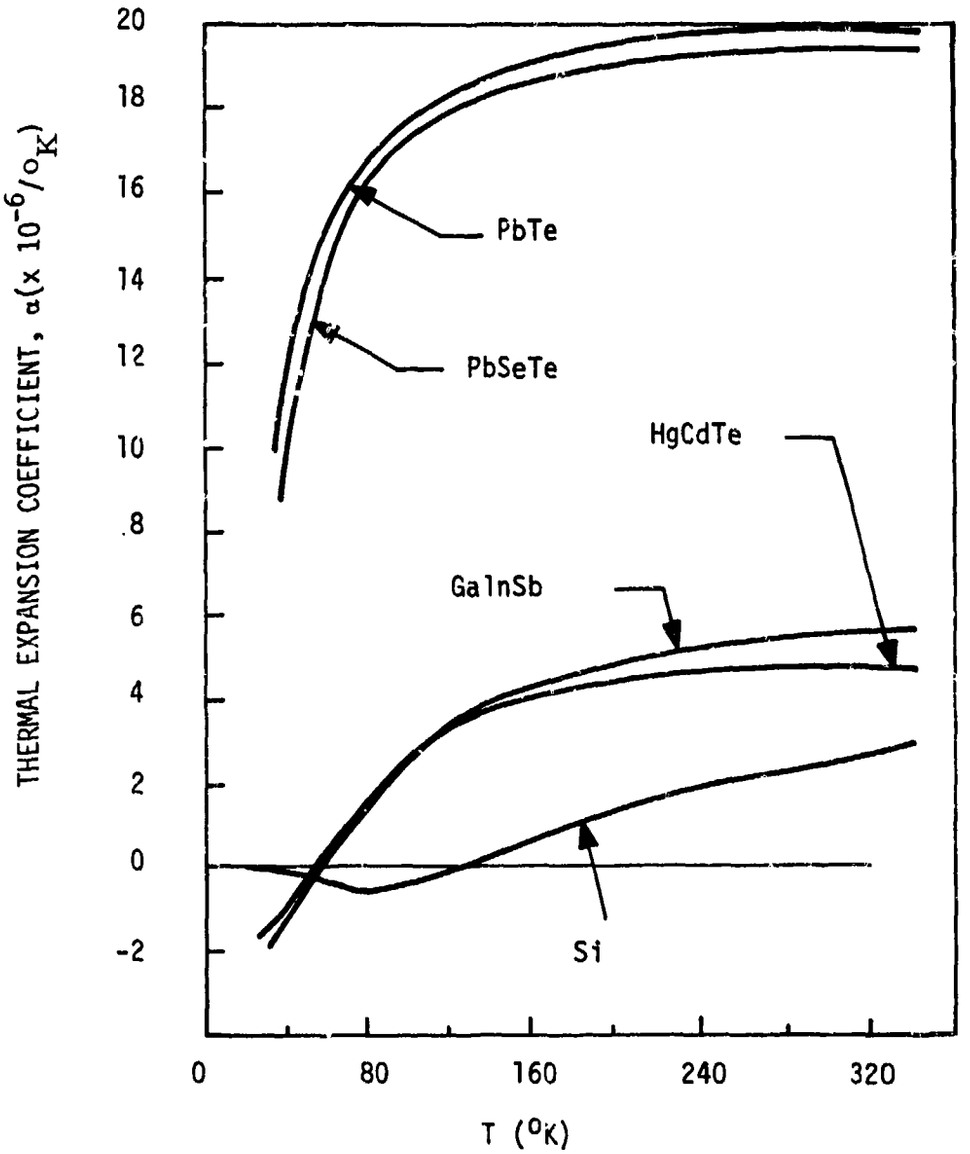

Figure 4-38. Linear Thermal Expansion Coefficients vs. Temperature

TABLE 4-10. ARRAY EXPANSION VALUES FOR DIFFERENT ARRAY LENGTHS[ΔT = (300 - 190 K)]

ℓ (mils)	$\Delta\ell$ (HgCdTe) (μm)	$\Delta\ell$ (Pb-salt) (μm)	$\Delta\ell$ (Si) (μm)
50	0.63	2.5	0.25
100	1.25	5	0.5
200	2.5	10	1.0
400	5.0	20	2.0

The differences in $\Delta\ell$ values show that the Pb-salts are limited array sizes of about 150 mil (from center to edge) or about 300 x 300 mil whereas the good expansion match between HgCdTe and silicon make extremely large chip sizes possible with the flip-chip approach.

Interconnect Shear Strain

Consider the strain that develops when the detector/CCD is cooled to cryrogenic temperatures. Strain is the change per unit length in a linear dimension of a body which is due to an accompanying stress. Shear strain is measured at right angles to the dimension under consideration. The bump interconnects undergo a shear strain of an amount determined by the displacement, a , divided by the column height, b, as shown in Figure 4-39. For example, we can calculate the shear strain for a 200 x 200 mil focal plane using HgCdTe/(Si) CCD from Table 4-10. The worst case displacement at 190 K is

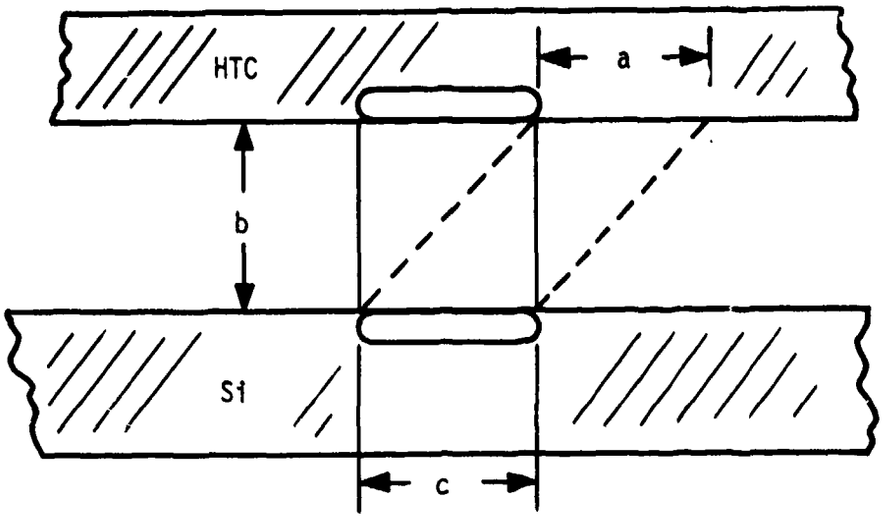

Figure 4-39. Bump Interconnect Shear Strain Due To Differential Thermal Expansion

$$(\Delta \ell_{det} - \Delta \ell_{si}) = 2.5\ \mu m - 1\ \mu m = 1.5\ \mu m$$

Keeping in mind that a shear strain of 0.2 is a very large strain, Table 4-11 shows the shear strain for various bump heights for HgCdTe/CCD cooled to 190 K using the worst case displacement.

TABLE 4-11. SHEAR STRAIN VS. BUMP HEIGHT FOR 200 x 200 MIL ARRAY AND ΔT = (300 - 190 K)

Bump Height (μm)	Shear Strain
.5	3
1 m	1.5
2.5	0.6
5	0.3
	----------max ≃ 0.2
10	0.15
15	0.1
20	0.075
25	0.06
30	0.05

From this table we can see that the indium column height must be greater than 5 μm in order to have reasonable shear strains when thermally cycled. Our present bump technology yields columns 20 to 25 μm in height which provides a wide safety factor in the mechanical design.

Interconnect Reflow

Reflow techniques can be used to increase the bump height-to-width ratio. The bumps are heated to a temperature near their melting point and are allowed to obtain a lowest energy configuratic Figure 4-40 shows an SEM

Figure 4-40. SEM Photo of As-Plated Indium Bumps (4 x 4 mil Centers)

photo of as-plated indium bumps on a PbTe detector array. Figure 4-41 shows these bumps after being reflowed at 150°C. The original flattened top has now been made more pronounced, thus increasing the bump height from about 15 μm to 20 μm. Similar techniques can be used on the CCD as shown in Figure 4-42 which shows the Honeywell 2181 CCD with reflowed indium bumps ready for mating to the detector array.

Bump Reliability

The detector/CCD focal plane interconnects must have both mechanical and electrical endurance under repeated thermal cycling. It has been shown that excellent mechanical and electrical continuity can be maintained through

Figure 4-41. Indium Bumps After Reflow at 150°C for Increase in Height-Width Aspect Ratio (Bump Height = 20 μm)

Figure 4-42. 32 x 32 CCD Readout Electronics with 1 mil Indium Bumps

the use of the indium bump interconnect. Honeywell has demonstrated this durability of the interconnect approach by operating a 32 x 32 element PbTe/CCD focal plane on IR&D funded programs. Repeated thermal cycling of these arrays showed no failures of the interconnects when cycling from 300 to 90 K.

SECTION V

FOCAL PLANE NONUNIFORMITY COMPENSATION

The low scene contrast for IR scenes (e.g., 3.5 percent/°K at 300°K for a five micron cutoff) means that responsivity and offset variations from one detector element to the next must either be held or corrected to less than 1 percent for "most" applications. With a scanning system, nonuniformity information is derived when the detector array scans across a reference source located outside the field of view. During the scanning of the reference sources, responsivity and offset equalization signals are calculated and are subsequently used to equalize the output signal.

With a staring focal plane system, it is necessary to introduce some element that will periodically interrupt the scene radiation incident on the focal plane and provide, instead, one (or two) reference levels of radiation. Potential candidates for this function are mechanical choppers, swing-in mirrors, and electro-optical modulators. Of importance here is the fact that when considering the applicability of staring focal planes for a particular application consideration must be given to the implementation of the chopping and reference level functions. The larger area of the staring focal plane relative to a scanning focal plane will require a larger reference source. Maintaining the requisite temperature uniformity across the source could influence the suitability of the staring focal plane concept for some applications.

SOURCES OF NONUNIFORMITY

Channel-to-channel nonuniformity can arise from many variables in focal plane associated with the IR detector, CCD signal processor, and temperature reference which may be used in a compensation circuit or radiometric system. Figure 5-1 illustrates the transfer characteristic of a detector from input scene temperature to focal plane output signal. The shaded area represents the variability from channel to channel. At TE-cooled temperatures, PV detectors are presently operating non-BLIP, and a significant dc signal component exists due to diode diffusion current. In order to determine the effect of diode and input coupling variables on uniformity, the PV diode current is computed. Considering a source-coupled input with the detector operating under reverse bias conditions, both diode diffusion current (I_s) and photocurrent (I_ϕ) are integrated into the CCD, and the CCD input current can be expressed as

$$I_{CCD} = g_1 (I_s + I_\phi) \tag{5-1}$$

where g_1 is a transfer gain which is a function of injection efficiency and CCD transfer efficiency. The photocurrent can be expressed as signal and background components related to scene temperature as follows:

$$I_\phi = g_2 \phi_T \tag{5-2}$$

$$\phi_T = \phi_P (1 + C_o \Delta T + C_1 \Delta T^2 + ---) \tag{5-3}$$

where g_2 is a transfer gain which relates photodiode carrier generation to photon flux (ϕ_T) and C_o, C_1, etc. are contrast constants which relate photon

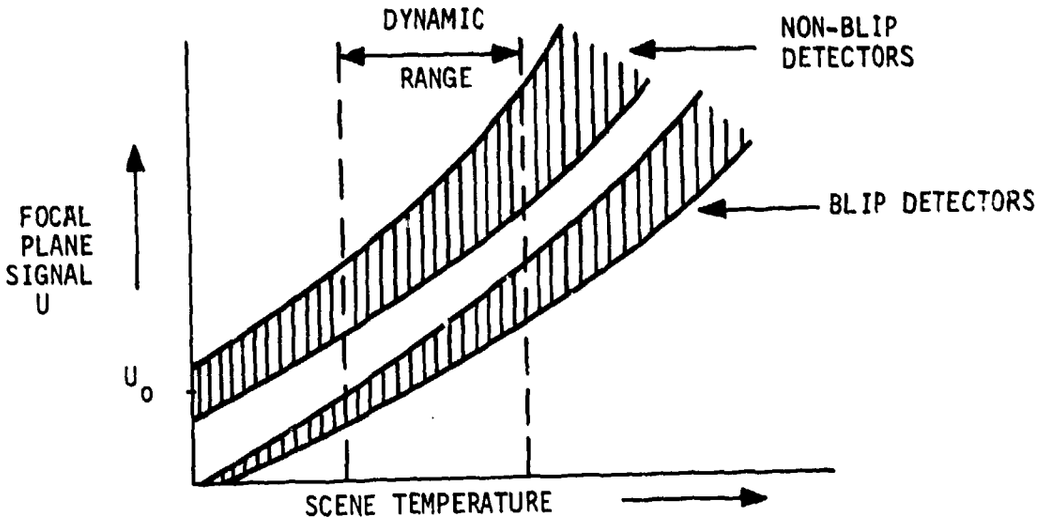

Figure 5-1a. Channel-To-Channel Variations Due To Differences In Offset And Detector Responsivity

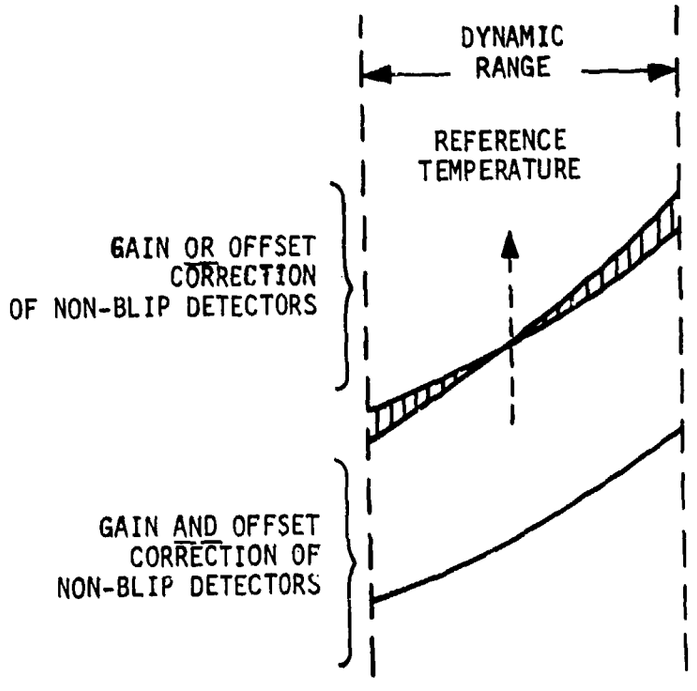

Figure 5-1b. Effects of Automatic Responsivity Control Approaches on Channel-To-Channel Variations

flux to scene temperature, optics, atmospheric path properties, and spectral band. For a uniform scene ($\Delta T = 0$), the two current components are

$$I_B = q \eta A_d T_r \phi_B \tag{5-4}$$

$$I_s = \frac{KT A_j}{q (R_o A)} \tag{5-5}$$

Figure 5-2 is a plot of the diode currents calculated for the following parameters:

$\eta = 0.7$

A_d = detector sensitive area = 1.5 x 1.5 mil

T_r = path transmission = 1

ϕ_B = photon flux/cm^2

T = 190°K

f/1 optics

300°K scene

A_j = detector junction area = 1.5 x 1.5 mil

In most cases the diffusion current is greater than the photocurrent and therefore is a significant source of nonuniformity. This figure indicates the effect of R_oA variations and input flux variations on the diode current components.

Table 5-1 summarizes the sources of channel-to-channel nonuniformity. The detector R_oA product is the principal performance limitation and also has the largest variation in TE-cooled applications. This situation will

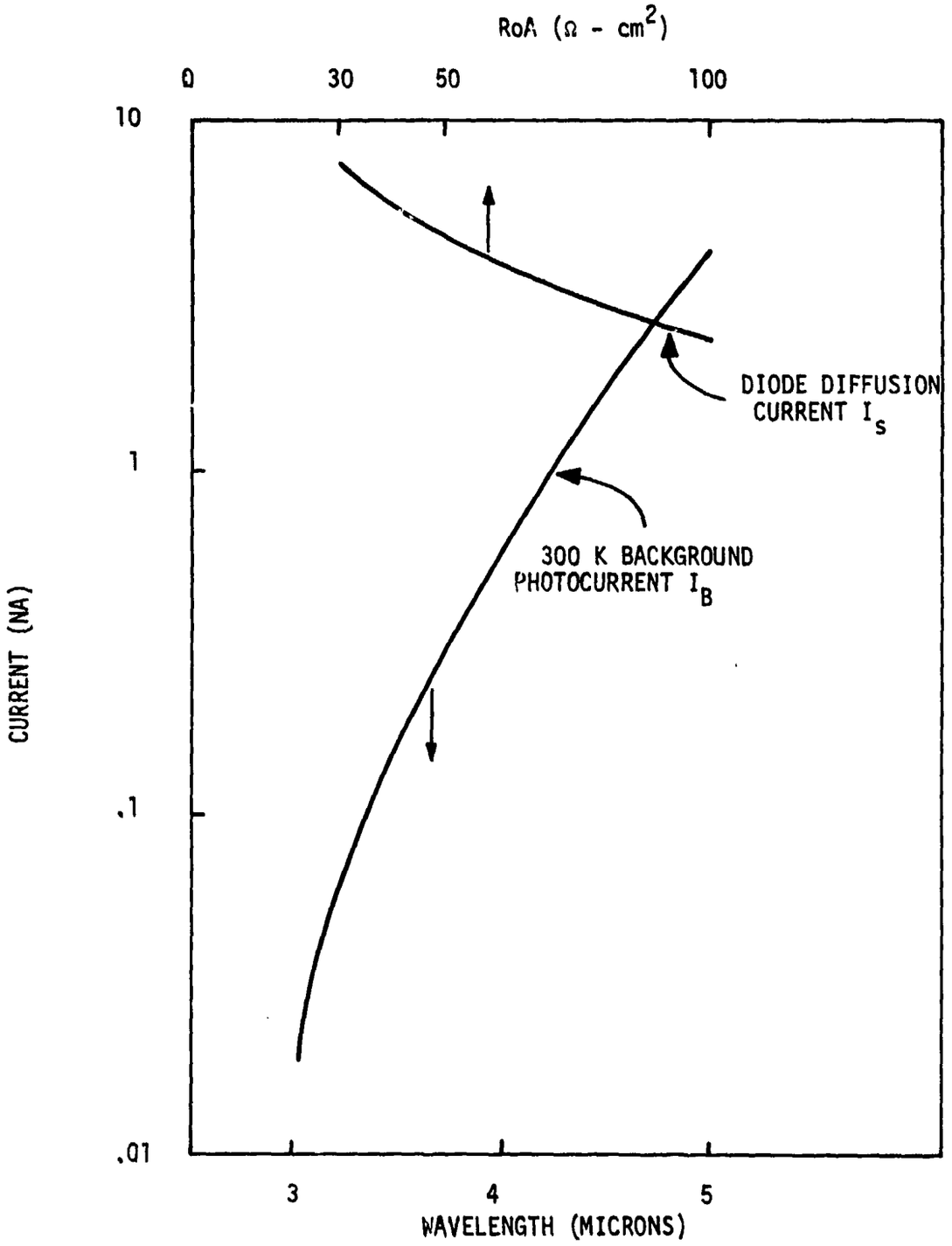

Figure 5-2. Detector Diffusion and Background Currents for Different R_oA Products and Cutoff Wavelengths, Respectively

TABLE 5-1. EFFECT OF DIFFERENT DETECTOR, CCD, AND TEMPERATURE REFERENCE PARAMETERS ON GAINS AND OFFSET LEVELS

Component	Nonuniformity Source	Source Parameters	Effect		Temperature Sensitive
			Offset	Gain	
Detector array	Saturation current	Lifetime Doping Junction area	X	X	Yes
	Active area	Photolithography	X	X	No
	Quantum efficiency	Surface reflectance, lifetime	X	X	No
	Cutoff wavelength	Composition	X	X	No
CCD	Threshold voltage	Doping, Traps	X		No
	Transfer efficiency	CCD Design, Mobility		X	No
Temperature Reference	Emission	Temperature and emissivity uniformity	X	X	Yes
	Optics	Reflectivity "narcissus" effect	X	X	No

exist until R_oA's in excess of 100 Ω-cm^2 are achieved. At TE-cooled temperatures, diode shunt leakage current can be neglected. The diode optically sensitive area variation assumes a $\pm 1\,\mu$m photolithography resolution and registration tolerance. In good quality arrays, surface recombination and diffusion length variations have a small effect on quantum efficiency and variations are dominated by surface reflectance effects.

Compositional variations across an array can alter the bandgap and change the cutoff wavelength. These variations are expected to yield a $\pm$.05-micron cutoff wavelength error. Figure 5-3 shows the corresponding percentage change in photon flux for a 300°K scene. A technique which should be considered to minimize this source of gain variation is the use of an optical filter with a cutoff wavelength slightly below that of the detector cutoff.

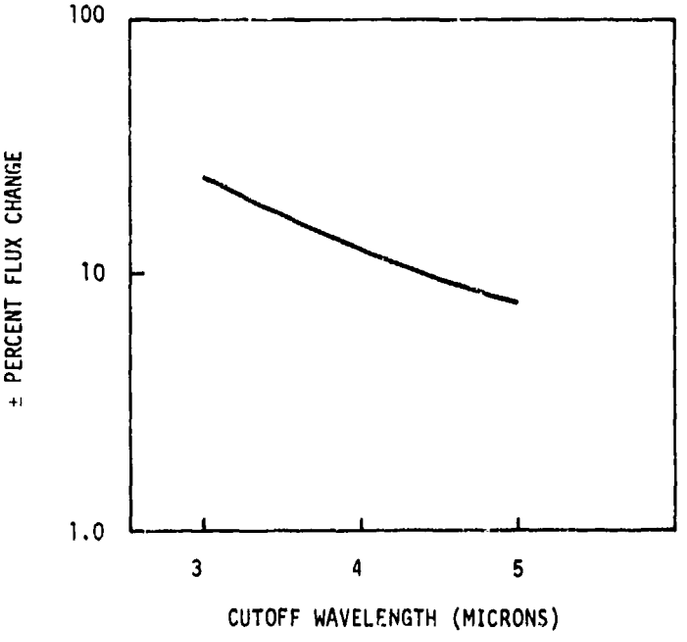

Figure 5-3. Photon Flux Variation for $\pm$ 0.05 μm Detector Cutoff Wavelength Variation as a Function of Wavelength for 300°K Scene

OFFSET COMPENSATION REQUIREMENTS

From Table 5-1 and the expression for the focal plane output signal as a function of the nonuniformity source parameters, we can calculate the compensation requirements necessary to achieve the minimum available NEΔT from the focal plane system. For a source-coupled input, the expression for the output signal is given by

$$-I_B = \underbrace{I_{CO} \exp \frac{q(V_g - V_t - V_s)}{KT}}_{\text{CCD Current}} - \underbrace{I_{SAT} \left(\exp \frac{-qV_s}{KT} - 1\right)}_{\text{Detector Current}}$$

where

I_B = background current

I_{CO} = CCD normalized current

V_s = source (or detector) voltage

V_t = input gate threshold voltage

V_g = input gate voltage

This expression can be rewritten in terms of the CCD input current normalized to the background current I_B:

$$\frac{I_{CCD}}{I_B} = - \frac{1 + \alpha + C(1 + \mu)}{1 + \frac{CD(1 + \mu)}{E(1 + C - CD)}}$$

where

$$\alpha = \frac{\Delta I_B}{I_B}$$

$$\mu = \frac{\Delta I_{SAT}}{I_{SAT}}$$

$$D = \exp \frac{-qV_d}{KT} \quad (V_d = \text{detector voltage and } V_d > 0 \rightarrow \text{reverse bias})$$

$$E = \exp \frac{-q\Delta V_t}{KT}$$

$$C = \frac{I_{SAT}}{I_B}$$

This expression can be simplified when considering the case of reverse bias detectors and reduces to

$$-\frac{I_{CCD}}{I_B} = 1 + \alpha + C(1 + \mu) - \frac{CD(1 + \mu)}{E}$$

or

$$\Delta I_{CCD} = \Delta I_B + \Delta I_{SAT}(1 - D) - I_{SAT}\frac{Dq\Delta V_T}{KT}$$

Normalizing this expression to the $NE\Delta T$ output current equivalent gives

$$\frac{\Delta I_{CCD}}{\Delta I_{NE\Delta T}} = \frac{\Delta I_B + \Delta I_{SAT}(1 - D) - I_{SAT}\frac{Dq\Delta V_T}{KT}}{(\text{Contrast}) X (I_B) X (NE\Delta T)}$$

The ΔI_B term is dependent upon variations in quantum efficiency and detector active area and can most easily be throught of as dependent upon $\Delta\eta$ A variations. In addition, variations in the detector cutoff wavelength also contribute to the ΔI_B term. ΔI_{SAT} is dependent upon the detector dynamic resistance and therefore the R_oA product variations. Figures 5-4 through 5-7 show the effects of the focal plane output signal variations, normalized to the number of NEΔT unit variations, with respect to the variations from channel-to-channel in the different parameter functions. These calculations were made for detectors which are non-BLIP and we have assumed the detectors are source-coupled into the CCD and nominally operated under reverse bias conditions.

Figure 5-4 shows the effect of $\Delta\eta$ A variations on the output variations. The $\Delta\eta$ A levels are about $\pm$ 5 percent, thereby resulting in an offset nonuniformity of about 500 NEΔT levels. (For 66 dB dynamic range on the focal plane this means an observed output nonuniformity of about 25 percent.)

Figure 5-5 shows the effect of the R_oA product variations on the output offset. ΔR_oA values are typically on the order of $\pm$ 10 percent, resulting in offset variations of about 1000 NEΔT levels ($\approx$ 50% of maximum output signal).

Figure 5-6 shows the effect of variations in the long wavelength cutoff on the output variations. These variations can be virtually eliminated by use of a cutoff filter which restricts the radiation incident on the detectors to a well-defined spectral band.

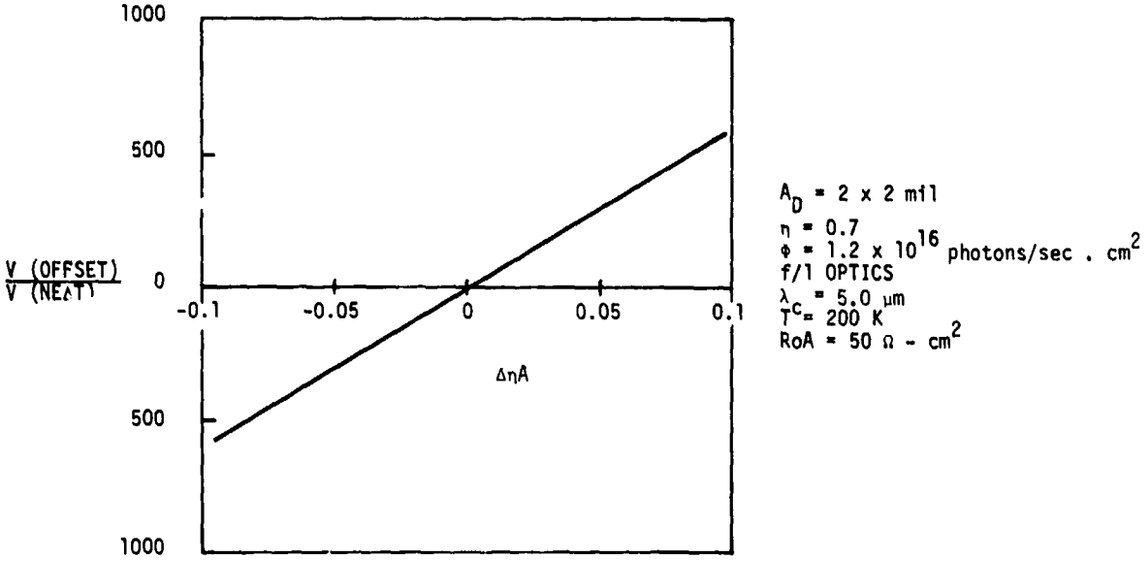

Figure 5-4. Effect of (η A) Variations on Output Offset for NEΔT = 0.01 K

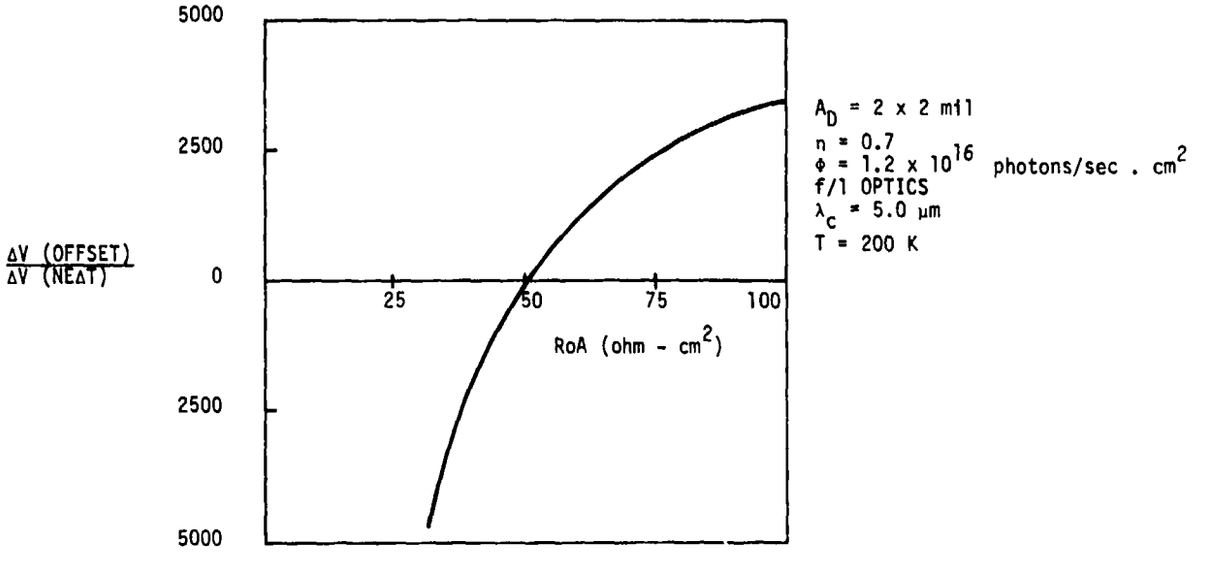

Figure 5-5. Effect of R_oA Variations on Output Offset for NEΔT = 0.01 K

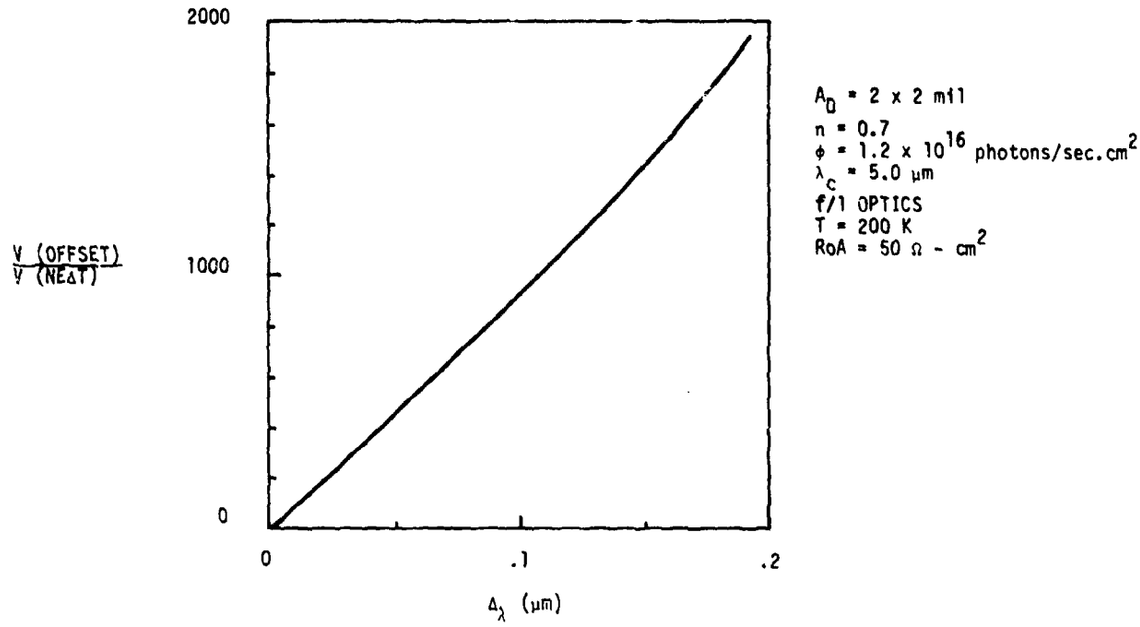

Figure 5-6. Effect of Cutoff Wavelength Variations on Output Offset for NEΔT = 0.01 K

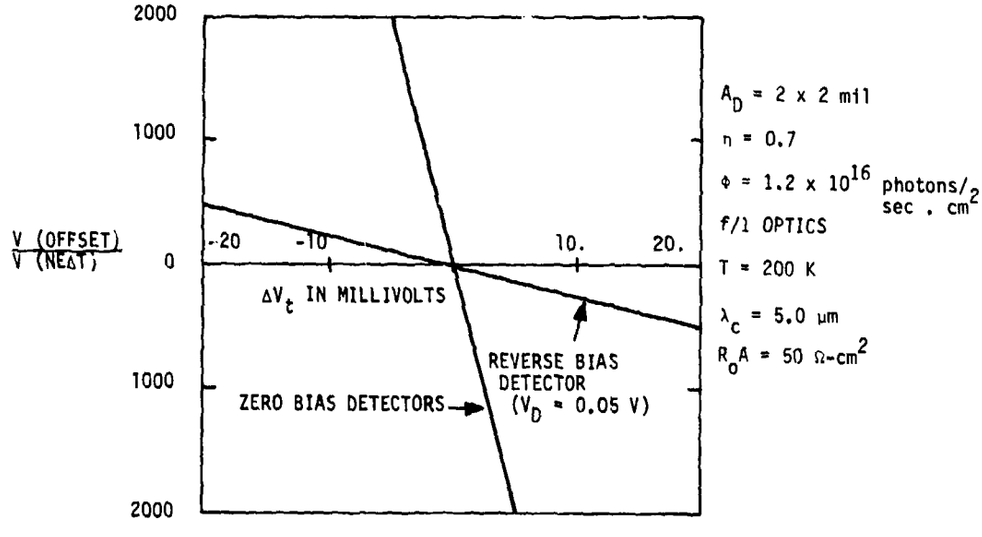

Figure 5-7. Effect of ΔV_T Threshold Variations on Output Offset for NEΔT = 0.01 K

Figure 5-7 shows the effect of the CCD threshold variations on the output signal. In this case the reverse biased detectors operated with a ΔV_T value of $\pm$ 10 mV results in an output variation of 250 NEΔT levels.

In summary, the effect of the $\Delta\eta A$ and $\Delta R_o A$ variations dominates the output signal variations, for the source-coupled input considered, and effectively results in a fixed pattern which is about 50 percent of the maximum CCD signal amplitude. This then effectively reduces the system dynamic range by a factor of 2 and requires that the compensation circuitry essentially have a compensation accuracy comparable to the focal plane dynamic range. (It should be noted that the $\Delta\eta A$ and $\Delta R_o A$ variations may in fact originate from the same source of variation since they are both active area dependent.)

The requirements are dependent, of course, on the particular input circuit configuration to the readout electronics and must be recalculated depending upon the detector/CCD coupling mode.

At TE-cooled temperatures, CCD dark current is negligible. Transfer inefficiency will cause a difference between the output level of the channel with the longest path through the CCD compared to the channel with the shortest path through the CCD. For a 128 x 128 detector array, two phase clocking, and a transfer inefficiency of 5×10^{-5}, the maximum gain loss is 2.6 percent. This corresponds to a gain variation of $\pm$ 1.3 percent. The impact of transfer inefficiency on gain for a FLIR display is to cause a gradual shading across the display rather than a random gain change. This subtle shading may not however be discernable by a human observer.

Nonuniformity compensation techniques may require the use of a temperature reference. An error signal (E) is generated by comparing the CCD output with the desired output (I_{REF}) when the detectors are viewing a reference temperature (T_{REF}). Thus,

$$E = I'_{CCD} - I_{REF} \tag{5-6}$$

$$I'_{CCD} = g_1 (I_s + g_2 \phi'_T) \tag{5-7}$$

where ϕ_T is the photon flux generated by the temperature reference. To minimize the uniformity requirements on the temperature reference, it can be located so as to be significantly out of focus. Then each pixel sees a spatial average of many (effective) pixels of the reference.

Thermal reference with less than 0.3°C end-to-end temperature difference can be maintained by using a suitable high thermally conductive material such as OFHC copper. The reference surface can be coated with a black paint such as 3M black velvet in order to have a high emittance. Point-to-point uniformity (over 0.01 inch areas) to within 0.01°C can be readily achieved.

To a large degree, the variables discussed above and summarized in Table 5-1 are fixed; that is, they are time and temperature independent. It may be possible, then, to do a large portion of uniformity correction with a fixed correction circuit rather than with a real-time feedback system. The major exceptions to this rule are discussed on the following pages.

The R_oA product of the detector has a large temperature coefficient. The temperature dependence for R_oA is dominated by the exponential term

$$R_oA \propto \exp \frac{qEg}{KT}$$

for a diffusion limited R_oA applicable at TE-cooled temperatures. Thus,

$$\frac{\Delta(R_oA)}{\Delta T} = \frac{(R_oA)qE_g}{KT^2} \qquad (5-8)$$

Since the bandgap E_g is related to the cutoff wavelength λ by

$$E_g = \frac{1.24}{\lambda}$$

at 190°K and λ = 4.2 microns, the temperature coefficient is

$$\frac{\Delta(R_oA)}{\Delta T} \cdot \frac{1}{R_oA} = 0.0947/^oK \qquad (5-9)$$

Thus to provide a fixed calibration compensation (i.e., not periodically re-corrected), the focal plane temperature stability must be exceptionally good. As an example for a focal plane instability of 1K, the $\Delta R_oA \simeq 10$ percent so that $\Delta R_oA = 5\ \Omega\text{-cm}^2$ for $R_oA = 50\ \Omega\text{-cm}^2$. Equation (5-9) then shows that this R_oA variation is equal to an output variation of 250 NEΔT levels. Thus focal plane temperature stability levels on the order of 0.01 K are necessary if fixed compensations levels are to be used.

COMPENSATION TECHNIQUES

The compensation techniques used to cancel out the offset and responsivity variations of the focal plane can be divided into two categories:

1. Offset compensation with stored responsivity correction
2. Offset plus responsivity compensation

The first category operates on the basis that, by carefully controlling the focal plane temperature, the detector responsivity variations remain invariant with time. The second category assumes that the responsivity and offset variations will be unpredictable during the mission time and therefore the correction coefficiency must be periodically or continually updated to maintain optimum performance.

Offset Compensation with Stored Responsivity Correction

As mentioned earlier, focal plane temperature variations on the detector responsivity result in different detector saturation currents because of the detector RA product variations.

Figure 5-8 shows a plot of the focal plane output signal variation as a function of the focal plane temperature uniformity. The output variations have been normalized to units of V(NE ΔT) where V(NE Δ T) = output signal equivalent to the minimum NE ΔT performance. From this figure we can see that it is necessary to maintain the focal plane temperature to within less than 0.01 K in order to use "permanently" stored responsivity correction factors.

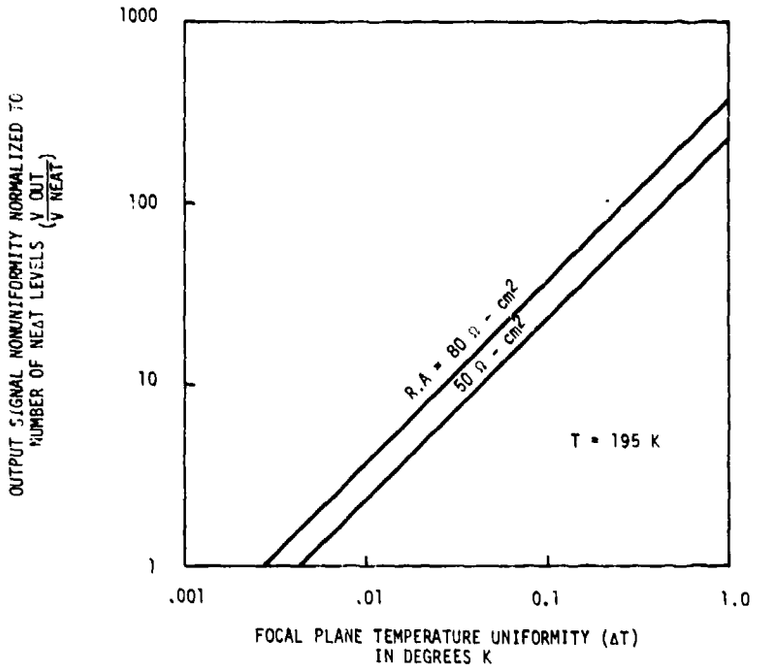

Figure 5-8. Focal Plane Signal Variation vs. Focal Plane Temperature Uniformity

Figure 5-9 shows a diagram of the general compensation circuitry used with this approach. The responsivity correction factors are stored in a PROM or ROM depending upon when the responsivity correction factors are evaluated.

At some point the offset nonuniformities are calibrated by having the focal plane look at a uniform temperature background. Various techniques can be used to store this nonuniformity information including the use of mechanical or electro-optical shutter, liquid crystal image divergers, etc. The stored reference signal is then subtracted from the subsequent video output signal on a corresponding bit-by-bit basis.

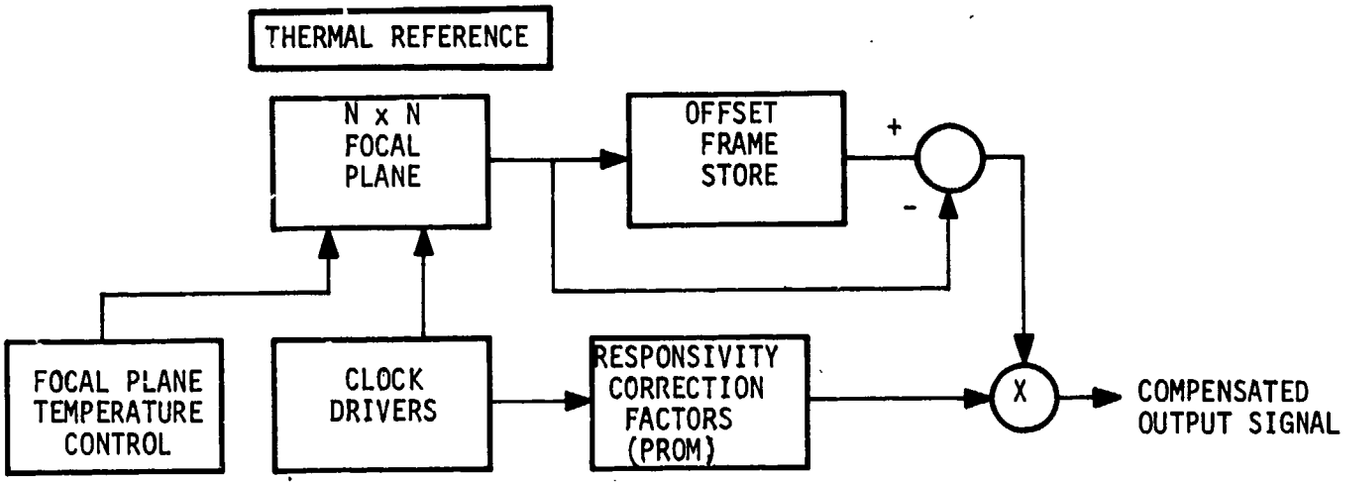

Figure 5-9. General Configuration Used in Focal Plane Compensation Using a PROM for Responsivity Correction Factors

Offset Compensation Techniques

Long-Term Averaging--Long-term averaging (Figure 5-10) is an ac coupling technique which normalizes the dc level for each pixel to an average value. Since a stationary image "washes out," the technique is only applicable to moving object detection or to panning systems.

Reference Frame Subtraction--In a system with a temperature reference, offset compensation can be implemented with the circuit shown in Figure 5-11. Each time the detector array views the temperature reference, the frame store memory is updated; when the array is viewing the scene, the frame store data is shifted out in synchronism with the array data and subtracted from it.

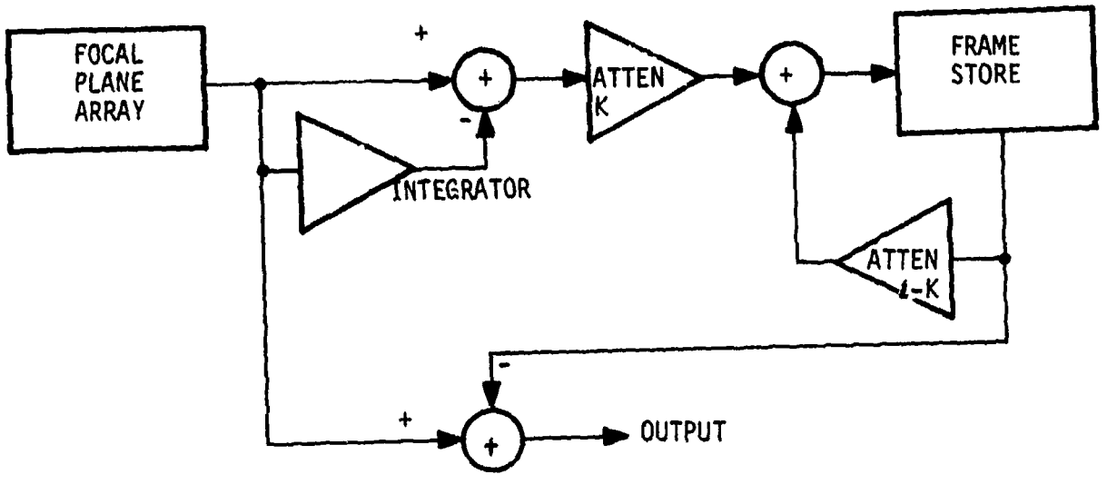

Figure 5-10. Long-term Averaging

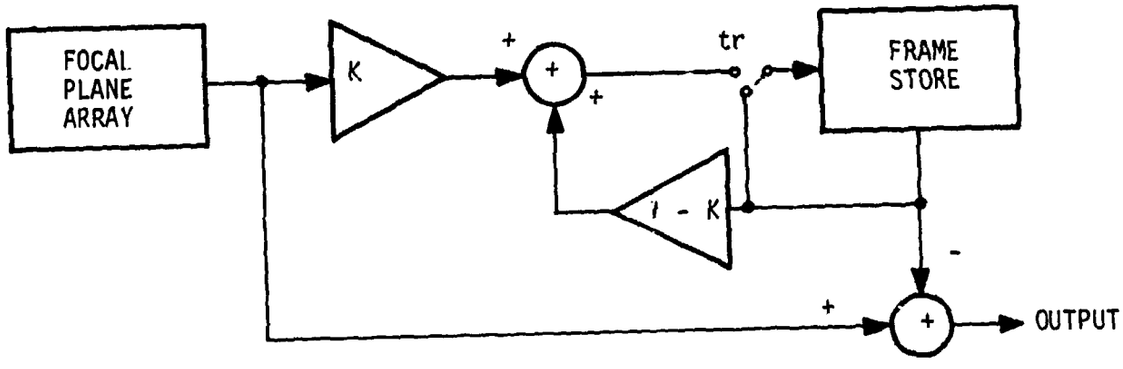

Figure 5-11. Reference Frame Subtraction

Figure 5-11 shows the frame store memory as a serial memory; thus the output data must be continually recirculated.

The attenuators K and (1 - K) form a low pass digital filter with a bandwidth K divided by the reference frame rate. Thus if all the noise is from the focal plane (no additional noise in the compensation circuit), the signal-to-noise ratio at the output is degraded by $\sqrt{1 + K}$. Making K small minimizes noise degradation at the expense of initialization time. This is a feed-forward correction circuit and relies on accurately setting the circulating loop to unity gain.

In Figure 5-12 feedback correction is used. The circuit functions are similar to those in Figure 5-11; however only error information is stored in the frame store. When the array is viewing the temperature reference, difference information, attenuated by K, is added to the frame store.

This circuit is more tolerant of gain variations in the circulating loops. However if it is assumed that the array views the scene M-1 times while the information in the frame store memory is recirculating and then views the reference once, the memory loop gain must differ from unity by less than $\pm$ MK for the circuit to be stable.

A second bound that can be placed on this circuit is that K must be on the order of the equivalent NEΔ T voltage so that there will be no discernable correction when viewing the temperature reference.

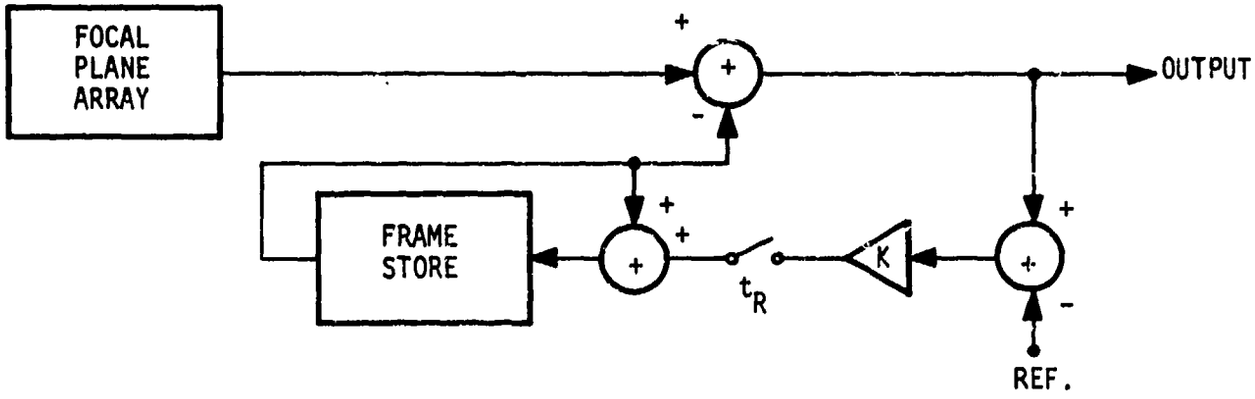

Figure 5-12. Feedback Reference Correction

Offset plus Responsivity Compensation

While the offset compensation is achieved by differencing the video data with a reference video frame, the responsivity compensation is typically implemented by multiplying a reference frame with the offset corrected video frame (Figure 5-13). If the focal plane temperature cannot be calibrated to the tight tolerances mentioned earlier, the responsivity correction coefficients must be periodically updated. As shown in Figure 5-13, the responsivity correction coefficients are typically calibrated through the use of a second temperature reference plane. The offset reference T_1 normalizes the output signal to the T_1 signal by voltage shifting the individual output signal amplitudes. This then only normalizes the output signals at a particular temperature. To achieve full compensation over a wide scene

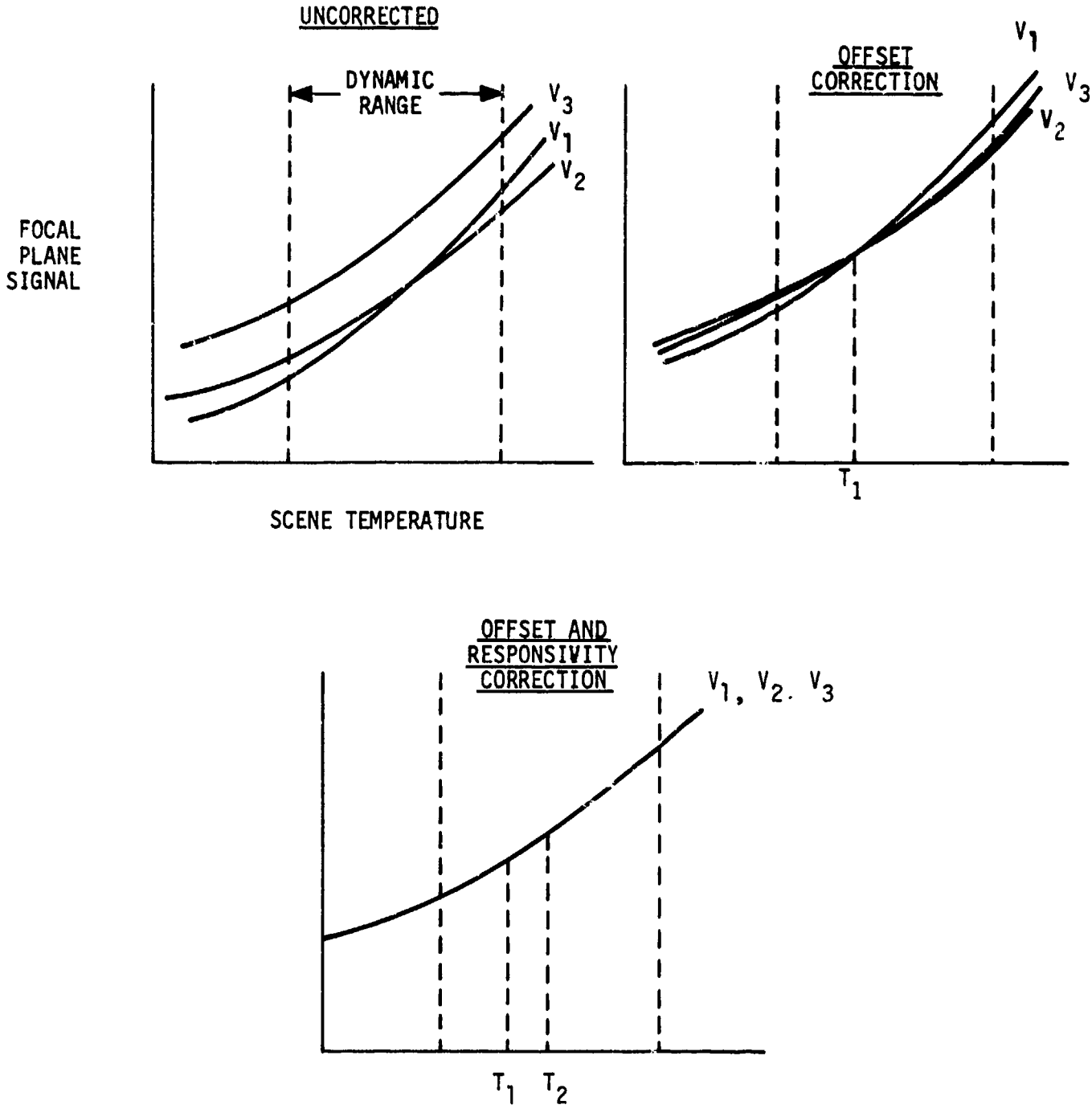

Figure 5-13. Use of Two-Temperature Reference Levels for Offset and Responsivity Correction

temperature range, the offset corrected transfer characteristic is normalized by means of a multiplication factor as indicated in Figure 5-13. The output signal S(ij) from the focal plane can be expressed as

$$S(ij) = R(ij) [\Phi_B + \Phi_s(ij)] + V_o(ij)$$

where

$R(ij)$ = responsivity of element in row i, column j (volts/photon)

Φ_B = background radiation flux

$\Phi_s(ij)$ = signal flux on element (ij)

$V_o(ij)$ = CCD offset amplitude from element (ij)

Figure 5-14 shows a block diagram of a digital implementation of the offset and responsivity correction circuitry. As indicated in the figure, the first two output frames F1 and F2 are obtained by having the focal plane radiated by uniform temperature references R1 and R2, respectively. These two frames are A/D converted and stored in the random-access-memory modules. By differing the F1 and F2 frames on a bit-by-bit basis, the responsivity values R(i, j) are determined since the differenced output from the RAMs is

$$S(ij) = R(ij) [\Phi_{B1} - \Phi_{B2}] = R(ij) \times \text{constant}$$

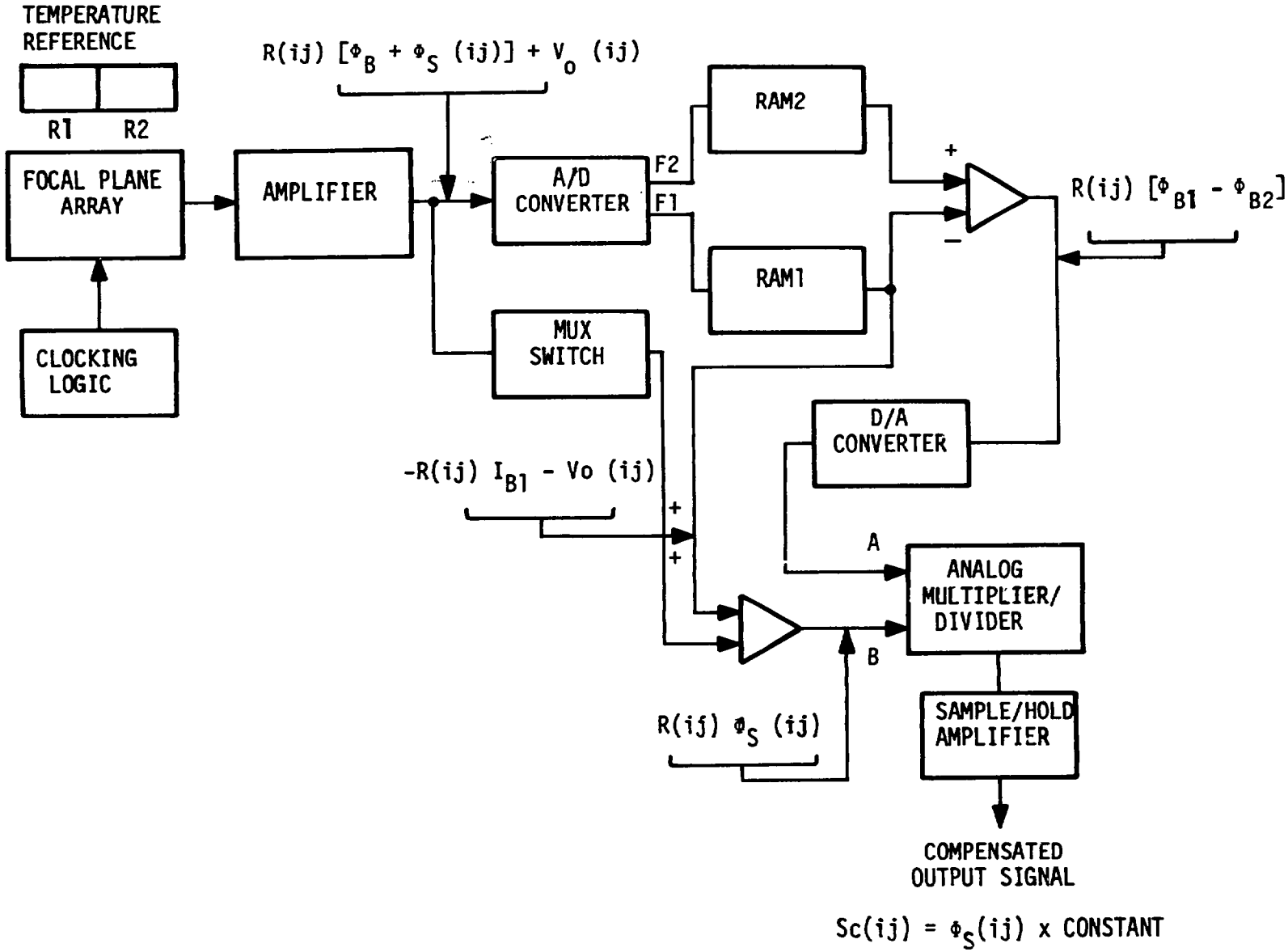

Figure 5-14. Digital Offset and Responsivity Compensation Circuitry

where

Φ_{B1} = radiation flux from reference R1

Φ_{B2} = radiation flux from reference R2

The output of RAM1 is given by

$$S(ij) = - R(ij)\, \Phi_{B1} - V_o(ij)$$

When this is differenced with the focal plane output signal, the offset coefficients are removed. The inputs to the analog multiplier/divider are

Input A: $R(ij)\,[\Phi_{B1} - \Phi_{B2}] = R(ij) \times \text{constant}$

Input B: $R(ij)\ \Phi_s(ij)$

Dividing input B by A gives the corrected output signal $S_c(ij)$ of

$$S_c(ij) = \frac{R(ij)\,\Phi_s(ij)}{R(ij) \times \text{constant}} = \Phi_s(ij) \times \text{constant}$$

which shows the corrected output signal as a function of only the signal radiation level.

Compensation can also be achieved by using all analog techniques. Figure 5-15 shows a diagram of an implementation in which CCD serial/parallel/serial delay lines are used to temporarily store the compensation coefficients. In this case the stored correction coefficients are recirculated back through the delay lines to compensate several successive output frames.

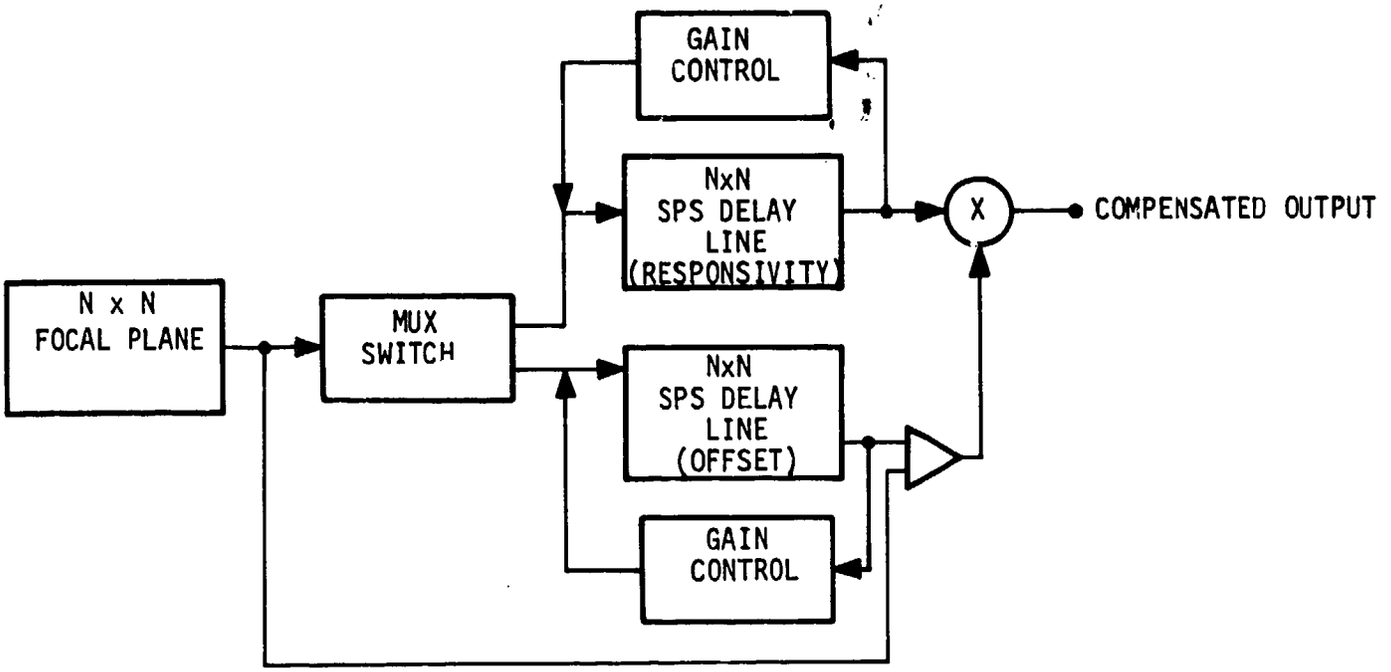

Figure 5-15. Nonuniformity Compensation Using Recursive Delay with Analog CCD Delay Lines

The number of recirculations is determined by the magnitude of the degradation of the correction coefficients through the transfer inefficiency of the CCD. The reduction of MTF of the stored signals is determined by the $N\epsilon$ product (number of transfer times the transfer inefficiency).

For a N x N array, each recirculation requires $2N \times \Phi$ transfers where Φ = number of transfers per bit. For a two-phase CCD, we then have 4N transfers per recirculation. To keep the $N\epsilon$ degradation below 2 percent requires $N\epsilon \leq 0.02$. For $\epsilon = 10^{-5}$ we have $N \times 4 \times 10^{-5} = 0.02$ or $N = 500$. Thus a 250 x 250 array could have the correction coefficients recirculated once, or in other words the thermal referencing would only have to be done every other frame. Similarly this approach could store the

coefficients for a 64 x 64 array for eight frames and would only have to be updated every ninth frame.

Supplement A discusses the implementation of a unique analog compensation technique called the Double Buffer CCD Memory (DBM) which Honeywell has been developing under IR&D funding.

DIGITAL OFFSET CORRECTOR PERFORMANCE

A digital offset compensation circuit was fabricated earlier at Honeywell and measurements were made to analyze its performance. Figure 5-16 shows a block diagram of the offset corrector circuit.

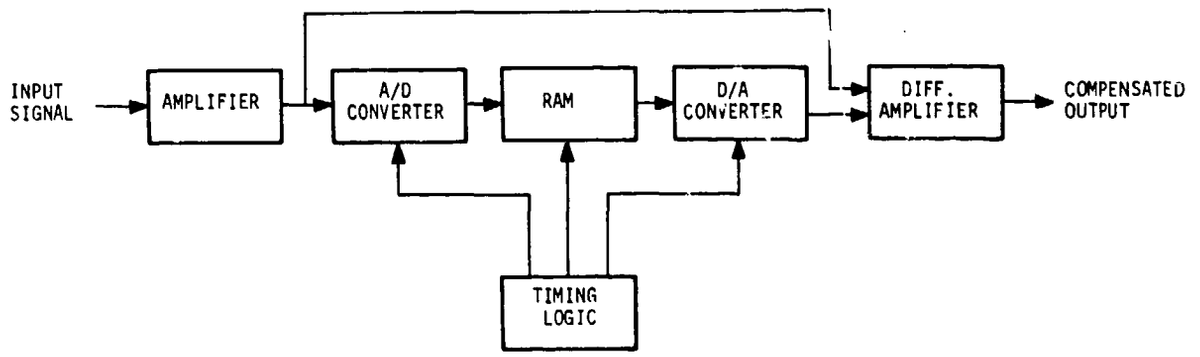

Figure 5-16. Block Diagram of Offset Corrector

Figure 5-17a shows a photo of a square wave input signal and the compensated output signal. This compensated output is the difference between the input signal and the stored signal. Ideally the compensated output signal is zero. At the transition of the square wave, a small "glitch" is seen which, in this case, is related to the synchronization between the input and output signals. The maximum output signal amplitude is 10 volts with a noise level of about 10 mv resulting in a 1000: 1 dynamic range.

Figure 5-17b shows a photo of a triangle waveform which has been stored in the RAM and is out of phase with the input triangle waveform. The differenced signal is shown on the lower trace where the phase differences are obvious. (A large discontinuity is shown after the 128 bits due to the resetting of the RAM output bits at this point).

The compensation circuit was operated in conjunction with the output signal from a CCD sensor. Figure 5-18 (top) shows a photo of the uncompensated output signal from the CCD (with particularly bad threshold variations chosen to dramatize the compensator performance). An ac chopped radiation signal is incident on the detector (which is small compared to the offset levels). The bottom trace (500 mV/cm) is the digitally compensated signal. Several items should be observed in this trace. A total of 15 elements are being read out and the digital electronics operate such that the first signal bit does not achieve full compensation. The vertical width of any one output represents the ac (out of sync) signal on the detectors. The variation in the ac signal amplitudes represents the detector

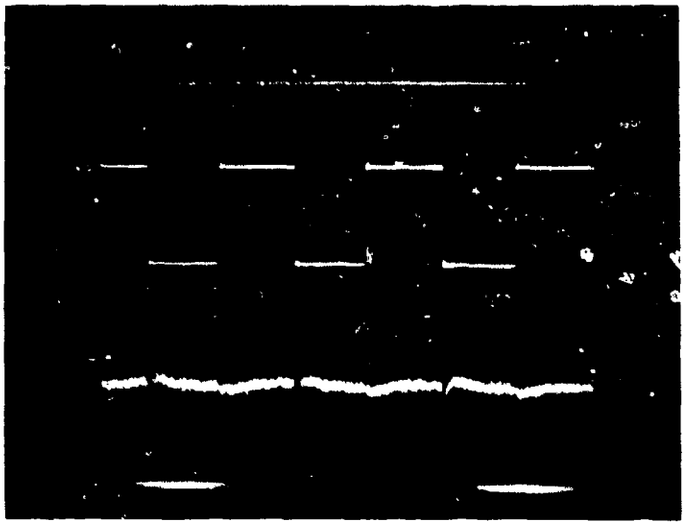

TOP:

A/D CONVERTER INPUT

5 V/cm x 500 μsec/cm

BOTTOM:

COMPENSATED OUTPUT

50 mV/cm

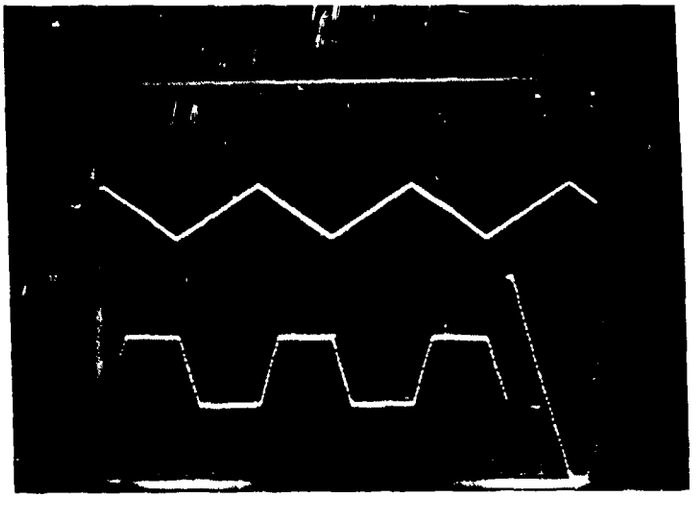

TOP:

OUT OF PHASE INPUT SIGNAL

2.5 V/cm x 500 μsec/cm

BOTTOM:

COMPENSATED OUTPUT

2V/cm

Figure 5-17. Digital Compensation Output Signals

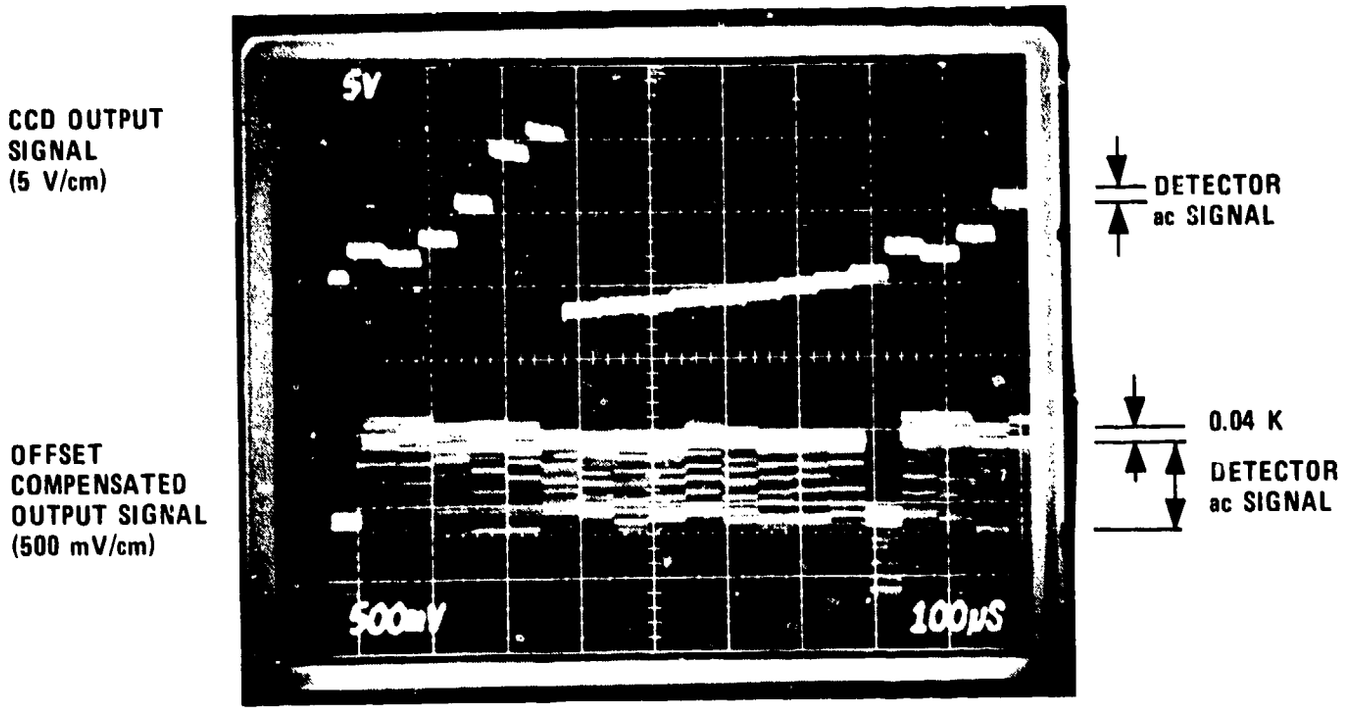

Figure 5-18. Performance of Digital Compensation Circuit on CCD Output Signal

responsivity variations which this circuit has not corrected. The top edge of the compensated output signals represents the compensation accuracy of this processor. This new compensation pattern noise level represents an NEΔT = 0.04 K for an 80 percent background suppression factor.

Power Dissipation

Power Dissipation levels in compensation circuits are a problem for many low power applications such as a hand-held viewer. Recent developments in the area of low power D/A, A/D, and low power digital memories make it possible to develop lightweight, low power compensation circuitry using digital

techniques. Table 5-2 lists the power dissipation requirements for both a digital and analog 8-bit offset and responsivity compensation circuitry.

For compensation of a 180 x 180 element array, a total of 8 CCD memory modules would be required for a total memory power dissipation of 1.6 watts (using the 32 K x 2 architecture of the Nippon digital CCD memory). Combined with the power requirements from the converters, analog multiplier, and timing logic, the total dissipation for such a compensator would be about 3.7 watts.

Analog circuits such as the recursive delay circuit of Figure 5-15 basically require power for the clock drivers, amplifiers, multipliers, and timing logic which would generally require less power than the digital implementation shown. For such cases power dissipation levels of less than 2 watts can be anticipated. This provides very low power, lightweight compensation circuits; however, one must update the correction coefficients of these circuits more frequently due to the temporary nature of the analog storage. Proprietary Supplement A describes the characteristics of Honeywell's DBM analog compensation circuitry where extremely low power dissipitation modules requiring infrequent updating are possible.

TABLE 5-2. COMPENSATOR POWER REQUIREMENTS FOR TYPICAL 180 x 180 ELEMENT FOCAL PLANE (8 bit accuracy-offset and responsivity)

Component	Type	Characteristics	Power Dissipation
DIGITAL			
A/D converter	TDC-1001J (TRW)	8 bit, 2.5 MHz	400 mW
D/A converter	DAC-08 (Precision)	8 bit, 11 MHz	33 mW
CCD digital memory	Nippon Electric	64K, 3.4 MHz (32K x 2 bits)	200 mW
Analog multiplier	429 (Analog Dev.)		150 mW
Timing logic circuits	Differential amps, MUX switches, etc.	10 MHz	1.5 watts
		Total dissipation	3.7 watts
ANALOG			
- Recursive delay CCD		10 bit, 4 MHz Requires frequent update	<2 watts total
- Honeywell's DBM compensator		Low duty cycle refresh	<2 watts total

SECTION VI

SYSTEM PERFORMANCE MODELING

To accurately model the performance of a staring focal plane requires special consideration of the dependence between the detector array spatial MTF and the detector bandwidth. By appropriately modifying the NVL Static Performance Model for Thermal Viewing Systems,[2] we can derive the MRT and NEΔT performance characteristics for the non-scanning focal plane.

MRT DERIVATION

The MRT for the staring syste is derived in a manner analogous to that used for the derivation in the NVL Performance Model. The signal and noise are calculated using a matched filter for the four-bar pattern as indicated in Figure 6-1. A discussion of the matched filter is given in the NVL Performance Model report. Essentially, the perceived signal and noise are calculated, and the MRT is the required temperature difference necessary to give a particular perceived signal-to-noise ratio. In the derivation outlined below, reference is made to equations in the NVL report.

The signal deriviation for the staring system is nearly identical to that for the scanning system, except for the relation between the focal plane signal

---

[2] J. A. Ratches et. al, "Night Vision Laboratory Static Performance Model for Thermal Viewing Systems," NTIS, April 1975.

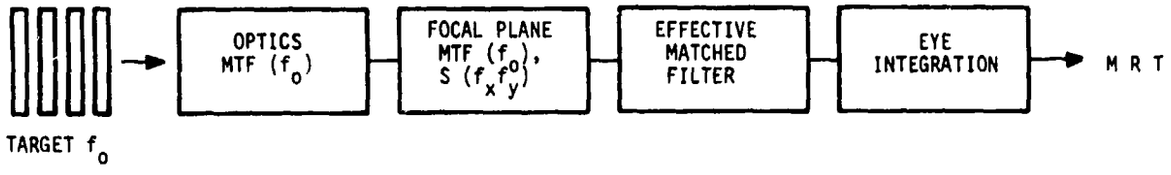

$$\text{EFFECTIVE MATCHED FILTER} = H_w(f_x)\, H_L(f_y)\, H_D(f_y)$$

Figure 6-1. MRT Calculation Model

and the display emission. For the staring system Equation (A27) is replaced by

$$M(x,y) = \frac{k' \Delta T\, i(x,y)}{\Delta x\, \Delta y} \qquad (6\text{-}1)$$

where the symbols have the same meaning as in the NVL report, and k' is defined such that $k' \Delta T$ equals the energy emitted by a display element for a large target with a temperature difference ΔT.

The evaluation of $i(x,y)$ proceeds identically with that for the scanning system, leading to

$$\text{Signal} = \frac{k'}{\Delta x\, \Delta y}\ \text{MTF}\,(f_o)\frac{8}{\pi^2}\,\Delta T \int_{-\infty}^{\infty} LH_L^2\ H_D^2\ df_y \qquad (6\text{-}2)$$

(The glossary at the end of this section defines the terms used throughout the analysis.) To evaluate the noise on the display, we need an expression for $S_1(f_x, f_v)$, the spectral density of the noise.

The spectral density of the noise which must be used is that from one detector, S_1. However, it is most straightforward to calculate the focal plane noise spectral density, S, and then relate it to S_1. The spectral density is derived from the spatial noise function, n(x, y). For a display excited by a staring focal plane, the spatial noise function is given by

$$n(x,y) = \sum_{i,j} ij\ h(x - x_i)\ g(y - y_j) \qquad (6\text{-}3)$$

where h and g are the impulse response functions of the display in the x and y directions, respectively, and n_{ij} is the noise from the (ij) detector. The important characteristic of the staring system is that the noise from the various detectors is uncorrelated, so that $n_{ij} = n_{kl}$ for $i \neq k$ or $j \neq 1$.

There are two equivalent methods to derive $S(f_x, f_y)$ from n(x, y). These derivations are shown in Appendix B.

As in the NVL report, the filter for the matched noise is

$$H_w(f_x)\ H_L(f_y)\ H_D(f_y)$$

Using $H_d(f_x, f_y) = H(f_y)\, G(f_y)$, we have the following for the MRT noise:

$$(\text{Noise})_p = \frac{(k' \, NE\Delta T)^2}{\Delta x \, \Delta y} \iint H_d^2(f_x, f_y)\, H_w^2(f_x)\, H_L^2(f_y)\, H_D^2(f_y)\, df_x\, df_y \tag{6-4}$$

The ratio of the signal given in Equation (6-2) and the noise given in Equation (6-4) gives the signal-to-noise ratio for a single frame. The MRT is the ΔT found by summing the signal to noise over the frames in an eye integration time and by setting the signal-to-noise ratio equal to a threshold value of 8:

$$MRT(f_o) = \frac{\pi^2 \, 8 \, NE\Delta T}{8\, MTF(f_o) \int_{-\infty}^{\infty} LH_L^2 H_D^2 \, dfy} \left\{ \frac{\Delta x \, \Delta y}{\tau_e \dot{F}} \iint H_d^2 H_w^2 H_L^2 H_D^2 \, df_x \, df_y \right\}^{1/2} \tag{6-5}$$

A normalized form of the integrals may be obtained by multiplying $W/W \cdot L/L$. Then for large bars the integrals will reduce to 1.0. Noting that

$$W = \frac{1}{2f_o} \; ; \; L = \frac{7}{2f_o}$$

we have

$$MRT(f_o) = \frac{\pi^2 f_o \, NE\Delta T \, 8 \left(\Delta x \, \Delta y \iint W H_w^2(f_x)\, L H_L^2(f_y)\, H_D^2(f_y)\, H_d^2(f_x f_y)\, df_x df_y \right)}{4\, MTF(f_o)\, (7\tau_e \dot{F})^{1/2} \int L\, H_L^2(f_y)\, H_D^2(f_y)\, df_y} \tag{6-6}$$

Using the definitions

$$q_y \equiv \int_{-\infty}^{\infty} LH_L^2(f_y)\, H_D^2(f_y)\, df_y \tag{6-7}$$

$$\rho_x \int_{-\infty}^{\infty} WH_w^2(f_x)\, H_d^2(f_x)\, df_y \tag{6-8}$$

$$\rho_y \int_{-\infty}^{\infty} LH_L^2(f_y)\, H_D^2(f_y)\, H_d^2(f_y)\, df_y \tag{6-9}$$

The MRT reduces to

$$MRT(f_o) = \frac{\pi^2 f_o\, NE\Delta T\, S}{4\,(7)^{1/2}\, MTF(f_o)\, q_y} \left(\frac{\Delta x\, \Delta y\quad \rho_x\, \rho_y}{\tau_e \dot{F}} \right)^{1/2} \tag{6-10}$$

This result is comparable to Equation (A-48) of the NVL report. The essential difference is in f_x, which for the staring system does not have any detector (temporal) frequency characteristics.

Writing the staring result and the scanning result in the same form, we have

$$MRT(f_o) = \frac{\pi^2 f_o\, S}{4\, MTF(f_o)\, q_y} \left(\frac{\Delta y\, \rho_y}{7\tau_e \dot{F}} \right)^{1/2} \cdot Q_i \equiv A \frac{Q_i}{MTF(f_o)}$$

$$Q_i = (\Delta x)^{1/2}\, NE\Delta T \left\{ \int_o^{\infty} 2H_d^2\, WH_w^2\, df \right\}^{1/2} \quad \text{(Staring)} \tag{6-11}$$

$$Q_i = \left(\frac{V_x}{2\,\Delta f_n} \right)^{1/2} NE\Delta T \left\{ \int_o^{\infty} 2\, \frac{S(f)}{S(f_o)}\, H_{elect}^2\, H_d^2\, WH_w^2\, df \right\}^{1/2} \quad \text{(Scanning)} \tag{6-12}$$

The similarity in results indicates that the NVL Static Performance Model Computer Program may, with suitable modifications, be used to model the

staring system. The calculation must be performed in two steps. The first calculation gives the spatial dependence of MRT, and the second gives the correct magnitude factor.

Step 1. F_x Dependence of MRT

For the first NVL model run, set $S(f)/S(f_o) = HB^2 = H^2_{elect} = 1.0$ and f^* (detector) very high. This allows the program to calculate the correct value for the integral in Equation (6-11). The program output will be

$$MRT_1(f_o) = A \frac{NE\Delta T_1}{MTF_1(f_o)} \left(\frac{V_1}{2 \Delta f_{n1}} \right)^{1/2} \left\{ \int_o^\infty 2H_d^2 WH_w^2 \, df \right\}^{1/2} \qquad (6\text{-}13)$$

The MTF_1 which has been calculated has the f_x dependence given by

$$MTF_1 = H_{OPT} \cdot H_{DET} \cdot H'_{DET} \cdot H_{ELECT} \cdot H_B \cdot H_{DISPLAY} \cdot H_{EYE} \cdot H_{LOS} \qquad (6\text{-}14)$$

With $H'_{DET} = H_B = H_{ELECT} = 1.0$, this MTF_1 is the same as the required MTF for the staring system since for that system there are no temporal MTF effects. The $NE\Delta T$ and Δf_n will not be the correct values for the staring system, and of course V_1 does not apply to the staring system. The long form NVL program output will give $MRT_1(f_x)$, $NE\Delta T$, Δf_{n1}, and V_1. Using the outputs, the result of Equation (6-13) may be rewritten in the following form:

$$\frac{MRT_1}{NE\Delta T_1}\left(\frac{2\Delta f_{n1}}{V_1}\right)^{1/2} = \frac{A}{MTF_1}\left\{\int_o^\infty 2H_d^2\, WH_w^2\, df\right\}^{1/2} \qquad (6\text{-}15)$$

where all the terms on the left-hand side of the expression are known. Comparing this equation with the MRT of the staring focal plane, Equation (6-11), we find

$$MRT\ (Staring) = (\Delta x)^{1/2}\, NE\Delta T\ (Staring) \cdot \frac{MRT_1}{NE\Delta T_1}\left(\frac{2\Delta f_{n1}}{V_1}\right)^{1/2} \qquad (6\text{-}16)$$

Therefore, all we now need to evaluate MRT (staring) is the correct value for $NE\Delta T$ (staring).

Step 2. NEΔT (Staring)

The second NVL program run is used to evaluate the correct value for $NE\Delta T$.

The $NE\Delta T$ is given by

$$NE\Delta T = \frac{4F^2\,(\Delta f_n)^{1/2}}{\pi\, a\, W\, D^*(f_o, \lambda_p)\sqrt{N}} \qquad (6\text{-}17)$$

with

$$\Delta f_n \equiv \frac{\int_f^\infty (I_n^2 + e_{1/f}^2/R^2)\left(\frac{R^2}{1+\omega^2R^2C^2}\right)\left(\frac{\sin\omega\tau/2}{\omega\tau/2}\right)^2 df}{R^2\, I_n^2(f_o) + e_{1/f}^2(f_o)} \qquad (6\text{-}18)$$

and

$$D^*(\lambda_{p1} f_o) = \frac{q\lambda_p na}{hc} \left\{ I_n^2(f_o) + e_{1/f}^2(f_o)/R^2 \right\}^{-1/2} \qquad (6\text{-}19)$$

This form for NEΔT may now be evaluated using the NVL scanned model. The required inputs are $D^*_{fo}(\lambda_p)$ given above and $S(f)/S(f_o)$ given by

$$\frac{S(f)}{S(f_o)} = \frac{\left(\dfrac{I_n^2 R^2 + e_{1/f}^2}{1 + \omega^2 R^2 C^2} \right) \left(\dfrac{\sin \omega\tau/2}{\omega\tau/2} \right)^2}{R^2 I_n^2(f_o) + e_{1/f}^2(f_o)} \qquad (6\text{-}20)$$

The NVL model imposes an additional filter H_{MD} in the calculation of NEΔT, where $H_{MD} = [1 + (f/f_o)^2]$; $f_o = 1/2T_d$. It is necessary to check that H_{MD} does not roll off the detector noise. One way to insure this is to input a large FOV/IFOV ratio and a large frame rate $\dot{F}$ for the NEΔT calculation. This will make T_d small and will make the H_{MD} roll-off occur at a higher frequency than the detector roll-off. The only useful output from this second NVL model run is the true detector NEΔT. This NEΔT is used with the results of the first computer in Equation (6-16) to give the staring MRT. Appendix C goes through an example case for the modeling of a particular staring focal plane.

MODELING RESULTS

The staring array performance model was used to calculate the performance characteristics of staring focal planes under various operating conditions.

Staring vs. Scanned Array Performance

Of particular interest is the comparison of performance between a staring array and a scanned (TDI) focal plane. The MRT for a scanned system is a function of the number of detectors in the TDI direction and, in fact, improves as $\sqrt{N_D}$ where N_D = number of detectors in the TDI direction. The staring array performance, however, is independent of the total array size since there is no correlation of data between the detector elements of the array.

The relative MRT performance characteristics between a parallel scanned imager with 350 x 4 (TDI) detector elements (PV) and a staring focal plane is shown in Figure 6-2. (The fact that the array size is not specified has no effect on the MRT performance characteristics since the modeling data inputs do not use the array size in the calculations.)

The detector R_oA products used in this modeling were the same for both systems and are as indicated in the figure. The staring array performance is about an order of magnitude better than the scanned array. To fabricate a scanned array with the same performance characteristics as the staring array, the number of detectors in the TDI direction would have to be increased to 520 elements. This is based on MRT $\propto$ NEΔ T/(overscan)$^{1/2}$ and the fact that NEΔ T $\propto$ overscan factor results in MRT $\propto$ (overscan)$^{1/2}$, and it assumes that overscan = 2. Thus a staring array will give comparable MRT sensitivity as a 350 x 520 (TDI) scanned array; the only difference in the system performance is the total FOV which is dependent upon the number of detectors in the staring array.

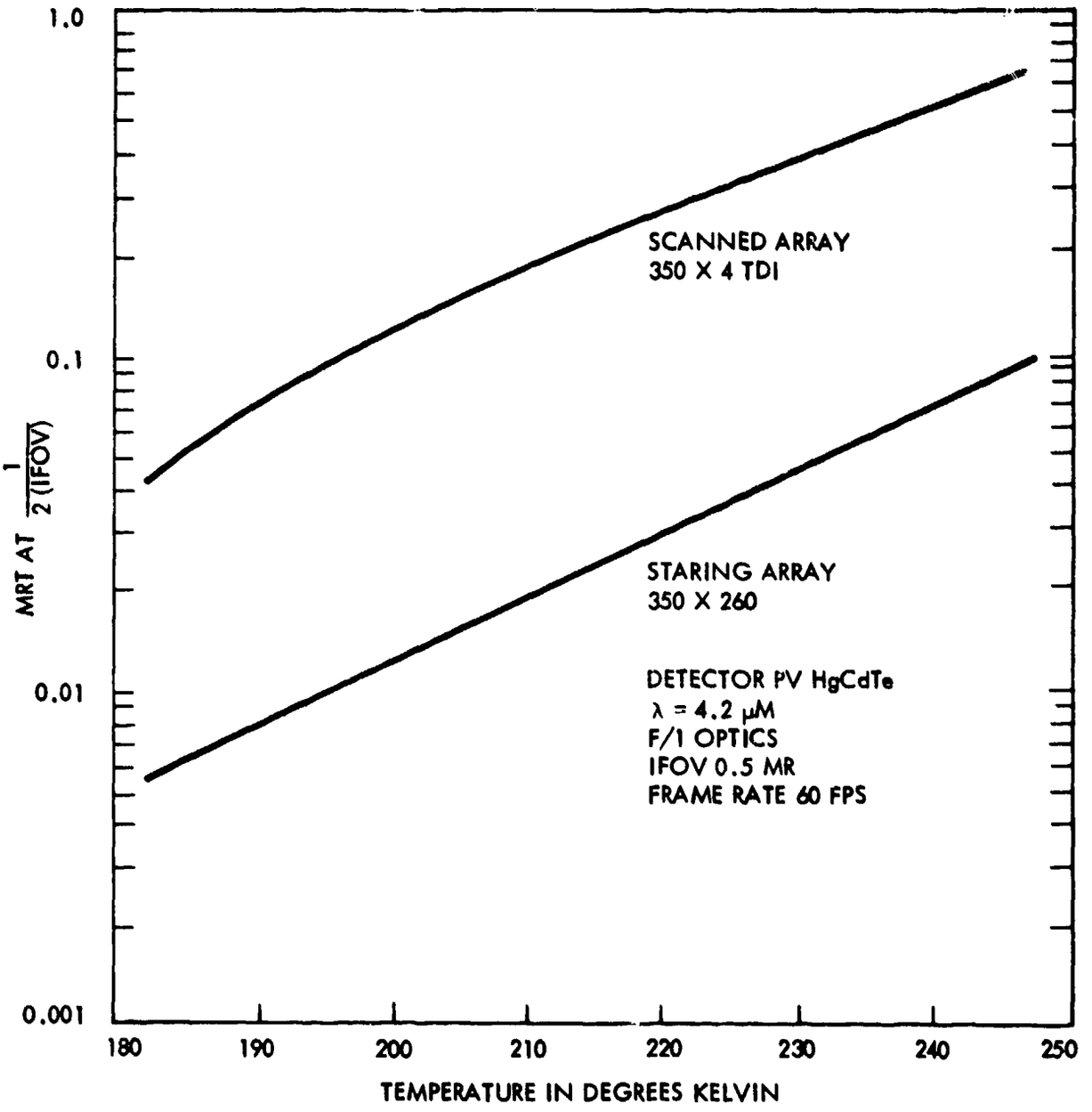

Figure 6-2. MRT vs. Temperature for Staring and Scanned Detector Arrays

Figure 6-3 shows a plot of MRT vs. spatial frequency for a 1 x 1 mil and 2 x 2 mil detector for the staring focal plane. These were calculated using the same optics diameter and optical f/number.

Effect of Frame Rate on NEΔT, MRT

The staring array frame rate can be varied and it is of interest to determine the performance characteristics as a function of the frame rate.

The effect of frame rate on the NEΔT is given in Reference 1 by

$$NE\Delta T = \frac{4F^2 \left(\Delta f_n\right)^{1/2}}{\pi A_d^{1/2} \eta_o (\lambda_p) D_p^* (\lambda_p) W} \qquad (6\text{-}21)$$

where

Δf_n = detector bandwidth

A_d = detector area

η_o = optical efficiency

D^* = detector D^*

W = normalized $D^* \eta$ integral

F = optical f/number

As shown in this equation, the NEΔT is proportional to the square root of the detector bandwidth (and thus the frame rate).

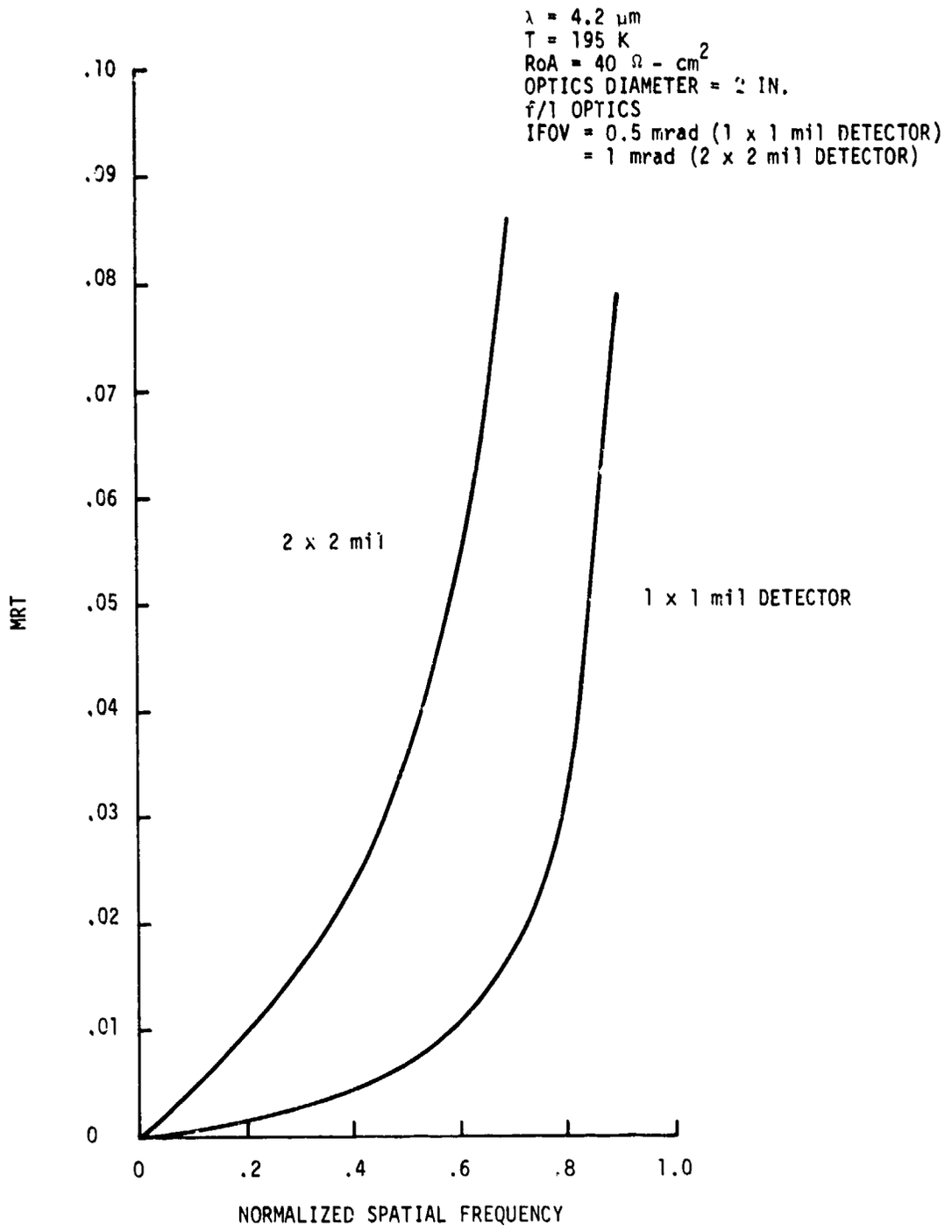

Figure 6-3. MRT vs. Spatial Frequency for Staring Focal Plane

The MRT variation with frame rate is not quite as evident as the NEΔT relationship. For the MRT functional relationship, we start with the equations from staring modeling analysis:

$$MRT = \frac{\pi f_o S}{MTF(f_o)\, q_y} \left(\frac{\Delta y \, \Delta x \, \rho_x \, \rho_y}{\tau_e} \right) \frac{NE\Delta T}{\dot{F}^{1/2}} \tag{6-22}$$

with

$$NE\Delta T = \frac{4F^2}{\pi a \bar{w} D^*} \sqrt{\frac{\Delta f_n}{N}} \tag{6-23}$$

$$q_y = \int_0^\infty 2H_d^2 \, LH_L^2 \, df_y \tag{6-24}$$

$$q_x = \int_0^\infty 2H_d^2 \, WH_w^2 \, df_x \tag{6-25}$$

The only frame rate ($\dot{F}$) dependent terms are

$$MRT(\dot{F}) \propto \frac{NE\Delta T}{\dot{F}^{1/2}} \propto \left(\frac{\Delta f_n}{\dot{F} N} \right)^{1/2} \tag{6-26}$$

because there is no temporal dependence in MTF, M_D, H_L, H_w, H_d, etc. (see Glossary for definition of terms). This is in contrast to the scanning focal plane result, which has temporal terms in MTF and H_D (H'_D, H_{elect}). This will give an $\dot{F}$ dependence to the result if the simple-minded application of the scanned model to the staring application is made.

If we assume a simple integrating input, with an "TDI," N = 1, then

$$\Delta f_n = \frac{\int_o^\infty \overline{I}_{nd}^{\,2} \left(\frac{1}{1 + \omega^2 R^2 C^2} \right) \left(\frac{\sin \pi f \tau}{\pi f \tau} \right) df}{\overline{I}_{nd,o}^{\,2}} \qquad (6\text{-}27)$$

For integration over the whole frame time, $\tau = 1/\dot{F}$, and for reasonably slow frame rates, the detector roll-off term will have no effect. Then

$$\Delta f_n = \int_o^\infty \left(\frac{\sin \frac{\pi f}{\dot{F}}}{\frac{\pi f}{\dot{F}}} \right) df = 2\dot{F} \qquad (6\text{-}28)$$

and Equation (6-26) becomes

$$MRT \propto \left(\frac{\Delta f_n}{\dot{F}} \right)^{1/2} \propto 1 \qquad (6\text{-}29)$$

That is, MRT is independent of frame rate.

It is important to note that this result will not be received if the scanning focal plane model is used, due to temporal effects in MTF and ρ_x.

Figure 6-4 shows the modeled results for the staring array where the model gives the correct $\sqrt{\dot{F}}$ dependence on NEΔT and independence on MRT.

A real performance advantage is gained in operating at lower frame rates in systems where a video display is not used, such as with missile seeker

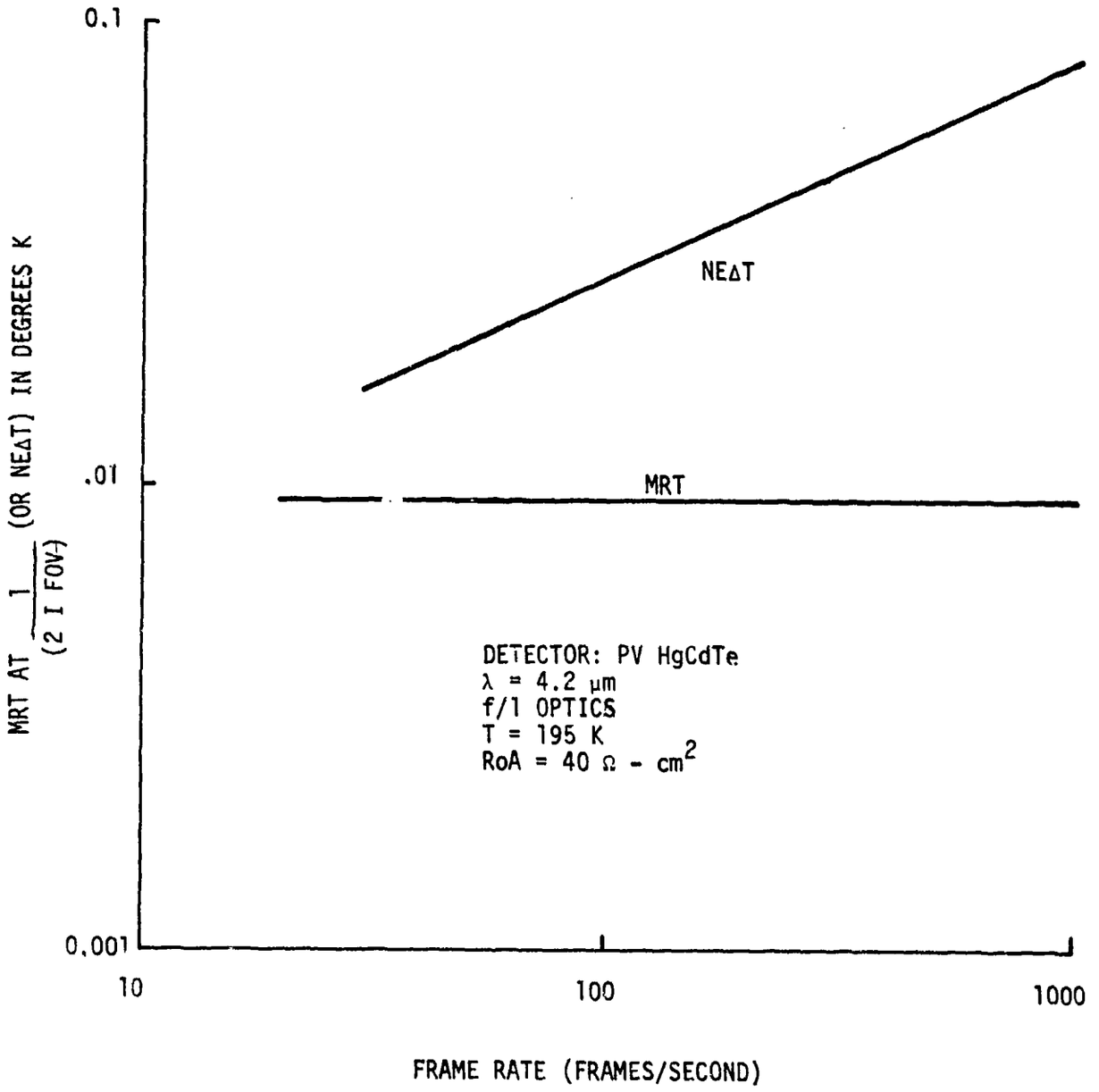

Figure 6-4. MRT and NEΔ T vs. Frame Rate

systems and RPVs. In these applications the data is processed with an on-board analog/digital signal processor, and the $NE\Delta T$ level determines the system sensitivity and dynamic range. In applications where a video display is used (such as with hand-held thermal viewers), the independence of the MRT on the frame rate means that no additional advantage is gained in operating at any particular frame rate. In practice, however, since the same focal plane design could be used in both these types of applications, it is advantageous to develop focal plane structures in which the low frame rate (30 to 60 fps) can be achieved on the focal plane.

GLOSSARY OF TERMS FOR PERFORMANCE MODELING

c	optics blur circle $((mr)^2)$
b	display blur circle $((mr)^2)$
ℓ	focal length (cm)
F	optics f/#
a	detector size (assumed square)
No	system optics transmission
S(f)	noise spectral density
Δfn	noise equivalent bandwidth
fd	normalization frequency for D*, S(f) (Hz)
	threshold S/N for MRT (=2.25 for NVL model)
fo	bar pattern frequency (cycles/mr)
τ_e	eye integration time (= 0.2 sec for NVL model)
F	frame rate (sec^{-1})
L	bar pattern length $(= \frac{7}{2fo})$
W	bar pattern width $(= \frac{1}{2\ fo})$
H	transfer functions:

$H_D =$	$\sin(\pi fx/2fd)/(\pi fx/2fd)$	detector
$H_w =$	$\sin(\pi fx/2fo)/(\pi fx/2fo)$	bar width
$H_L =$	$\sin(7\pi fx/2fo)/(7\pi fx/2fo)$	bar length
$H_d =$	$\exp-(bfx^2+bfy^2)$	display
$H_{optd} =$	$\frac{2}{\pi}[\cos^{-1}A - A(1-A^2)^{\frac{1}{2}}]$, $A \equiv \frac{\lambda F fo}{\ell}$	
$H_{optb} =$	$\exp-(cfx^2 + cfy^2)$	
$H_{elect} =$	electronics bandpass (at CCD input)	

α	Noise correlation time (inverse)

$D^*_{fd}(\lambda p)$	D* at frequency fd and peak wavelength λp
f_ℓ	lower frequency system bandpass ($\approx \dot{F}$)
f*	noise correlation frequency
f_c	"TDI" sampling frequency
τ	fill and spill time $\leq \frac{1}{N\dot{F}} = \frac{1}{f_c}$
R	detector (open circuit) resistance
C	detector (plus parasitic) capacitance
I_s	detector saturation current
I_B	background current ($= qn\phi_B A_D/(4F^2 + 1)$)
$e^2_{1/f}$	detector 1/f noise voltage
C_{RW}	CCD fill and spill well capacitance
MTF(fo)	H_D(fo) H_{opt_d} (fo) H_{opt_b} (fo)

APPENDIX A

MULTIPLE SAMPLE INJECTION INPUT

APPENDIX A

MULTIPLE SAMPLE INJECTION (MSI) INPUT

Honeywell's approach to the detector/CCD electrical coupling for non-BLIP staring focal planes is the Multiple Sample Injection (MSI) circuit. This circuit, invented and demonstrated by Honeywell, has been shown to meet the requirements of

- Low input referred noise, such that a near-unity noise figure can be achieved when operating with TE-cooled detectors.
- Background suppression levels suitable for 30-60 frame-per-second operation.
- Simple structure which requires no detector preamplification, consists of basically one source diffusion and four gates, and can be fabricated in structures as small as 1 x 1 mil.

Figure A-1 is a diagram of the MSI input circuit. The basic concept behind this coupling circuit is that the detector signal level is sampled with respect to the reference gate many times during the frame period. During each of the samples the detector signal (plus noise) levels are summed together into a storage well, V.

The input noise is made up of the detector noise and the CCD input noise which, for this voltage sampling technique, is dominated by the kT/C component at the input gate, of capacitance C. The integrated detector

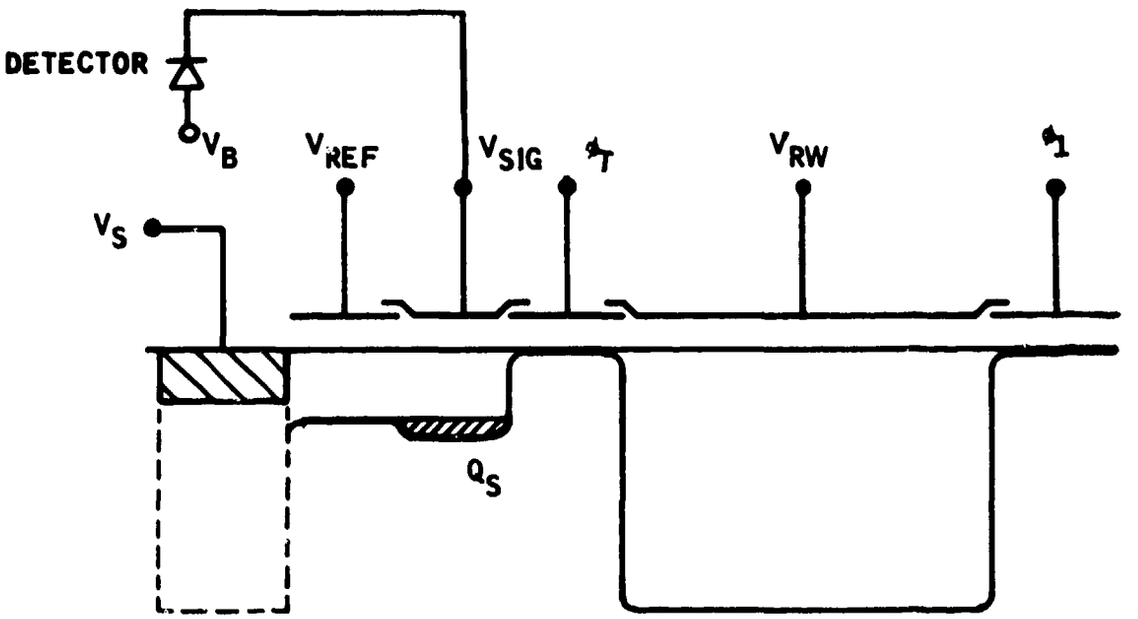

Figure A-1. MSI Input Circuit Diagram

signal is proportional to N, the number of samples, whereas the kT/C noise increases as $N^{1/2}$. Thus the signal-to-noise ratio increases as $N^{1/2}$ until the detector noise component predominates for large N. At this sample rate the input circuit does not degrade detector D*.

This input signal circuit has many unique features which make its structure ideal for interfacing the TE-cooled detector to the CCD electronics. These features include

- Simple configuration - few gates (therefore higher fabrication yields)
- Wide detector bandwidth

- Multiple sampling operation yields large signal gain (and improved S/N ratio)
- Excellent performance (noise figure ≃ 1) at low frame rates (30 fps)
- Innate antiblooming control
- Can be implemented with automatic, self adjusting background suppression

The MSI input is basically a voltage sampling fill and spill circuit.

The fill and spill operation is achieved by pulsing V_s (Figure A-1) to substrate potential for a short period of time followed by its return to a strong-on level (≈ 10 volts). Figure A-2 shows the circuit clocking diagram. This fill and spill operation leaves a small packet of charge, Q_s, beneath the V_{sig} gate:

$$Q_s/C = (V_B + V_{Det} - V_{Tsig} - V_{ref} - V_{Tref})$$

where

V_B = detector substrate bias

V_{Det} = detector open circuit voltage

V_{Tsig} = threshold voltage of V_{sig} gate

V_{ref} = applied reference gate voltage

V_{Tref} = threshold voltage of V_{ref} gate

C = capacitance of the signal gate

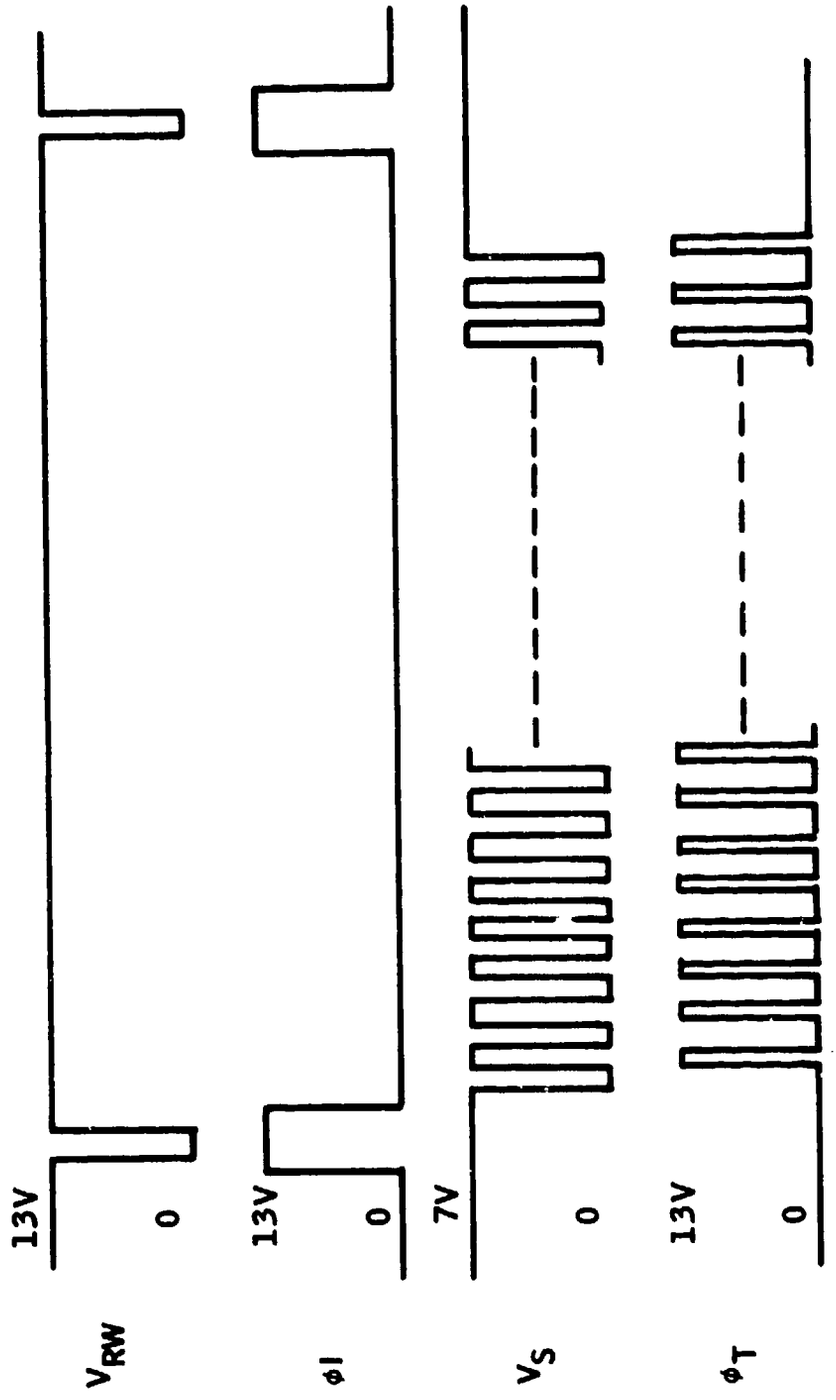

Figure A-2. MSI Clocking Diagram

The expression for V_{Det} can be obtained from the standard diode equation:

$$I = I_{SAT} [1 - \exp (eV/kT)] + I_{\phi} + I_{sig}$$

where I_{ϕ} is the background current and I_{sig} is the signal current.

Since the detector is operating open circuit I = 0, and V_{Det} is given by

$$V_{Det} = \frac{kT}{e} \ln \frac{I_{SAT} + I_{\phi} + I_{sig}}{I_{SAT}}$$

the magnitude of the sampled signal, Q_s, is thus proportional to the natural log of the signal current, which is approximately linear for small signal levels.

Following the fill and spill operation, the Q_s charge packet is transferred to the storage gate V_{RW} by turning on ϕ_T. Since the magnitude of Q_s is small compared with the charge storage capacity of V_{RW}, this sampling and storage operation can occur many times before V_{RW} is saturated.

The V_{RW} gate stays on for nearly the full frame time and is gated to zero at the end of the frame time to transfer the summed charge packet into the readout shift register. The maximum sampling frequency is limited by the detector open circuit bandwidth (typically ≈ 100 to 500 kHz). When this condition is observed, the signal charges add linearly while the uncorrelated noise terms from each sample are added in quadrature ($\sqrt{N}$). Thus the improved S/N of the final charge packet has effectively reduced the input referred noise of the CCD input by the square root of the number N of independent samples.

Figure A-3 is a diagram of the output charge amplitude as a function of the sampling frequency and is shown as related to the detector bandwidth. As indicated, the signal continues to add linearly independent of the sampling frequency, but once the sampling occurs beyond the detector bandpass the correlated noise begins adding linearly so that no additional S/N improvement is realized.

MSI INPUT PERFORMANCE CHARACTERISTICS

The performance characteristics of the MSI input circuit were measured using Honeywell's 2178 CCD chip on which the MSI input test circuit was fabricated. The circuit is a 16-stage CCD delay line with two separate MSI input circuits at the input as shown in Figure A-4. The only difference between the two input structures was the ratio of the receiving well area to the detector gate area. Channel A had $A_{RW}/A_W = 22$ while the channel B ratio was 4.4. These different ratio wells were designed into the circuit to measure 1/f noise effects and to verify the input stage gain calculations.

Figure A-5 shows the gate structure for the test circuit. The input has a four-gate input (prior to the shift register) compared with the three-gate input described previously. This additional gate was placed in the circuit to determine the performance characteristics when differencing between two level-one polysilicon gates and when differencing between poly-one and poly-two level gates.

Between the detector terminals and the CCD, there is no filtering to band-limit the process. However, coupling the detector's stored charge into the CCD well is inherently a band-limited process.

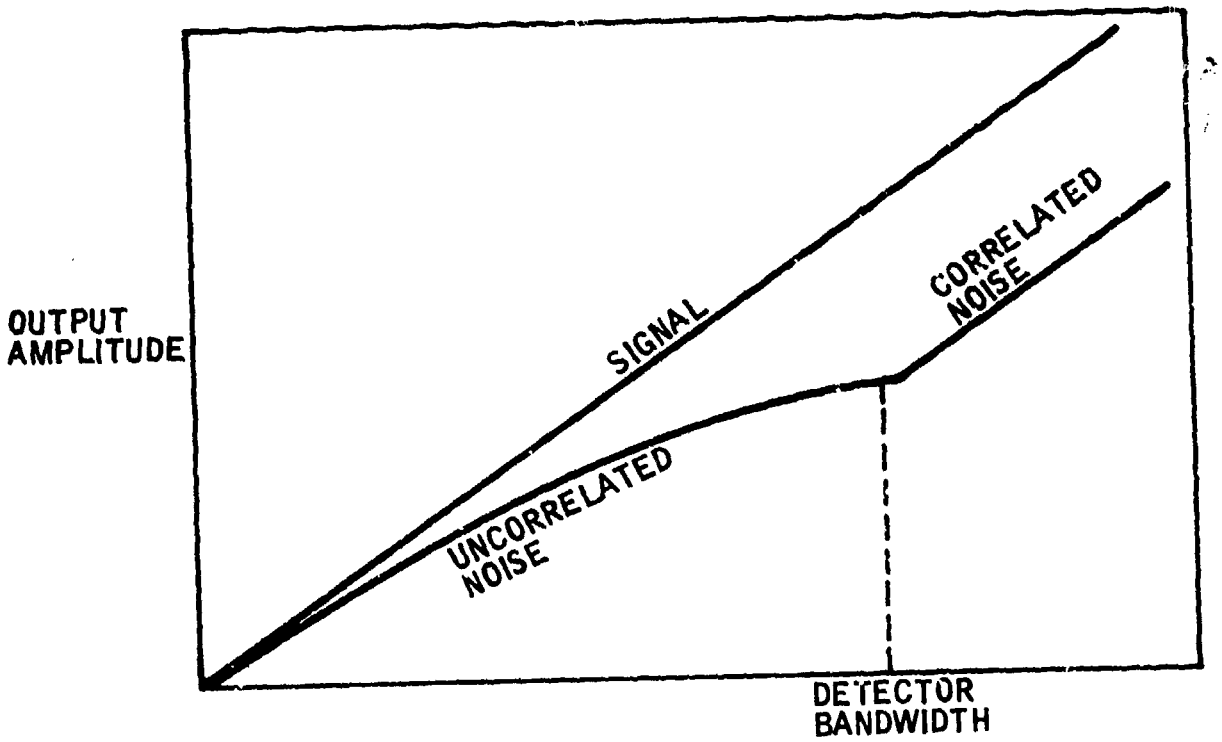

Figure A-3. Output Amplitude vs. Sampling Frequency Indicating Regions of Correlated and Uncorrelated Noise Contributions

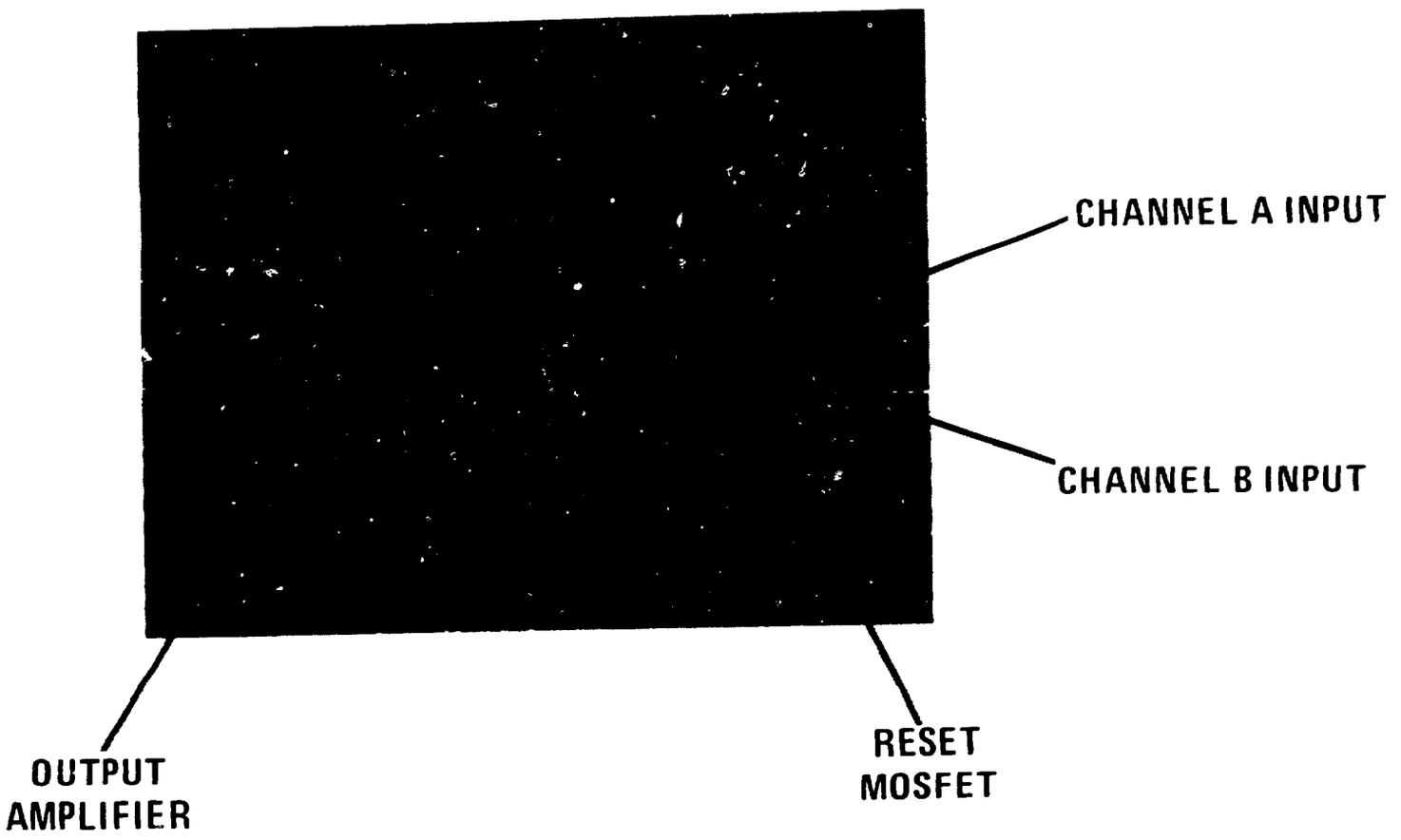

Figure A-4. MSI Test Circuit on the Honeywell 2178 CCD Chip

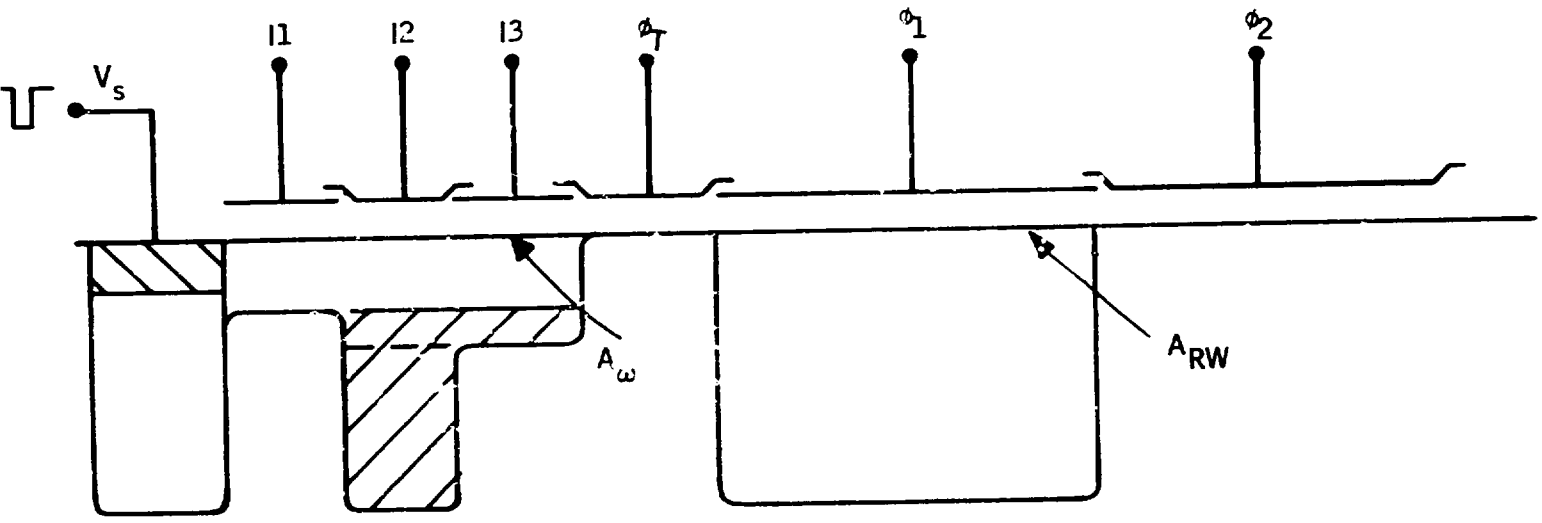

Figure A-5. MSI Input Test Cell on 2178 CCD Chip

Input Referred Noise

The input referred noise levels can easily be calculated by the following expression, which relates the input well capacitance and the total number of input samples, N, to an input referred noise voltage V_{in}:

$$V_{in} C_w N = \sqrt{NkTC} \qquad (A-1)$$

The expression on the right is the summed charges in the storage well after N samples when the left-hand expression refers to the input charge level. Rewriting Equation (A-1) gives

$$V_{in}^2 \text{ (input referred noise)} = \frac{kT}{NC\Delta f} \qquad (A-2)$$

where Δf = CCD output bandwidth.

From this equation it is seen that the input referred noise V_{in} improves as $\sqrt{1/N}$ as expected.

Figure A-6 shows a plot of the input referred noise magnitudes vs. the number of input samples, N, for the 1 x 1 mil and 2 x 2 mil cell designs. This is consistent with the results of the noise figure calculations which showed that an input sampling frequency on the order of 300 kHz is required to achieve a near-unity noise figure. Figure A-6 shows that, to approach the detector noise levels shown, the total number of samples taken during the frame time is N ≈ 3000 for the 1 x 1 mil cell design and N = 4000 for the 2 x 2 mil cell design for a 30 fps frame rate.

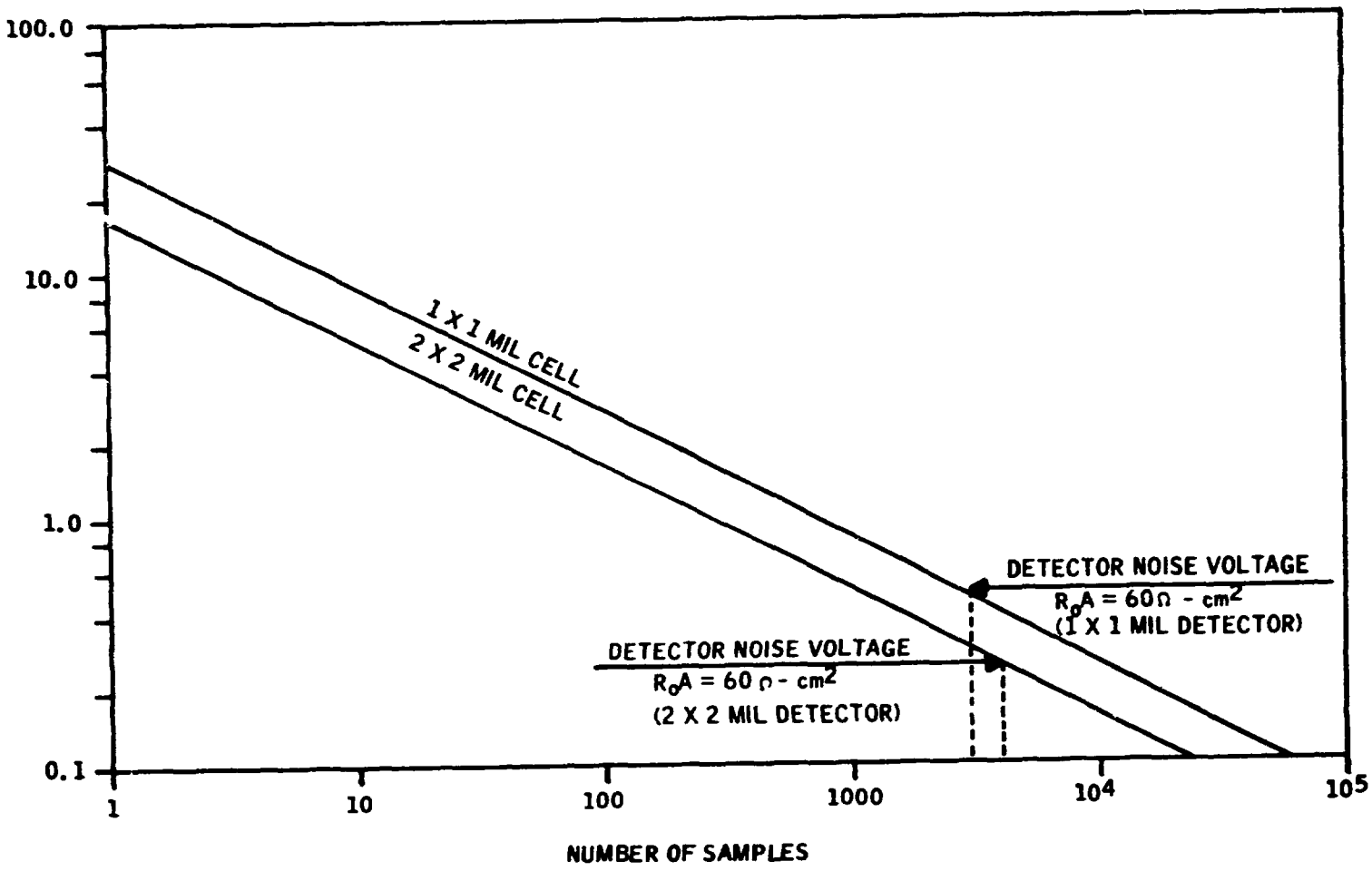

Figure A-6. MSI Input Referred Noise vs. Number of Input Samples

The input noise figure is defined as

$$N.F. = \left[\frac{(\text{Detector noise})^2 + (\text{CCD input noise})^2}{(\text{Detector noise})^2} \right]^{1/2}$$

The noise voltage of a PV detector is simply given by

$$\overline{V_D}^2 = 4kTR\,\Delta f + e_{1/f}^2 \qquad \text{(A-3)}$$

where

R_o = detector zero bias dynamic resistance

$e_{1/f}$ = 1/f noise contribution (= 0 for zero biased detectors)

The CCD input noise for this voltage sampling technique was given in Equation (A-2) as

$$V_{CCD}^2 = \frac{kT}{C_w} \qquad \text{(A-4)}$$

where C_w = CCD well capacitance. The input noise figure can now be written as

$$NF^2 = \frac{4KTR\Delta f + \frac{KT}{C_v}}{4KTR\Delta f} \qquad \text{(A-5)}$$

For proper operation we set the sampling rate $\dot{N} = \Delta f$. Equation (A-3) then becomes

$$NF^2 = 1 + \frac{A_D}{4R_o A_D C_w \dot{N}} \qquad \text{(A-6)}$$

where

A_D = detector area

R_o = detector zero bias resistance

Figures A-7 and A-8 show a plot of the input noise figure for the CCD input design for a 2 x 2 mil cell and a 1 x 1 mil cell, respectively, as a function of the number of input samples and the input well capacitance, C_w. The conditions for these calculations are given in Table A-1.

TABLE A-1. CONDITIONS FOR NOISE FIGURE CALCULATIONS

R_oA	= 60Ω - cm^2
T	= 195 K
A_D	= 2 x 2 mils = 2.6 x 10^{-5} cm^2
F	= 30 frames per second
$\dot{N}$	= 3.3 x 10^5 samples per second

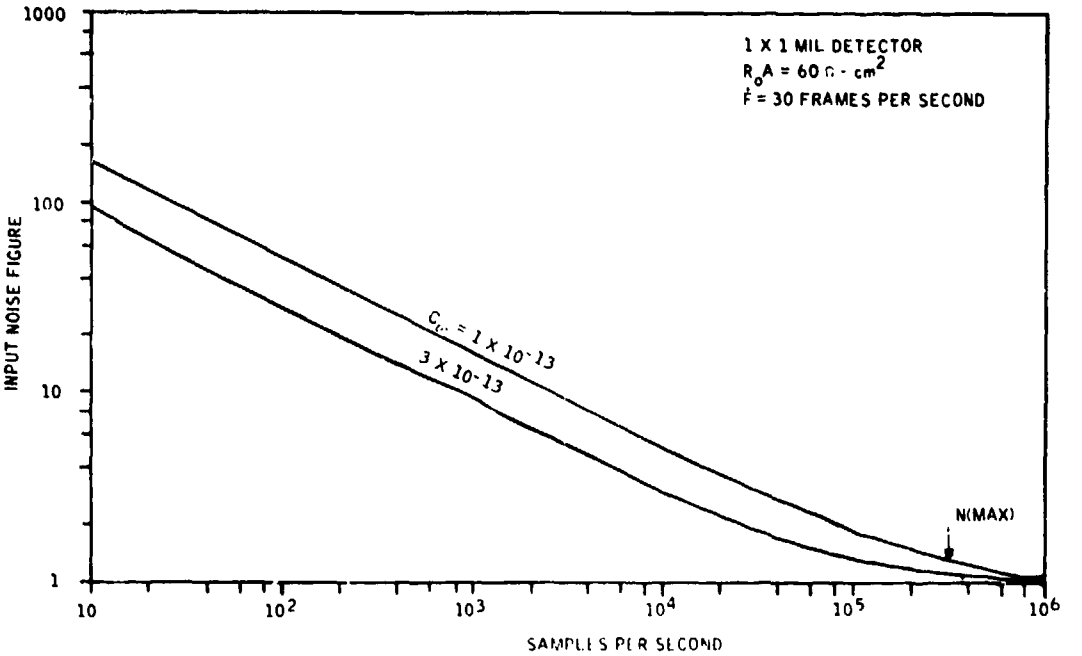

Figure A-7. Input Noise Figure vs. Sample Rate for 1 x 1 mil Detector Array

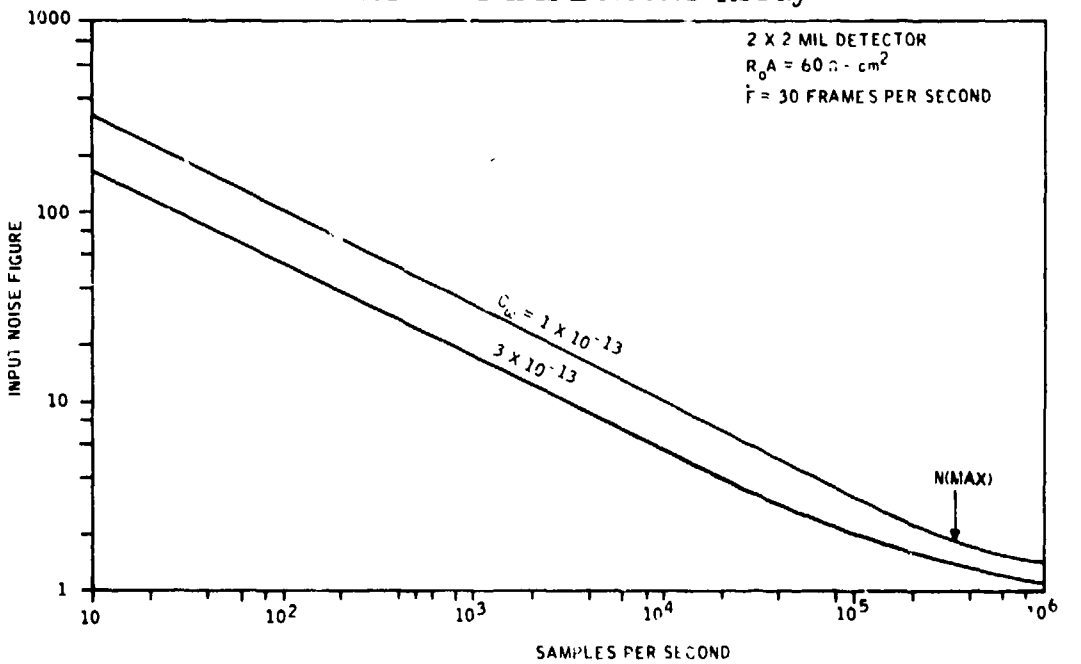

Figure A-8. MSI Input Noise Figure vs. TDI Sample Rate for 2 x 2 mil Detector Array

The values for $\dot{N}_{max}$ are determined by considering that the detector sampling frequency should not extend beyond the detector bandpass frequency and therefore

$$\dot{N}_{max} = \left(R_o A_D \times \frac{C_o}{A_o}\right)^{-1} = (60 \times 5 \times 10^{-8})^{-1}$$

$$= 3.3 \times 10^{5} \text{ samples per second}$$

The well capacities for the 1 x 1 and 2 x 2 mil cells described earlier are shown in Table A-2.

TABLE A-2. RECEIVING WELL CAPACITANCE

	1 x 1 mil cell	2 x 2 mil cell
A_w	1.8×10^{-6} cm^2	5×10^{-6} cm^2
C_w	1×10^{-13} Farads	3×10^{-13} Farads

From Figures A-7 and A-8 it can be seen that, for the cases considered, a near-unity noise figure is achieved for either the 1 x 1 or 2 x 2 mil cell designs if the number of input samples is near the detector bandwidth of 330 kHz. The dominant term in the noise figure expression of Equation (A-6) is the detector $R_o A$ product and the input well capacitance C_w. Figure A-9 shows a plot of the input noise figure vs. RA product for the 2 x 2 mil cell with $\dot{N} = \dot{N}_{max}$.

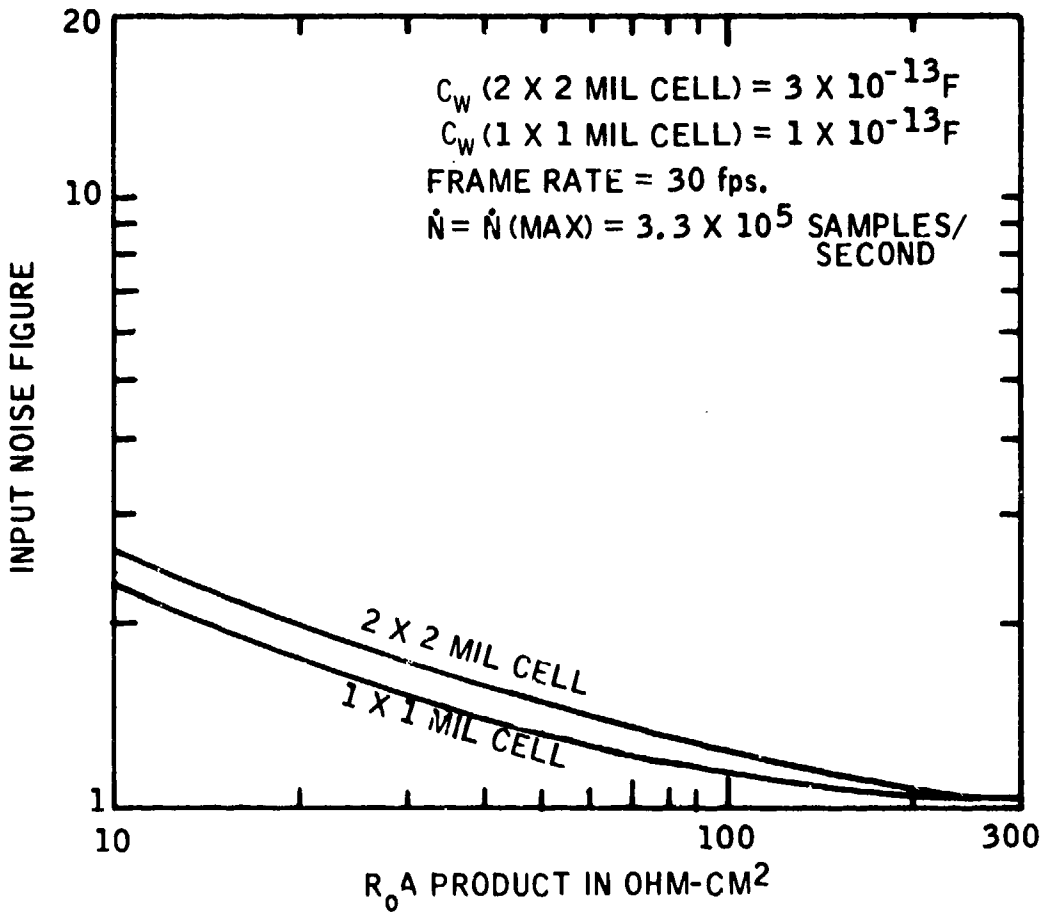

Figure A-9. Input Noise Figure vs. R_oA Product for $\dot{N} = \dot{N}_{max}$

Nonuniformity Effects

In designing the MSI input circuit, consideration must be made regarding both the detector responsivity variations and the CCD threshold variations to insure that these nonuniformities do not saturate the CCD wells. The detector responsivity variations are due to quantum efficiency and R_oA product variations.

Honeywell's NMOS CCD processing line has been able to consistently fabricate CCD circuits with state-of-the-art threshold voltage variations. As an example, devices fabricated and measured on NVL contract DAAK70-77-C-0160 have shown the 1σ threshold variation levels to be about ±2 mV on chips whose input gates spread over a 260 mil distance. Figure A-10 shows a histogram of the distribution of the CCD threshold variations for a sample of 512 input gates measured on 32 different CCD chips under the mentioned contract.

The MSI input circuit effectively multiplies the input voltage variation by the number of samples. For the case where the ΔV_T = 6mV (2σ value) and the number of samples required to achieve a near-unity input noise figure is N = 4000, the integrated output signal variations = $N\Delta V_T$ = 24 volts. With a maximum charge packet amplitude in the CCD well of about 6 volts, we can accomodate the $N\Delta V_T$ variation by reducing the input stage gain which is determined by the ratio of the receiving well capacitance and the detector input gate capacitance. For this example the receiving well area should be designed to be at least four times the area of the input gate.

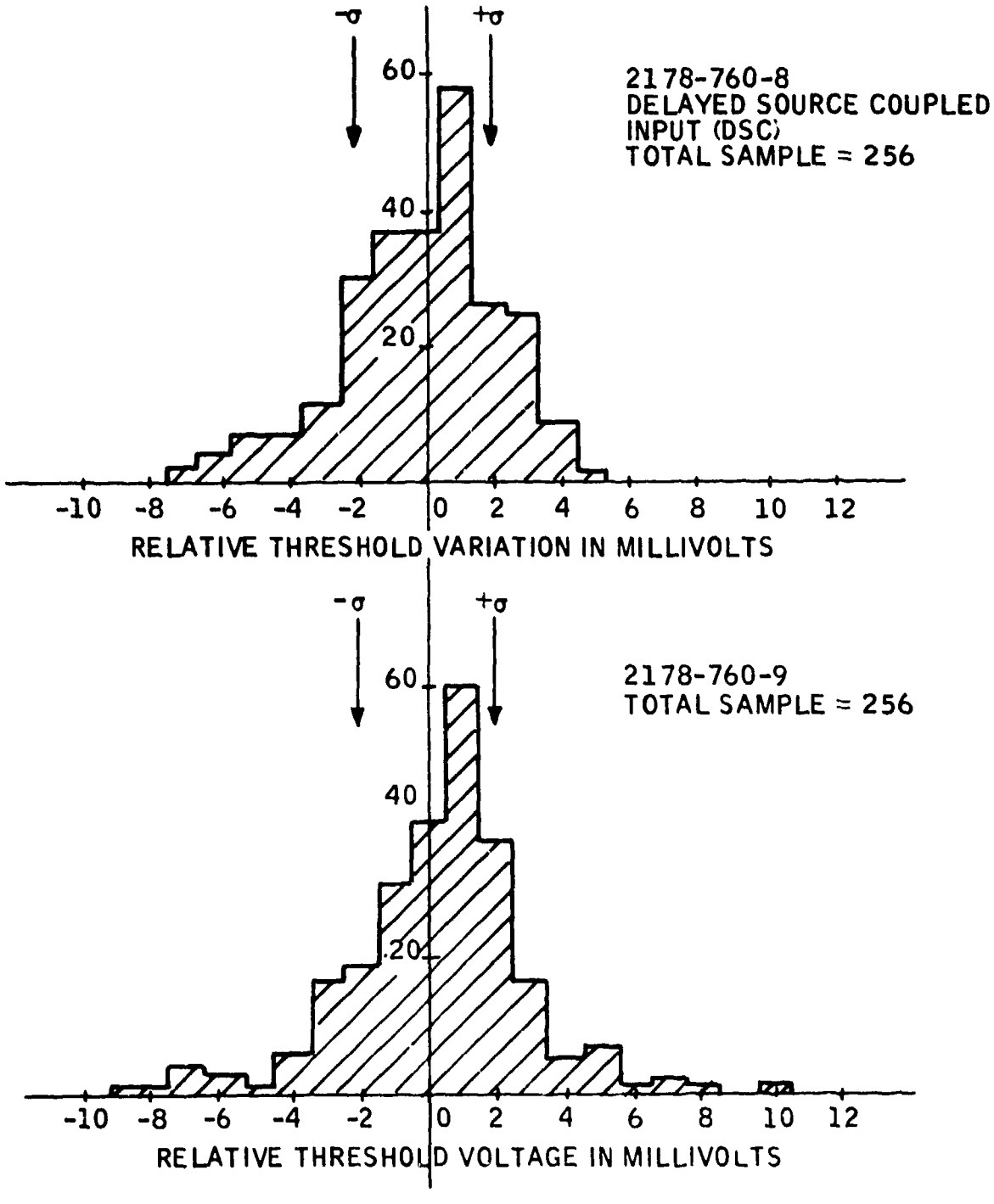

Figure A-10. Input Gate Threshold Voltage Distribution Measured on 32 Different CCD Chips

Figure A-11 shows the ratio of the receiving and input gate areas as a function of the number of samples N for different ΔV values. The expression for the relative areas is given by

$$\frac{A_{RW}}{A_w} = \frac{N \Delta V}{V_{max}}$$

where V_{max} = maximum charge packet magnitude

From Figure A-6 the N value needed to reduce the CCD input referred noise to the detector noise level was N = 4000. The gate ratio design can now be determined from the curve in Figure A-11. For N = 5000 samples and ΔV_T between 4 and 8 mV, the ratio of A_{rw} to A_w should be $A_{rw}/A_w \cong 4$.

Dynamic Range

The dynamic range performance can be determined by calculating the maximum signal charge and rms noise charges in the V_{RW} well. We will assume that the maximum signal charge is one-half of the total V_{RW} well capacity since the circuit has been designed such that the CCD threshold nonuniformities will be accommodated in the other one-half of the well capacity as described earlier. Thus for Q_{sig} (max) we have

$$Q_{sig}\,(\text{max}) = \frac{C_{RW}}{2} \times V_{RW} = 9 \times 10^{-13} \text{ Coul (2 x 2 mil cell)}$$

$$= 3 \times 10^{-13} \text{ Coul (1 x 1 mil cell)}$$

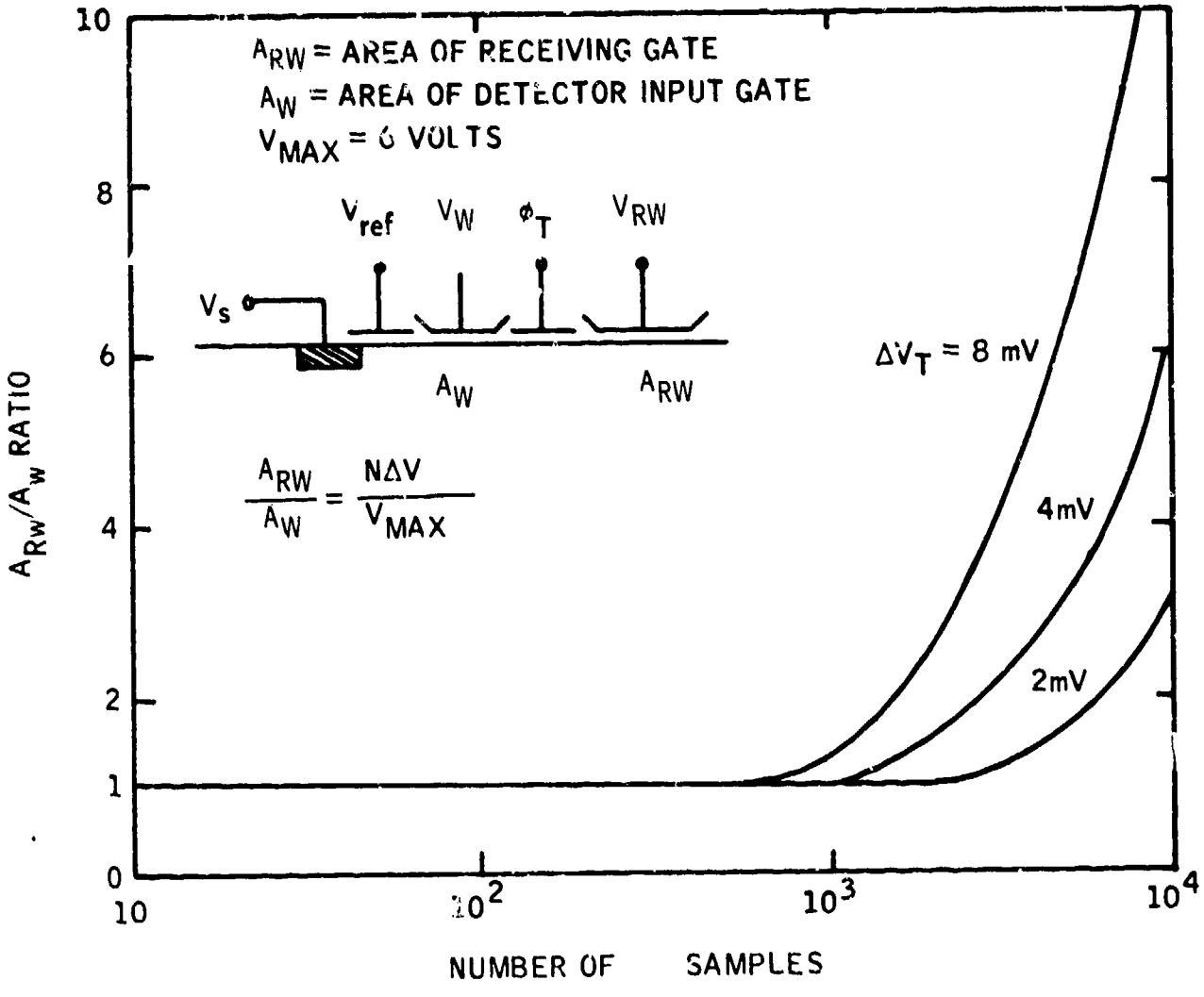

Figure A-11. Receiving Gate Area to Input Gate Area Ratio as Required to Insure that Threshold Variation Effects are Accommodated by the CCD Output Well (as a Function of the Number of Input Samples)

[Recall: $C_{RW}(2 \times 2 \text{ mil}) = 3 \times 10^{-13}$ Coul
and: $C_{RW}(1 \times 1 \text{ mil}) = 1 \times 10^{-13}$ Coul]

The total noise charge in V_{PW} is given by the input kTC noise which is rms added by the number of samples N and is given by

$$Q_{noise} = (NkTC_w)^{1/2} \left(\frac{C_w}{C_{RW}}\right)^{1/2} \qquad \text{(A-8)}$$

where (C_w/C_{RW}) is the input stage gain determined by the relative gate areas of V_{sig} and V_{RW} electrodes.

As mentioned earlier, we have selected $C_{RW} = 4\,C_W$. Thus we have

$$\begin{aligned} Q_{noise} &= 1/2\,(NkTC_W)^{1/2} \\ &= 5 \times 10^{-16} \text{ Coul (2 x 2 mil cell)} \\ &= 2.6 \times 10^{-16} \text{ Coul (1 x 1 mil cell)} \end{aligned}$$

The dynamic range values calculated by taking into account the offset nonuniformities are shown below in Table A-3.

TABLE A-3. MSI DYNAMIC RANGE PERFORMANCE CHARACTERISTICS

Cell Size	Q_{sig} (max)	Q_{noise}	Dynamic Range
2 x 2 mil	9×10^{-13} Coul	5×10^{-16} Coul	65 dB
1 x 1 mil	3×10^{-13} Coul	2.6×10^{-16} Coul	61 dB

MSI CIRCUIT EVALUATION

The evaluation of this circuit included the following measurements:

- S/N improvement factor
- Input referred noise characteristics
- Threshold nonuniformity effects

S/N Improvement Factor--The input circuit was set up so that:

Gate I1 = Reference voltage level
I2 = Strong on
I3 = Signal gate
ϕT = Transfer gate
$\phi 1$ = Storage gate

The input is a surface channel structure which transitions to the buried channel shift register in the middle of the ϕT electrode.

The input noise level and signals levels were measured as a function of the number of samples. Figure A-12 shows some typical results for frame rate = 1000 fps and a 200 Hz input signal.

The figure shows a linear increase in amplitude with increasing N as expected and the noise increasing at a rate equal to $\sqrt{N}$. Figure A-13 shows both the theoretical S/N improvement factor and the experimental data points. The agreement between the theory and experimental data is excellent and clearly demonstrates the S/N improvement achieved by the MSI input circuit.

Input Referred Noise Measurements--The input referred noise of the MSI test circuit was measured by first measuring the input to output transfer function (V_{out}/V_{in}), and then measuring the output noise spectra and dividing by the transfer function. Figure A-14 shows a plot of the input referred noise as a function of the number of input samples measured out to N = 1000. The noise was measured at f = 100 Hz, while the frame rate was 200 frames per second. (The 16 delay stages following the input circuit limited how low we could go in frame rate at room temperature due to dark current build-up.)

From Figure A-14, it is seen that the theory and experimental data points are in excellent agreement with the theoretical calculations predicted for this device. The lowest input referred noise level is limited by the input gate 1/f noise of the particular device measured. The noise capacitance factor was measured to be C_n = 300 pF/cm^2 for these devices. Improvement of the C_n factor will result in a reduction of the input 1/f noise level and permit operation with near unity noise figures.

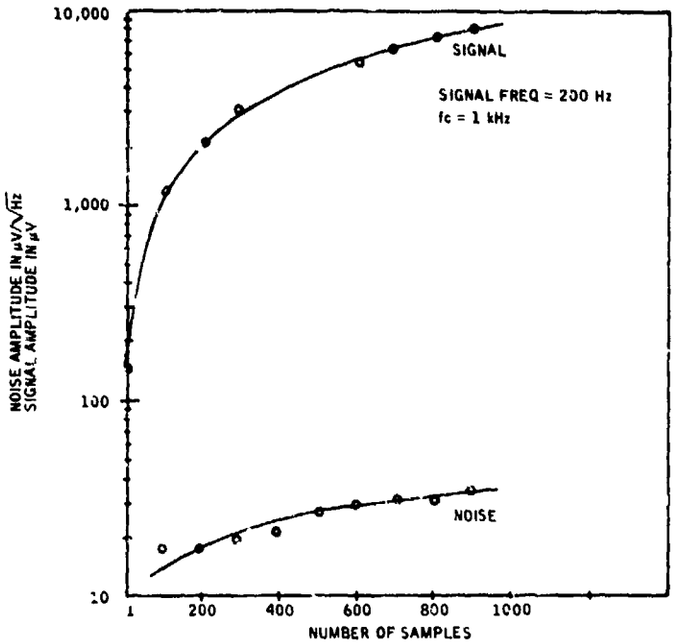

Figure A-12. Experimentally Measured Signal and Noise Characteristics of MSI Input

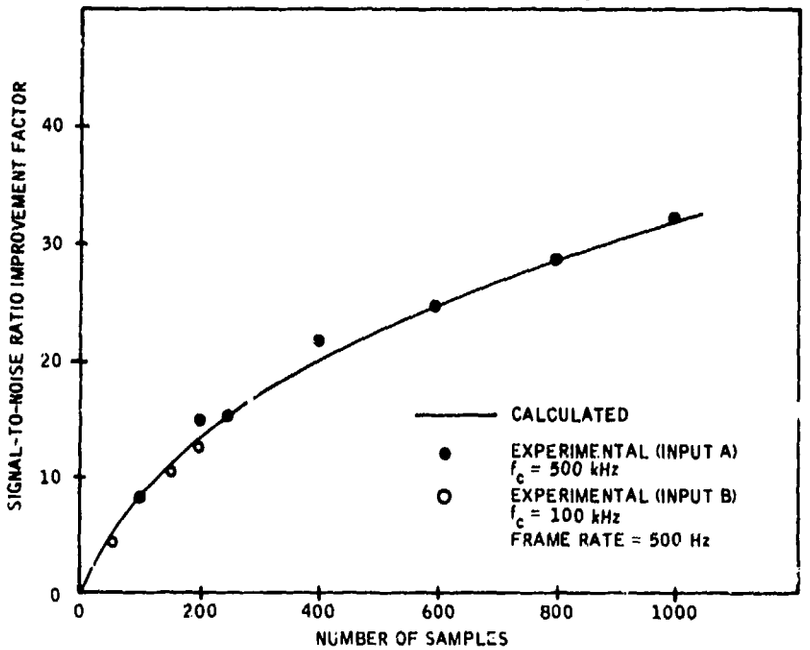

Figure A-13. Experimentally Measured S/N Improvement Factor for MSI Input Circuit

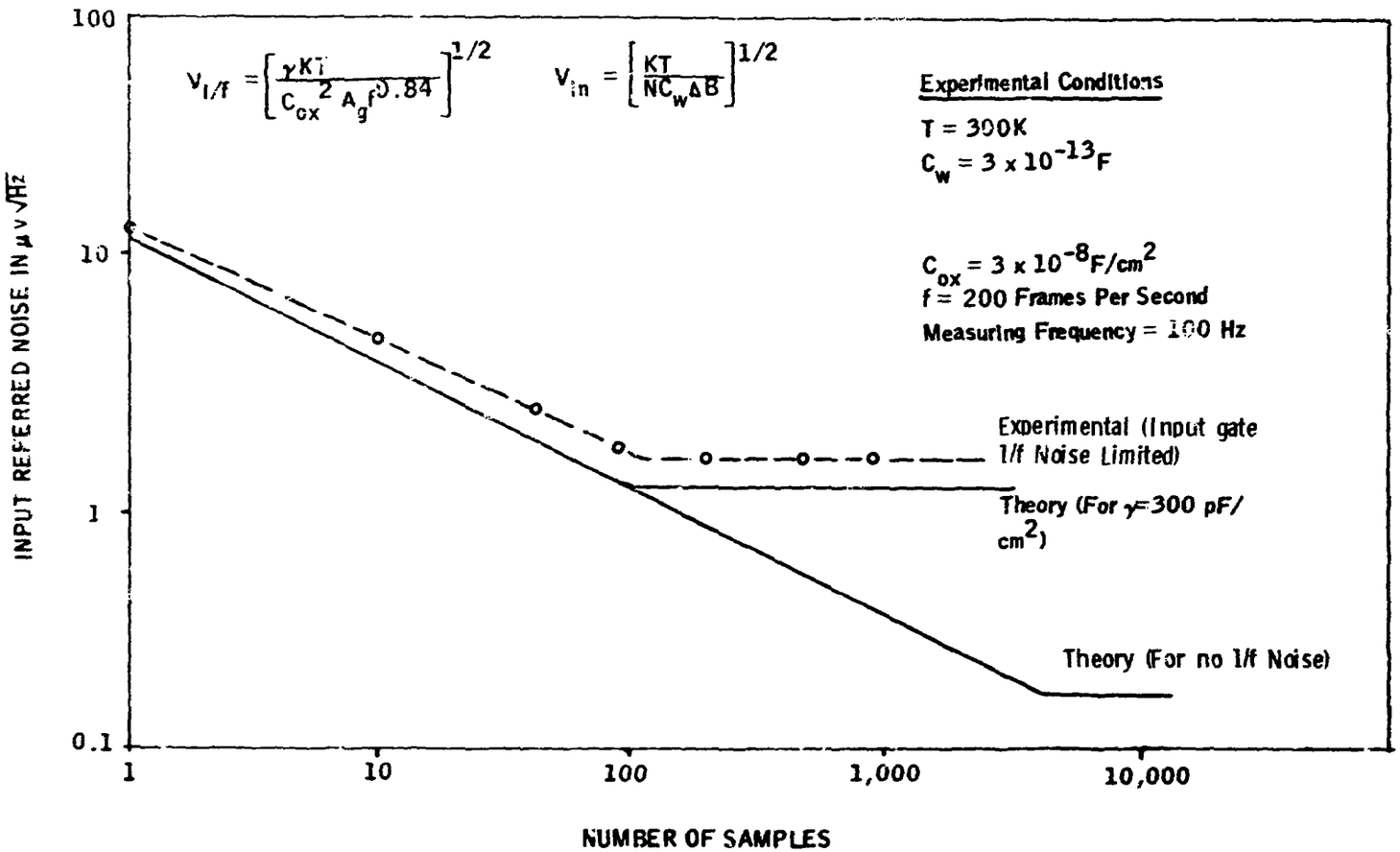

Figure A-14. MCI Input Referred Noise Characteristics Measured on 2178 CCD Test Chip

Threshold Nonuniformity Effects--The effects of threshold nonuniformities were evaluated on the test devices. The input threshold variations can be calculated as shown in Figure A-15. This photo shows the output signal from the MSI test chip with N = 1000 samples for a sine wave input signal. The overall device gain is simply the ratio of the ac output signal to the ac input amplitude. The input threshold variations will give rise to different dc levels at the output and are measured by dividing the dc level differences by the device gain.

Figure A-16 shows the test circuit used to evaluate the effects of differencing the detector signal level and reference voltage when they are on the same polysilicon layer level (i.e., the threshold variation effects will be due to differences between two gates on a poly-one level). The first test devices were set up and a total of 13 different CCD chips were plugged in and evaluated without changing any operating voltages. As shown in the figure the average gain was 8.96 with a 1σ variation of 0.42; the average dc offset level was 0.88 volts with a 1σ variation of only 0.06 volts. This result is especially important since we believe these uniformity characteristics to be both unique and key to successful focal plane performance.

Figure A-17 shows the results of measuring the nonuniformity effects when the reference and signal levels are on different polysilicon gate levels. The ac and dc level variations are somewhat greater than the poly 1 - poly 1 level measurements but are still exceptionally low.

The results show that differencing between gates on the same polysilicon level results in the lowest nonuniformity levels and should be used to ensure optimum device performance.

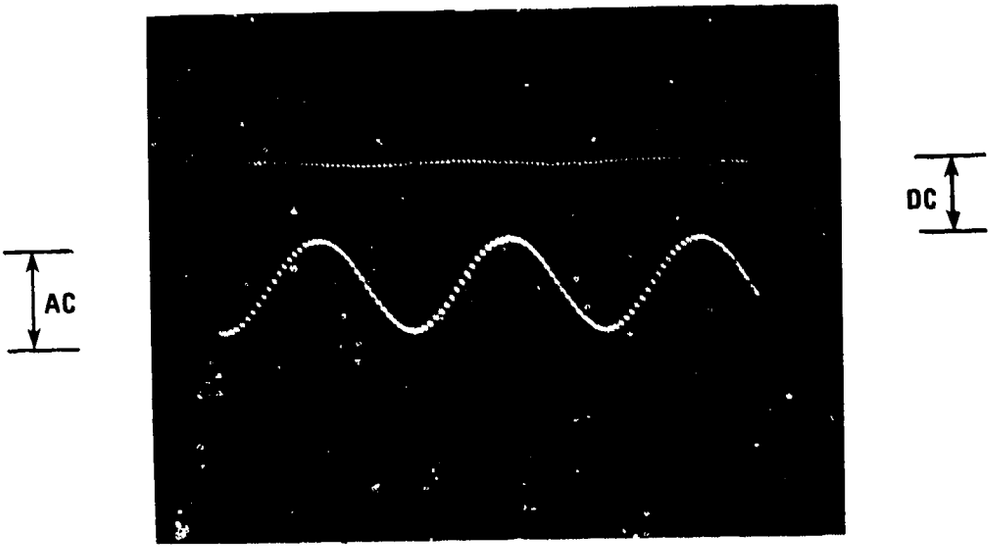

$$\text{GAIN} = \frac{\text{AC OUT}}{\text{AC IN}} \qquad \text{INPUT THRESHOLD VARIATION} = \frac{\triangle \text{DC}}{\text{GAIN}}$$

Figure A-15. MSI Output Waveform for Sine Wave Input and N = 1000 Samples

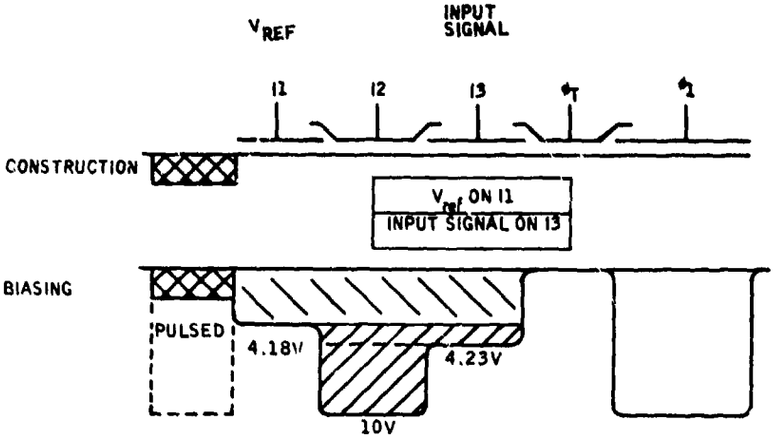

MEASUREMENTS ON 13 CCD CHIPS

INPUT THRESHOLD VARIATION (1-1)	GAIN VARIATION (AC) MEAN VALUE=8.96 V/V	OUTPUT LEVEL VARIATION (DC) MEAN VALUE =0.682 VOLTS
$1\sigma = 4.5$ mV	$1\sigma = 0.42$ V/V	$1\sigma = 0.06$ V

Figure A-16. Nonuniformity Measurements between the Same Polysilicon Levels

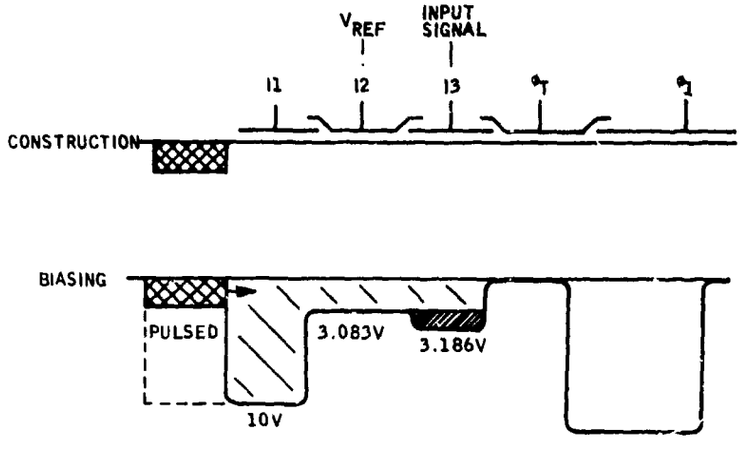

MEASUREMENTS ON 13 CCD CHIPS

INPUT THRESHOLD VARIATION (1-2)	GAIN VARIATION (AC) MEAN VALUE = 5.42 V/V	OUTPUT LEVEL VARIATION (DC) MEAN VALUE = 0.585V
$1\sigma = 12$ mV	$1\sigma = 0.44$ V/V	$1\sigma = 0.092$V

Figure A-17. Nonuniformity Measurements between Different Polysilicon Levels

APPENDIX B

SPECTRAL NOISE DENSITY $S(f_x, f_y)$ DERIVATION

APPENDIX B

SPECTRAL NOISE DENSITY $S(f_x, f_y)$ DERIVATION

There are two equivalent methods to derive $S(f_x, f_y)$ from $n(x, y)$. The first approach makes use of the noise spatial autocorrelation function to give S:

$$S(f_x, f_y) = F.T.(C(\gamma, \mu)) \tag{B-1}$$

where F.T. stands for the fourier transform operation, and $C(\gamma, \mu)$ is the autocorrelation function for the noise, defined by

$$C(\gamma, \mu) = \iint n(x, y)\, n(x-\gamma,\ y-\mu)\,dx\,dy \tag{B-2}$$

Inserting the value for n from Equation (6-3) into this expression gives

$$C(\gamma, \mu) = \iint \sum_{i,j,k,\ell} n_{ij} n_{k\ell} h(x-x_i) h(x-x_k-\gamma) g(y-y_j) g(y-y_\ell-\mu)\,dx\,dy \tag{B-3}$$

Using the uncorrelated nature of the noise, we get

$$C(\gamma, \mu) = \iint \sum_{i,j} n_{ij}^2\, h(x-x_i) h(x-x_i-\gamma) g(y-y_j) g(y-y_j-\mu)\,dx\,dy \tag{B-4}$$

Making use of the spatial invariance of h and g,

$$h(x-x_i)h(x-x_i-\gamma) = h(x-x_k)h(x-x_k-\gamma) \text{ for all } i,\ k$$

and noting that

$$n_{ij}^2 = n^2 \text{ for all } i,\ j$$

we have

$$C(\gamma,\mu) = N_x N_y n^2 \iint h(x-x_i)h(x-x_i-\gamma)g(y-y_j)g(y-y_i-\mu)dxdy \qquad (B-5)$$

with N_x, N_y equal to the number of detectors in the x and y directions. Inserting this expression into Equation (B-1), and defining $H(f_x) =$ F.T. (h(x)), we have finally

$$S(f_x,f_y) = N_x N_y n^2 H^2(f_x) G^2(f_y) \qquad (B-6)$$

The alternative derivation of $S(f_x,f_y)$ proceeds from a theorem of fourier analysis which states

$$S(f_x,f_y) = \text{F.T.}(n(x,y)) \cdot \text{F.T.}^*(n(x,y)) \qquad (B-7)$$

The fourier transform of n(x, y) is given by

$$\text{F.T.}(n(x,y)) = \iint \sum_{i,j} n_{ij}\, h(x-x_i)g(y-y_j)e^{j(F_x x + f_y y)}\, dxdy \qquad (B-8)$$

Using the translation property of the fourier transform, we have

$$F.T.(n(x,y)) = \sum_{i,j} n_{ij}\, H(f_x)\, G(f_y) e^{jf_x x_i}\, e^{jf_y y_j} \tag{B-9}$$

Then inserting this expression into Equation (C-7), we have

$$S(f_x, f_y) = \sum_{i,j,k,\ell} n_{ij} n_{k\ell}\, H^2(f_x)\, G^2(f_y) e^{jf_x(x_i - x_k)}\, e^{jf_y(y_j - y_\ell)} \tag{B-10}$$

Using the uncorrelated nature of n_{ij}, the sum is reduced to

$$S(f_x, f_y) = N_x N_y\, n^2\, H^2(f_x)\, G_z^2(f_y) \tag{B-11}$$

This is the same expression as derived from Equation (B-6).

Now the normalization factor for S must be determined to relate the noise spectrum to NEΔT. To do this, we draw on another theorem from fourier analysis which states

$$\iint n^2(x,y)\, d_x d_y = \iint S(f_x, f_y)\, df_x df_y \tag{B-12}$$

Replacing the first integral by a double sum, we have

$$n^2\, \Delta x \Delta y\, N_x N_y = \iint S(f_x, f_y)\, df_x df_y \tag{B-13}$$

where n^2 is the noise from one detector. Then the appropriate expression for n^2 for one detector is

$$n^2 = \iint S_1(f_x, f_y) df_x df_y \tag{B-14}$$

where

$$S_1(f_x, f_y) = \frac{S(f_x, f_y)}{\Delta x \Delta y \; N_x N_y} \tag{B-15}$$

or

$$S_1(f_x, f_y) = \frac{n^2 H^2(f_x)\, G^2(f_y)}{\Delta x \Delta y} \tag{B-16}$$

n^2 is simply the total noise from one detector, and in terms of $NE\Delta T$ and display characteristics it is given by

$$n^2 = (NE\Delta T)^2 (k')^2 \tag{B-17}$$

We finally have

$$S(f_x, f_y) = \frac{(k')^2 (NE\Delta T)^2 H^2(f_x)\, G^2(f_y)}{\Delta x \Delta y} \tag{B-18}$$

APPENDIX C

STARING FOCAL PLANE MODELING EXAMPLE

APPENDIX C

STARING FOCAL PLANE MODELING EXAMPLE

The computer modeling process consists of running the NVL program[1] twice--using the results from the first run as inputs into the second run which finally yield the terms necessary to calculate the MRT values. By modifying selected inputs between the two runs and mathematically relating various results, the MRT and NEΔT for a given system can be determined. The total modeling process can be described as two separate steps. The steps are

1. Data selection and preparation
2. Determining the MRT

DATA SELECTION AND PREPARATION

The obvious first step is to select the detector system to be modeled. After this is accomplished the deck setup is almost complete for pass 1. The only variation for pass 1 from the standard NVL program deck is to change the number of detectors in series (DISC) on the DETR data card to 1.

The data setup for run 2 is more complicated. For this run the number of detectors in parallel is set to 1 and number of detectors in series is set to N where N is the detector bandwidth divided by the frame rate. Furthermore the normalized noise power spectrum, NPSP data card, must be

[1] J. A. Ratches et al., "Night Vision Laboratory Static Performance Model for Thermal Viewing Systems", NTIS, April 1975.

generated from the following equation:*

$$S(f) = \frac{4R^2q\left(I_B + \frac{kTA}{qR_oA}\right)\left|\frac{\sin(\pi f/NF^*)}{\pi f/NF^*}\right|^2\left(\frac{1}{1+(2\pi fR_oA\,(C/A))^2}\right)}{4R^2q\left(I_B + \frac{kTA}{qR_oA}\right)} \qquad \text{(C-1)}$$

where the parameters have the same definitions as previously described. The above equation is solved for S as a function of frequency (f). The frequencies used are the same that were specified on the NPSF data card used for run 1. The results are normalized at the frequency (F_o) on the DETR data card. If the results must be normalized, i.e., $S(F_o) \neq 1$, then the peak measured S star on the DETR data card must be degraded by the value of $S(F_o)$. It should be pointed out that the normalization process is not often required.

DETERMINING THE MRT

The data deck is now ready to be submitted to the computer for execution. It is suggested that both data decks should be run as one job. This facilitates the data reduction.

---

*Equation (D-1) is the S(f) expression to be used when modeling the MSI input circuit.

Once the computer runs have been performed, the detector MRT can be determined. The MRT is given by

$$MRT_{DET} = MRT_{RUN\ 2} \frac{NE\Delta T_{RUN\ 2}}{NE\Delta T_{RUN\ 1}} (2\Delta f T_d)^{1/2}$$

where

$$2\Delta f T_d = 2\left(\frac{\text{Det Size x } 1000\ \frac{\text{mrad}}{\text{rad}}}{f^{\#} \text{ x Diam x Scan Vel}_{RUN\ 1}}\right) \text{x (Exact Noise BW)}_{RUN\ 1}$$

It can be seen from the above expression that the detector MRT is a function of the results of both runs 1 and 2. From run 1 the NEΔT, exact noise bandwidth, and the scan velocity are found on page 4 of the output. Once the results have been determined, the detector MRT can be calculated.

The above procedure can best be illustrated with an example. The sample data set (Figure (C-1) corresponds to a 350 x 350 array of 1 mil detectors. (The system performance, however, is independent of the number of detectors in the array.) In addition, the peak D star of 14.5×10^{10} cm$\sqrt{\text{Hz}}$/w corresponds to a temperature of 195°K with a detector R_oA = 40 ohm - cm^2. Furthermore, the CCD noise has been eliminated by setting the value of C_{rw} in the S(f) equation (MSI input only) to $1.0 \times 10^{+10}$ (i.e., extremely large). The S-factors were generated using the following parameters:

```
DONE    1
ENDS
NPSP      1.1  1.0  1.0  1.0  .98  .21  0.0  0.0  0.0  0.0
FOR2
ENDS
DETR    0.5       0.5       1.0       4000.     1.0       14.5      1.0
FOR1
ENDS    1
ENDS
DSTD    .8   .82   .85 .87  .9   .92  .95  1.0  .95  .90
DSTL    3.0  3.2  3.3  3.4  3.5  3.6  3.8  4.0  4.1  4.2
NPSP      2.0  1.0  1.0  1.0  1.0  1.0  0.0  0.0  0.0  0.0
NPSF    1.0  1.5  2.0  3.0  4.0  5.0  6.0  7.0
EMTF    1.0  1.0  1.0  1.0  1.0  1.0  1.0  1.0  1.0  1.0
FOR2
ENDS
TARG    5.25      2.7       5.25      12.
ENVI    15.       50.       23.       0.0
STAB    0.0       0.0
SYST    10.0      7.45      12.0      1.0       0.0
DISP    0.0       50.0      .019      .019
ELEC    1.0       0.0       0.0       0.0       0.0       0.0
SCAN    60.       1.0       1.0
DET2    27.       0.0       10000.
DSTR    0.5       0.5       350.      1.0       1.0       14.5      1.0
OPTI    1.0       2.0       0.6       0.0       3.6
BAND    3.0       4.2
FOR1
```

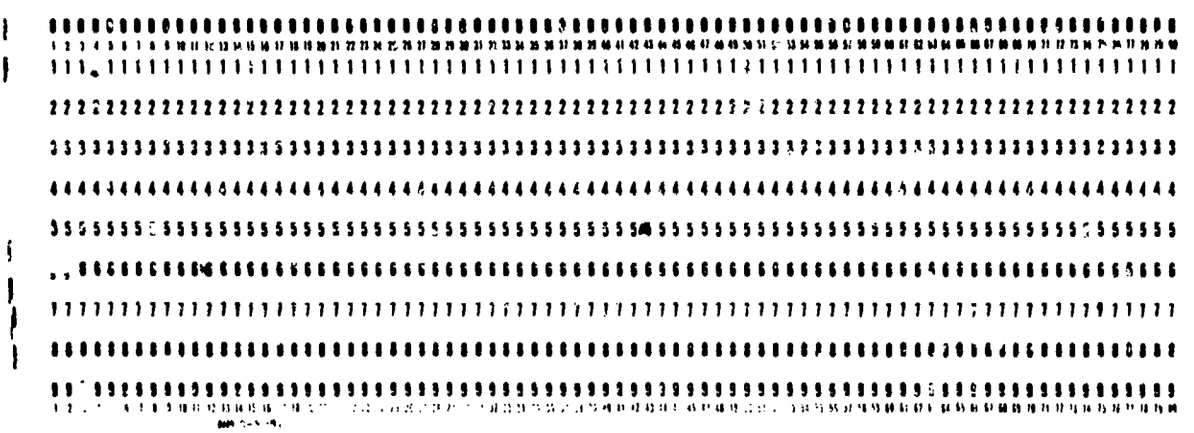

Figure C-1. Sample Data Deck

R_oA = 40Ω-cm^2

N = 4000

T = 195 K

I_B = 3.6×10^{-10} amps

C_{rw} = $1.0 \times 10^{+10}$ F

A = 6.25×10^{-6} cm^2

q = 1.6×10^{-19} Coul

k = 1.38×10^{-23}

C/A = 5×10^{-8} F/cm^2

$\dot{F}$ = 60.0 fps

fo = 1.0×10^{3} Hz

f_n = 50.0

The resulting values for S are found on the NPSP data card in deck 2. Notice the first value on the second NPSP card. The value is 1.1 but what was actually calculated was 1.0. The reason for the discrepancy is that the NVL program requires that the first value be greater than 1.0. This small change should not affect the results.

The results of the simulation are found in Figure C-2. Notice that, on the input sections of both runs, the key data cards for the staring focal plane are highlighted. The values for determining the MRT are also highlighted.

```
INPUT DATA

RUN NUMBER    1

YOUR SPECTRAL BAND IS     3.000     TO     4.200     MICRONS

OPTICS

     DIAMETER                          2.000     INCHES
     F-NUMBER                          1.000
     FOCAL LENGTH                      2.000     INCHES
     AVG. OPTICAL TRANSMISSION          .600
     WAVELENGTH FOR DIFFRACTION        3.600     MICRONS
     GEOMETRIC BLUR SPOT SIZE          0.000     MRAD.

DETECTOR

     HORIZONTAL IFOV                    .500     MRAD.
     VERTICAL IFOV                      .500     MRAD.
     DETECTORS IN PARALLEL              350.
     DETECTORS IN SERIES                 1.      STARING INPUT, RUN 1
     DETECTOR SIZE                    .00100     INCHES
     PEAK D*                           14.50     (1E10)CM-SQRT(HZ)/WATT
     MEASURING FREQUENCY OF D*         1000.     HERTZ
     COLD SHIELD ANGLE                27.000     DEGREES
     LIMITING NOISE                    DETECTOR
     DETECTOR RESPONSE,3-DB POINT    .100E+08     HERTZ

SCANNER

     FRAME RATE                       60.000     FRAMES/SECOND
     SCAN EFFICIENCY                   1.000
     OVERSCAN RATIO                    1.000

ELECTRONICS

     PREAMP,LOW FREQ 3-DB CUT-ON       1.000     HERTZ
     AMPLIFIER,3-DB POINT              0.000     HERTZ
     E/O LED WIDTH                  0.00000      MRAD.
     E/O LED LENGTH                 0.00000      MRAD.
     APERTURE CORRECTION AMPLITUDE     0.000
     APERTURE CORRECTION FREQUENCY        0.     HERTZ
```

Figure C-2. Typical Computer Program Output

INPUT DATA

DISPLAY

TYPE	CRT DISPLAY	
X SPOT SIZE	.019	MRAD.
Y SPOT SIZE	.019	MRAD.
AVERAGE BRIGHTNESS	50.000	FT. LAMBERTS

SYSTEM

HORIZONTAL FOV	10.000	DEGREES
VERTICAL FOV	7.450	DEGREES
MAGNIFICATION	12.000	
WFOV/NFOV	1.000	
NOISE EQUIV. DELTA T	0.000	DEGREES C

STABILIZATION

SYSTEM STATE	STABILIZED	
X VIBRATION CONSTANT	0.00	
Y VIBRATION CONSTANT	0.00	

STANDARD INPUTS

EYE INTEGRATION TIME	.200	SECONDS
THRESHOLD SIGNAL/NOISE	2.250	

INPUT DATA

ATMOSPHERIC PARAMETERS

CONDITION	CLEAR	
VISIBILITY RANGE	23.000	KILOMETERS
RELATIVE HUMIDITY	50.000	PERCENT
AIR TEMPERATURE	15.000	DEGREES C

TARGET + BACKGROUND

TARGET LENGTH	5.250	METERS
TARGET WIDTH	2.700	METERS
TARGET DELTA T	5.250	DEGREES C
BACKGROUND TEMPERATURE	12.000	DEGREES C

RANGE REQUIREMENTS

MIN. REQUIRED RANGE FOR RECOG.	500	METERS
MAX. REQUIRED RANGE FOR RECOG.	5000	METERS
RANGE INCREMENTS FOR RECOG.	500	METERS
MIN. REQUIRED RANGE FOR DETEC.	1000	METERS
MAX. REQUIRED RANGE FOR DETEC.	10000	METERS
RANGE INCREMENTS FOR DETEC.	1000	METERS

Figure C-2. Typical Computer Program Output (continued)

INPUT DATA

TEMPORAL MTF*S

FREQ. (LOG HERTZ)	0.00	.01	.10	.20	.30	.50	.60	.70	1.00	10.00
DETECT. ROLLOFF MTF(X)	1.00	1.00	1.00	1.00	1.00	1.00	1.00	1.00	1.00	1.00
DETECT. ROLLOFF MTF(Y)	1.00	1.00	1.00	1.00	1.00	1.00	1.00	1.00	1.00	1.00
ELECTRONIC MTF	1.00	1.00	1.00	1.00	1.00	1.00	1.00	1.00	1.00	1.00
BOOST MTF	1.00	1.00	1.00	1.00	1.00	1.00	1.00	1.00	1.00	1.00

SPATIAL COMPONENTS MTF*S

FREQ. (CYC./MRAD.)	0.00	1.00	2.00	3.00	3.50	4.00	4.50	5.00	6.00	7.00
OPTICS MTF (X)	1.00	1.00	1.00	1.00	1.00	1.00	1.00	1.00	1.00	1.00
OPTICS MTF (Y)	1.00	1.00	1.00	1.00	1.00	1.00	1.00	1.00	1.00	1.00
VIDICON MTF (X)	1.00	1.00	1.00	1.00	1.00	1.00	1.00	1.00	1.00	1.00
VIDICON MTF (Y)	1.00	1.00	1.00	1.00	1.00	1.00	1.00	1.00	1.00	1.00
STABILIZATION MTF (X)	1.00	1.00	1.00	1.00	1.00	1.00	1.00	1.00	1.00	1.00
STABILIZATION MTF (Y)	1.00	1.00	1.00	1.00	1.00	1.00	1.00	1.00	1.00	1.00

NOISE POWER SPECTRUM (VOLTS/SQRT(HZ))

FREQ.(LOG HERTZ)	1.00	1.50	2.00	3.00	4.00	5.00	6.00	7.00	0.00	0.00
POWER(TIMES 1E-9)	2.00	1.00	1.00	1.00	1.00	1.00	0.00	0.00	0.00	0.00

STARING INPUT

D* OF DETECTOR (CM.*SQRT(HZ.) /WATT)

WAVELENGTH (MICRONS)	3.00	3.20	3.30	3.40	3.50	3.60	3.80	4.00	4.10	4.20
D* (TIMES 1E10)	.80	.82	.85	.87	.90	.92	.95	1.00	.95	.90

INPUT DATA

DETECTION + RECOGNITION PROBABILITY DENSITY

DETECTION FREQ.	12.50	5.00	3.00	2.00	1.50	1.00	.75	.50	.25	0.00
BEST RECOG. FREQ.	37.50	15.00	9.00	6.00	4.50	3.00	2.25	1.50	.75	0.00
WORST RECOG. FREQ.	50.00	20.00	12.00	8.00	5.00	4.00	3.00	2.00	1.00	0.00
PROBABILITY	1.00	1.00	1.00	.95	.80	.50	.30	.10	.02	0.00

Figure C-2. Typical Computer Program Output (continued)

PREDICTED SYSTEM MTF			PREDICTED NOISE FILTERING MTF		
FREQ	X MTF	Y MTF	FREQ	X MTF	Y MTF
0.00	1.00	1.00	0.00	1.00	1.00
.10	1.00	1.00	1.52	.96	.96
.20	.98	.98	3.04	.84	.84
.30	.96	.96	4.56	.67	.67
.40	.93	.93	6.08	.50	.50
.50	.90	.90	7.60	.33	.33
.60	.85	.85	9.12	.21	.21
.70	.80	.80	10.64	.12	.12
.80	.75	.75	12.16	.06	.06
.90	.69	.69	13.68	.03	.03
1.00	.62	.62	15.20	.01	.01
1.10	.56	.56	16.72	.00	.00
1.20	.49	.49	18.24	.00	.00
1.30	.42	.42	19.76	.00	.00
1.40	.35	.35	21.28	.00	.00
1.50	.29	.29	22.80	.00	.00
1.60	.22	.22	24.32	.00	.00
1.70	.16	.16	25.84	.00	.00
1.80	.10	.10	27.36	.00	.00
1.90	.05	.05	28.88	.00	.00

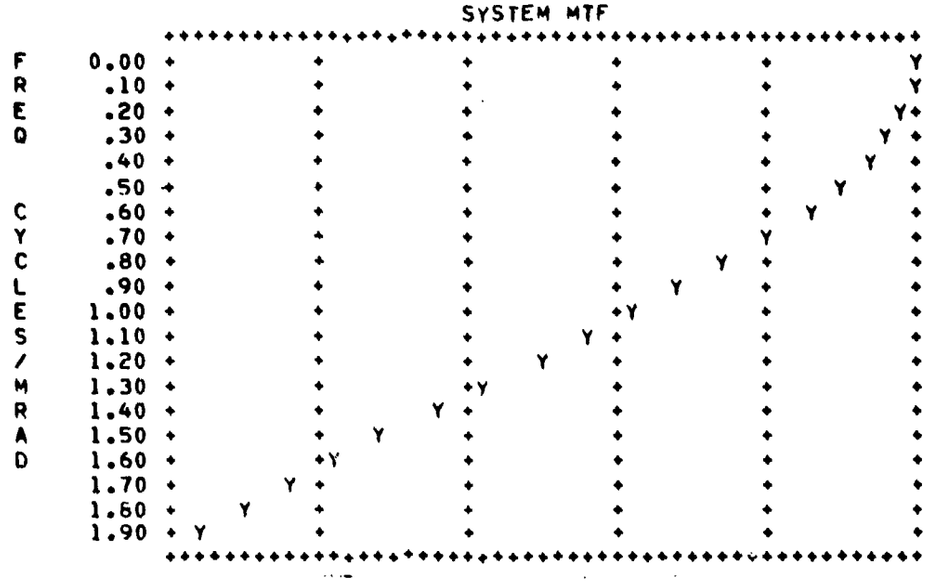

INTEGRAL OF D-STAR*W-PRIME= .216E+06
EXACT NOISE BANDWIDTH= .121E+05
WHITE NOISE BANDWIDTH= .123E+05

SCAN VELOCITY IN MR/SEC= .782E+04
DET NOISE LIMITED NET= .447E+00

EXACT NOISE BANDWIDTH RUN 1

SCAN VELOCITY RUN 1

NE ΔT RUN 1

Figure C-2. Typical Computer Program Output (continued)

FILTERED NOISE

FREQ	Q	QQ
.100E+00	.962F-01	.110F+00
.200E+00	.184F+00	.198E+00
.300E+00	.268F+00	.283F+00
.400E+00	.349E+00	.364E+00
.500E+00	.427F+00	.441E+00
.600E+00	.502F+00	.514E+00
.700E+00	.574F+00	.584E+00
.800E+00	.645F+00	.652E+00
.900E+00	.714F+00	.717E+00
.100E+01	.779F+00	.779E+00
.110E+01	.844F+00	.839E+00
.120E+01	.907F+00	.897E+00
.130E+01	.967F+00	.952E+00
.140E+01	.103F+01	.101E+01
.150E+01	.109F+01	.106E+01
.160E+01	.115E+01	.111E+01
.170E+01	.121F+01	.115E+01
.180E+01	.126F+01	.120E+01
.190E+01	.131F+01	.124E+01
.200E+01	.137F+01	.128E+01

PREDICTED MINIMUM RESOLVABLE TEMPERATURE

FREQ	X MRT	Y MRT	XLMRT	YLMRT	SMRT
.100E+00	.108E-01	.116E-01	.343E-01	.366E-01	.501E-01
.200E+00	.217E-01	.225E-01	.485E-01	.503E-01	.698E-01
.300E+00	.330E-01	.339E-01	.603E-01	.619E-01	.864E-01
.400E+00	.452E-01	.462E-01	.715E-01	.730E-01	.102E+00
.500E+00	.587E-01	.596E-01	.830E-01	.843E-01	.118E+00
.600E+00	.739E-01	.748E-01	.954E-01	.965E-01	.136E+00
.700E+00	.914E-01	.922E-01	.109E+00	.110E+00	.155E+00
.800E+00	.112E+00	.113E+00	.125E+00	.126E+00	.178E+00
.900E+00	.137E+00	.137E+00	.144E+00	.145E+00	.204E+00
.100E+01	.168E+00	.168E+00	.168E+00	.168E+00	.237E+00
.110E+01	.206E+00	.206E+00	.197E+00	.196E+00	.278E+00
.120E+01	.256E+00	.255E+00	.234E+00	.233E+00	.330E+00
.130E+01	.323E+00	.320E+00	.283E+00	.281E+00	.398E+00
.140E+01	.415E+00	.410E+00	.351E+00	.347E+00	.493E+00
.150E+01	.549E+00	.541E+00	.448E+00	.441E+00	.629E+00
.160E+01	.758E+00	.743E+00	.599E+00	.587E+00	.839E+00
.170E+01	.112E+01	.109E+01	.856E+00	.836E+00	.120E+01
.180E+01	.185E+01	.180E+01	.138E+01	.134E+01	.193E+01
.190E+01	.409E+01	.397E+01	.297E+01	.288E+01	.414E+01
.200E+01	.200E+08	.200E+08	.141E+08	.141E+08	.200E+08

MRT RUN 1

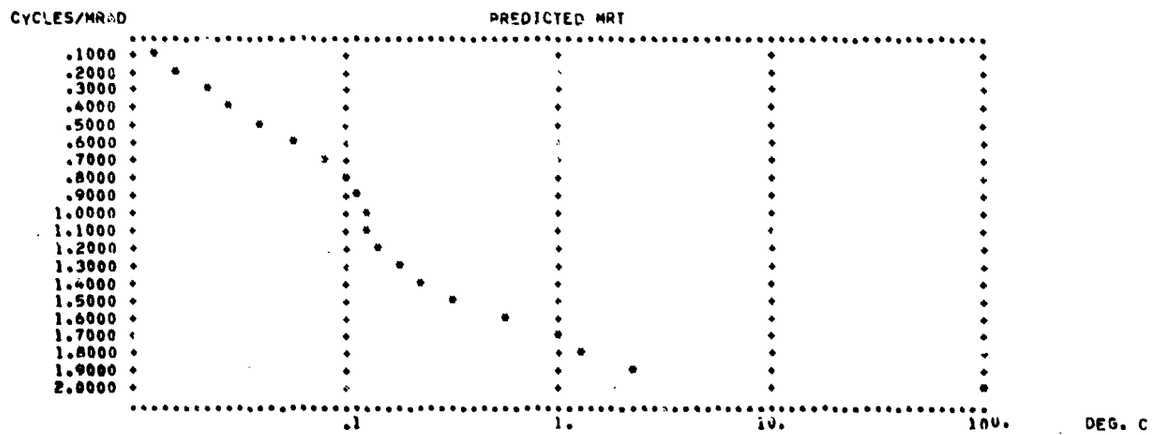

Figure C-2. Typical Computer Program Output (continued)

INPUT DATA

RUN NUMBER 2

YOUR SPECTRAL BAND IS 3.000 TO 4.200 MICRONS

OPTICS

DIAMETER	2.000	INCHES
F-NUMBER	1.000	
FOCAL LENGTH	2.000	INCHES
AVG. OPTICAL TRANSMISSION	.600	
WAVELENGTH FOR DIFFRACTION	3.600	MICRONS
GEOMETRIC BLUR SPOT SIZE	0.000	MRAD.

DETECTOR

HORIZONTAL IFOV	.500	MRAD.
VERTICAL IFOV	.500	MRAD.
DETECTORS IN PARALLEL	1.	
DETECTORS IN SERIES	4000.	
DETECTOR SIZE	.00100	INCHES
PEAK D*	14.50	(1E10)CM-SQRT(HZ)/WATT
MEASURING FREQUENCY OF D*	1000.	HERTZ
COLD SHIELD ANGLE	27.000	DEGREES
LIMITING NOISE	DETECTOR	
DETECTOR RESPONSE,3-DB POINT	.100E+08	HERTZ

STARING INPUT, RUN 2

SCANNER

FRAME RATE	60.000	FRAMES/SECOND
SCAN EFFICIENCY	1.000	
OVERSCAN RATIO	1.000	

ELECTRONICS

PREAMP,LOW FREQ 3-DB CUT-ON	1.000	HERTZ
AMPLIFIER,3-DB POINT	0.000	HERTZ
E/O LED WIDTH	0.00000	MRAD.
E/O LED LENGTH	0.00000	MRAD.
APERTURE CORRECTION AMPLITUDE	0.000	
APERTURE CORRECTION FREQUENCY	0.	HERTZ

INPUT DATA

DISPLAY

TYPE	CRT DISPLAY	
X SPOT SIZE	.019	MRAD.
Y SPOT SIZE	.019	MRAD.
AVERAGE BRIGHTNESS	50.000	FT. LAMBERTS

SYSTEM

HORIZONTAL FOV	10.000	DEGREES
VERTICAL FOV	7.450	DEGREES
MAGNIFICATION	12.000	
WFOV/NFOV	1.000	
NOISE EQUIV. DELTA T	0.000	DEGREES C

STABILIZATION

SYSTEM STATE	STABILIZED	
X VIBRATION CONSTANT	0.00	
Y VIBRATION CONSTANT	0.00	

STANDARD INPUTS

EYE INTEGRATION TIME	.200	SECONDS
THRESHOLD SIGNAL/NOISE	2.250	

Figure C-2. Typical Computer Program Output (continued)

INPUT DATA

ATMOSPHERIC PARAMETERS

CONDITION	CLEAR	
VISIBILITY RANGE	23.000	KILOMETERS
RELATIVE HUMIDITY	50.000	PERCENT
AIR TEMPERATURE	15.000	DEGREES C

TARGET + BACKGROUND

TARGET LENGTH	5.250	METERS
TARGET WIDTH	2.700	METERS
TARGET DELTA T	5.250	DEGREES C
BACKGROUND TEMPERATURE	12.000	DEGREES C

RANGE REQUIREMENTS

MIN. REQUIRED RANGE FOR RECOG.	500	METERS
MAX. REQUIRED RANGE FOR RECOG.	5000	METERS
RANGE INCREMENTS FOR RECOG.	500	METERS
MIN. REQUIRED RANGE FOR DETEC.	1000	METERS
MAX. REQUIRED RANGE FOR DETEC.	10000	METERS
RANGE INCREMENTS FOR DETEC.	1000	METERS

INPUT DATA

TEMPORAL MTF'S

FREQ. (LOG HERTZ)	0.00	.01	.10	.20	.30	.50	.60	.70	1.00	10.00
DETECT. ROLLOFF MTF(X)	1.00	1.00	1.00	1.00	1.00	1.00	1.00	1.00	1.00	1.00
DETECT. ROLLOFF MTF(Y)	1.00	1.00	1.00	1.00	1.00	1.00	1.00	1.00	1.00	1.00
ELECTRONIC MTF	1.00	1.00	1.00	1.00	1.00	1.00	1.00	1.00	1.00	1.00
BOOST MTF	1.00	1.00	1.00	1.00	1.00	1.00	1.00	1.00	1.00	1.00

SPATIAL COMPONENTS MTF'S

FREQ. (CYC./MRAD.)	0.00	1.00	2.00	3.00	3.50	4.00	4.50	5.00	6.00	7.00
OPTICS MTF (X)	1.00	1.00	1.00	1.00	1.00	1.00	1.00	1.00	1.00	1.00
OPTICS MTF (Y)	1.00	1.00	1.00	1.00	1.00	1.00	1.00	1.00	1.00	1.00
VIDICON MTF (X)	1.00	1.00	1.00	1.00	1.00	1.00	1.00	1.00	1.00	1.00
VIDICON MTF (Y)	1.00	1.00	1.00	1.00	1.00	1.00	1.00	1.00	1.00	1.00
STABILIZATION MTF (X)	1.00	1.00	1.00	1.00	1.00	1.00	1.00	1.00	1.00	1.00
STABILIZATION MTF (Y)	1.00	1.00	1.00	1.00	1.00	1.00	1.00	1.00	1.00	1.00

NOISE POWER SPECTRUM (VOLTS/SQRT(HZ))

S(F) CALCULATED FACTORS
STARING INPUT

FREQ.(LOG HERTZ)	1.00	1.50	2.00	3.00	4.00	5.00	6.00	7.00	8.00	9.00
POWER(TIMES 1E-9)	1.10	1.00	1.00	1.00	.98	.21	0.00	0.00	0.00	0.00

D* OF DETECTOR (CM.*SQRT(HZ.) /WATT)

WAVELENGTH (MICRONS)	3.00	3.20	3.30	3.40	3.50	3.60	3.80	4.00	4.10	4.20
D* (TIMES 1E10)	.80	.82	.85	.87	.90	.92	.95	1.00	.95	.90

Figure C-2. Typical Computer Program Output (continued)

Y MODULATION TRANSFER FUNCTIONS

FREQ	OPTIC	GOHLUR	OPTEC	VIDCN	LED	DSPLY	LOS	EYE
0.00	1.00	1.00	1.00	1.00	1.00	1.00	1.00	1.00
.10	1.00	1.00	1.00	1.00	1.00	1.00	1.00	.99
.20	1.00	1.00	.98	1.00	1.00	1.00	1.00	.98
.30	1.00	1.00	.96	1.00	1.00	1.00	1.00	.98
.40	1.00	1.00	.94	1.00	1.00	1.00	1.00	.97
.50	1.00	1.00	.90	1.00	1.00	1.00	1.00	.96
.60	1.00	1.00	.86	1.00	1.00	.99	1.00	.95
.70	1.00	1.00	.81	1.00	1.00	.99	1.00	.94
.80	1.00	1.00	.76	1.00	1.00	.99	1.00	.94
.90	1.00	1.00	.70	1.00	1.00	.98	1.00	.93
1.00	1.00	1.00	.64	1.00	1.00	.98	1.00	.92
1.10	1.00	1.00	.57	1.00	1.00	.98	1.00	.91
1.20	1.00	1.00	.50	1.00	1.00	.97	1.00	.90
1.30	1.00	1.00	.44	1.00	1.00	.97	1.00	.90
1.40	1.00	1.00	.37	1.00	1.00	.96	1.00	.89
1.50	1.00	1.00	.30	1.00	1.00	.96	1.00	.88
1.60	1.00	1.00	.23	1.00	1.00	.95	1.00	.85
1.70	1.00	1.00	.17	1.00	1.00	.95	1.00	.87
1.80	1.00	1.00	.11	1.00	1.00	.94	1.00	.86
1.90	1.00	1.00	.05	1.00	1.00	.93	1.00	.85

PREDICTED SYSTEM MTF			PREDICTED NOISE FILTERING MTF		
FREQ	X MTF	Y MTF	FREQ	X MTF	Y MTF
0.00	1.00	1.00	0.00	1.00	1.00
.10	1.00	1.00	1.52	.96	.96
.20	.98	.98	3.04	.84	.84
.30	.96	.96	4.56	.67	.67
.40	.93	.93	6.08	.50	.50
.50	.90	.90	7.60	.33	.33
.60	.85	.85	9.12	.21	.21
.70	.80	.80	10.64	.12	.12
.80	.75	.75	12.16	.06	.06
.90	.69	.69	13.68	.03	.03
1.00	.62	.62	15.20	.01	.01
1.10	.56	.56	16.72	.00	.00
1.20	.49	.49	18.24	.00	.00
1.30	.42	.42	19.76	.00	.00
1.40	.35	.35	21.28	.00	.00
1.50	.29	.29	22.80	.00	.00
1.60	.22	.22	24.32	.00	.00
1.70	.16	.16	25.84	.00	.00
1.80	.10	.10	27.36	.00	.00
1.90	.05	.05	28.88	.00	.00

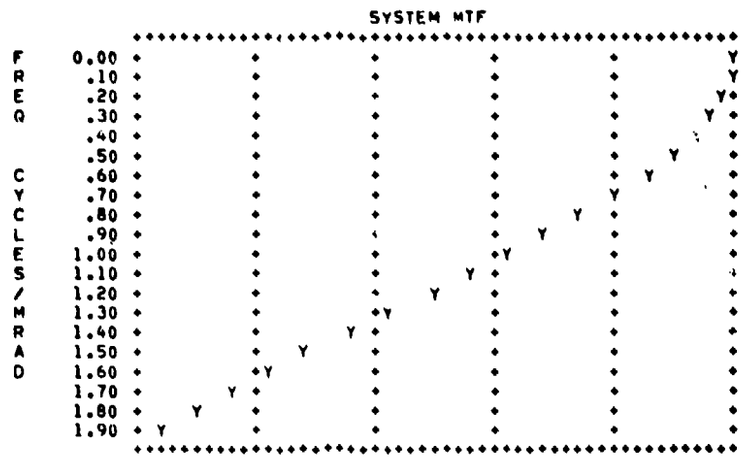

Figure C-2. Typical Computer Program Output (continued)

```
INTEGRAL OF D-STAR*w-PRIME=  .216E+06
EXACT NOISE BANDWIDTH=  .100E+06
WHITE NOISE BANDWIDTH=  .430E+07

SCAN VELOCITY IN MR/SEC=  .274E+07
DET NOISE LIMITED NET=  .204E-01
```

NE ΔT RUN 2

FILTERED NOISE

FREQ	Q	QQ
.100E+00	.310E-01	.730E-01
.200E+00	.423E-01	.114E+00
.300E+00	.479E-01	.137E+00
.400E+00	.506E-01	.154E+00
.500E+00	.520E-01	.167E+00
.600E+00	.528E-01	.179E+00
.700E+00	.533E-01	.189E+00
.800E+00	.536E-01	.197E+00
.900E+00	.539E-01	.205E+00
.100E+01	.540E-01	.212E+00
.110E+01	.542E-01	.218E+00
.120E+01	.543E-01	.223E+00
.130E+01	.544E-01	.227E+00
.140E+01	.544E-01	.231E+00
.150E+01	.545E-01	.233E+00
.160E+01	.545E-01	.235E+00
.170E+01	.545E-01	.236E+00
.180E+01	.546E-01	.237E+00
.190E+01	.546E-01	.237E+00
.200E+01	.546E-01	.237E+00

Figure C-2. Typical Computer Program Output (continued)

PREDICTED MINIMUM RESOLVABLE TEMPERATURE

FREQ	X MRT	Y MRT	XLMRT	YLMRT	45MRT
.100E+00	.182E-02	.279E-02	.576E-02	.393E-02	.105E-01
.200E+00	.307E-02	.505E-02	.687E-02	.113E-01	.132E-01
.300E+00	.413E-02	.698E-02	.754E-02	.128E-01	.148E-01
.400E+00	.509E-02	.848E-02	.805E-02	.140E-01	.162E-01
.500E+00	.606E-02	.104E-01	.856E-02	.154E-01	.176E-01
.600E+00	.709E-02	.130E-01	.915E-02	.168E-01	.192E-01
.700E+00	.824E-02	.155E-01	.985E-02	.185E-01	.210E-01
.800E+00	.956E-02	.183E-01	.107E-01	.205E-01	.231E-01
.900E+00	.111E-01	.217E-01	.117E-01	.229E-01	.257E-01
.100E+01	.131E-01	.259E-01	.131E-01	.259E-01	.290E-01
.110E+01	.155E-01	.310E-01	.147E-01	.296E-01	.330E-01
.120E+01	.185E-01	.376E-01	.169E-01	.343E-01	.382E-01
.130E+01	.226E-01	.462E-01	.198E-01	.405E-01	.451E-01
.140E+01	.282E-01	.581E-01	.239E-01	.491E-01	.546E-01
.150E+01	.363E-01	.752E-01	.296E-01	.614E-01	.681E-01
.160E+01	.486E-01	.101E+00	.386E-01	.801E-01	.889E-01
.170E+01	.702E-01	.146E+00	.536E-01	.112E+00	.124E+00
.180E+01	.114E+00	.237E+00	.849E-01	.177E+00	.196E+00
.190E+01	.246E+00	.514E+00	.179E+00	.373E+00	.413E+00
.200E+01	.200E+08	.200E+08	.141E+08	.141E+08	.200E+08

MRT, RUN 2

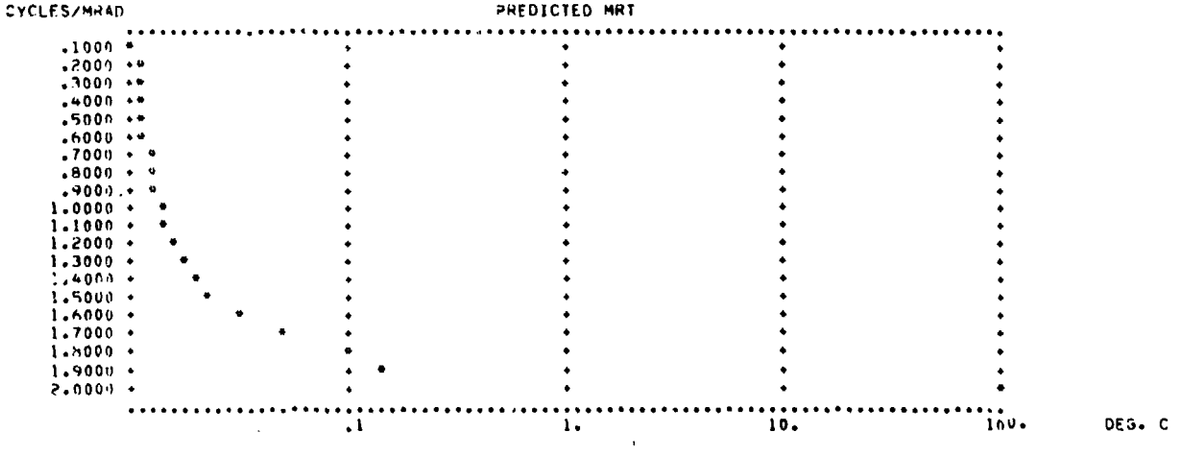

Figure C-2. Typical Computer Program Output (concluded)

APPENDIX D

MSI INPUT SPECTRAL NOISE DENSITY

APPENDIX D

MSI INPUT SPECTRAL NOISE DENSITY

To model the detector/CCD focal plane performance when using the MSI input circuit, the expression for the S(f) factor in Section 6 is

$$S(f) = \frac{4R^2q\left(I_B+\frac{KTA}{qR_oA}\right)\left|\frac{\sin(\pi f/NF)}{\pi f/NF}\right|^2\left|\frac{1}{1+(2\pi fR_oA(C/A))^2}\right| + \frac{KT\exp(-f/f_N)}{f_N C_{RW}}}{4R^2q\left(I_B+\frac{KTA}{qR_oA}\right)} \qquad (D\text{-}1)$$

In this expression the KT/CRW term is due to the input KT/C sampling noise in the MSI input circuit.

APPENDIX E

CCD INPUT MODELING FOR THE MSI INPUT FOCAL PLANE

APPENDIX E

CCD INPUT MODELING FOR THE MSI INPUT FOCAL PLANE

In this appendix the overall CCD input transfer functions are derived for the MSI input circuit. It is shown that with the optimum number of samples the detector-only signal-to-noise reduces to that which would be obtained by integrating the signal and noise for the entire frame rate. The optimum sample rate is related to the roll-off of the detector noise and the frame rate by $N = (2\dot{F}RC)^{-1}$. By increasing the one-sample noise bandwidth of the detector, the relative contribution of the CCD reset noise to the overall noise is reduced, and a noise figure approaching 1.0 may be obtained.

CCD INPUT

The input transfer functions are based on the circuit configuration shown in Figure E-1.

The detector response function is simply on RC roll-off due to the detector (open circuit) resistance and the detector plus input gate capacitance. Thus,

$$|H_1(\omega)| = \left(\frac{R^2}{(1 + \omega/\omega_i)^2} \right)^{1/2} \qquad \omega_i = (RC)^{-1} \qquad \text{(E-1)}$$

The factor R changes input currents to voltages.

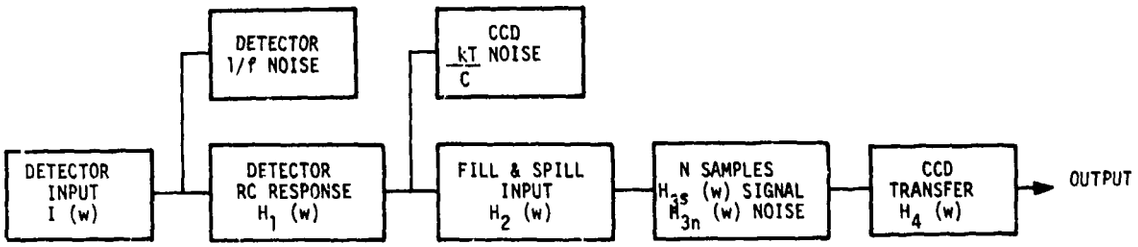

Figure E-1. Detector/CCD Transfer Function Modeling

The fill and spill takes place over a time τ_o. For small signals, the fill and spill input response is identical to an integrator.[2] Then

$$H_2(\omega) = \frac{\sin \omega\tau_o/2}{\omega\tau_o/2} \qquad \text{(E-2)}$$

---

[2]S. Emmons, 1975 CCD Conference Proceedings, p. 361.

SIGNAL TRANSFER FUNCTION

The effect of the N-sample summer is based on the assumption that the samples are taken at τ_s intervals. Then the output, at a given frequency ω, is given by the following sum:

$$V_o e^{j\omega t} = V_i(e^{j\omega t} + e^{j\omega t} e^{j\omega\tau_s} + e^{j\omega t} e^{j2\omega\tau_s} + \ldots + e^{j\omega t} e^{j(N+)\omega\tau_s}) \tag{E-3}$$

Summing

$$V_o e^{j\omega t} = V_i e^{j\omega t} \left[\frac{1 - e^{j\omega N\tau_s}}{1 - e^{j\omega\tau_s}} \right] \tag{E-4}$$

Then

$$H_{3s}(\omega) = \left[\frac{1 - e^{-j\omega N\tau_s}}{1 - e^{j\omega\tau_s}} \right] = \frac{\sin(N\omega\tau_s/2)}{\sin(\omega\tau_s/2)} \tag{E-5}$$

The CCD multiplexer is operating at a high frequency compared to $1/NT_s$ so its pass band will be much wider than that of the input circuit. If the CCD transfer efficiency may be set equal to 1.0, then $H_4(\omega) = 1$.

The overall input frequency response for signal is then

$$H_s(\omega) = H_1(\omega)\, H_2(\omega)\, H_{3s}(\omega)\, H_4(\omega)$$

or

$$H_s(\omega) = N\left(\frac{1}{1 + (\omega/\omega_i)^2}\right)^{1/2}\left(\frac{\sin \omega\tau/2}{\sin \omega\tau_s/2}\right)\left(\frac{\sin N\omega\tau_s/2}{N\omega\tau_s/2}\right) \qquad \text{(E-6)}$$

For the optimum case of maximum integration time, $\tau_o = \tau_s \equiv \tau$, and $H_s(\omega)$ has the form of an integrator with cutoff frequency f_{eff} given by

$$f_{eff} = \frac{1}{N\tau}$$

If the sampling is carried on for the entire frame time, $1/N\tau = \dot{F}$; the input has a frequency pass band equal to the frame frequency; and the output is N times an individual input, as is expected.

APPENDIX F

DETECTOR/CCD MODELING RESULTS FOR MSI INPUT

APPENDIX F

DETECTOR/CCD MODELING RESULTS FOR MSI INPUT

By applying the S(f) equation in Appendix D to the Staring Focal Plane Modeling Program, the effects of the multiple sampling on the system MRT can be derived. Figure F-1 shows a plot of MRT vs. number of samples at the input for a 60 fps frame rate for three different R_oA products. The MRT levels off at a sampling count of 10^4 - 10^5 depending upon R_oA. For $R_oA = 80\Omega\text{-cm}^2$, the MRT is within a factor of $\sqrt{2}$ of the minimum MRT at a sampling count of 5000.

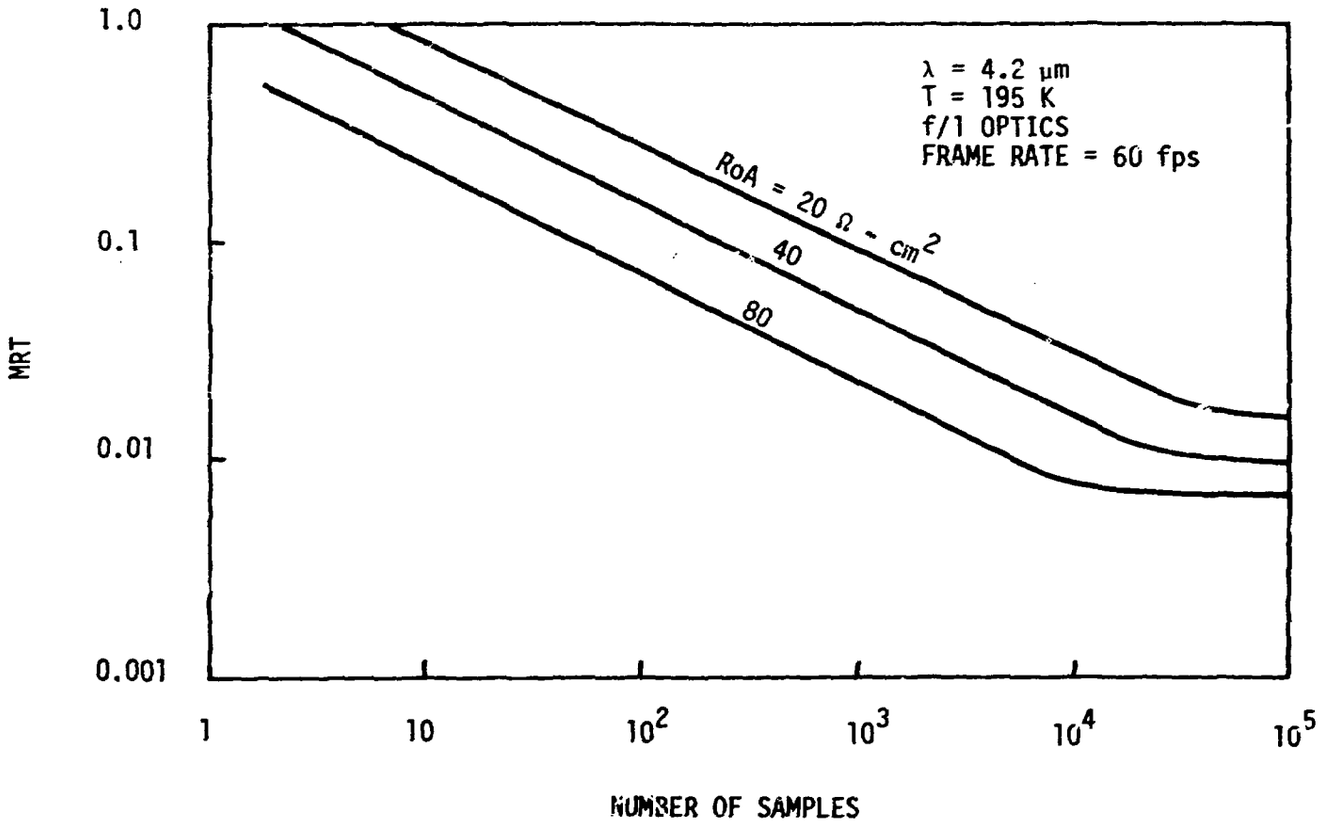

Figure F-1. MRT vs. Number of MSI Samples for Different Detector R_oA Products